National Library of Canada

Acquisitions and Bibliographic Services Branch

395 Wellington Street
Ottawa, Ontario
K1A 0N4

Bibliothèque nationale du Canada

Direction des acquisitions et des services bibliographiques

395, rue Wellington
Ottawa (Ontario)
K1A 0N4

Your file Votre référence

Our file Notre référence

NOTICE

The quality of this microform is heavily dependent upon the quality of the original thesis submitted for microfilming. Every effort has been made to ensure the highest quality of reproduction possible.

If pages are missing, contact the university which granted the degree.

Some pages may have indistinct print especially if the original pages were typed with a poor typewriter ribbon or if the university sent us an inferior photocopy.

AVIS

La qualité de cette microforme dépend grandement de la qualité de la thèse soumise au microfilmage. Nous avons tout fait pour assurer une qualité supérieure de reproduction.

S'il manque des pages, veuillez communiquer avec l'université qui a conféré le grade.

La qualité d'impression de certaines pages peut laisser à désirer, surtout si les pages originales ont été dactylographiées à l'aide d'un ruban usé ou si l'université nous a fait parvenir une photocopie de qualité inférieure.

Canada

Dislocations in Monolayers and Semiconductors

By

Qiang Ren

A thesis submitted to
the School of Graduate Studies and Research
in partial fulfilment of the requirements
for the degree of Doctor of Philosophy

Department of Physics

University of Ottawa
Ottawa, Ontario

April, 1995

National Library
of Canada

Acquisitions and
Bibliographic Services Branch

395 Wellington Street
Ottawa, Ontario
K1A 0N4

Bibliothèque nationale
du Canada

Direction des acquisitions et
des services bibliographiques

395, rue Wellington
Ottawa (Ontario)
K1A 0N4

Your file Votre référence

Our file Notre référence

ISBN 0-612-07859-0

Canada

UNIVERSITÉ D'OTTAWA
UNIVERSITY OF OTTAWA

Abstract

Four different aspects of the properties of dislocations in monolayer and semiconductors have been investigated:

i) Using atomic relaxation techniques, dislocation dipoles of various sizes and orientations have been studied for monolayers with the Lennard-Jones potential (LJP) and the nearest-neighbour piecewise linear force (PLF) interactions. In the LJP system the lower energy vacancy dipoles have over a wide range of angles an energy which is mainly a function of the vacancy content of the dipole. There is a competition between the elastic forces and the topological constraints which favour a five-fold coordinate vacancy (FCV) at the centre of each core. For the short range PLF system the lattice usually compresses upon the introduction of a dislocation, a consequence of the soft core of the interaction potential, and interstitial dipoles are lower in energy. For the long range LJP system the dislocations are mobile whereas for the PLF system they are pinned. The relevance of these results to existing theories of melting are discussed.

ii) Using generalized stacking-fault (GSF) energies obtained from first-principles density-functional calculations, a zero-temperature model for dislocations in silicon is constructed within the framework of a Peierls-Nabarro (PN) model. Core widths, core energies,PN pinning energies, and stresses are calculated for various possible perfect and imperfect dislocations. Both shuffle and glide sets are considered. 90° partials are shown to have a lower Peierls stress (PS) than 30° partials in accord with experiment.

iii) We have also studied by atomic relaxation techniques the properties of dislocations in silicon, modelled by the empirical potential of Stillinger and Weber. In order to compare with

the preceeding calculation no reconstruction is allowed. We find no evidence of dissociation in the shuffle dislocations. Within this model shuffle dislocations glide along their slipping planes. On the other hand, glide sets are shown to glide *only* in dissociated form. The dislocation displacement fields are essentially planar. The PS is found to be isotropic within the (111) plane. In other words the minimum stress at 0K required to move the dislocation in any direction with in that plane has the same projection unto the Burgers vector, the PS of the dislocation. Our PS are in good agreement with those from ii).

iv) Using a simple two dimensional LJP model, relaxation mechanisms of the epitaxial strain layers (ESL) have been simulated for various misfits and layer thickness. In this model, the relationship of two competing relaxation mechanisms is found. At small misfit, strain is released by nucleating misfit dislocations from the edges of system. This process is more favourable for the thicker layer. At large misfit, stress is relaxed through surface instability, allowing easy generation of misfit dislocations from the surface. Those results are qualitatively in agreement with experiments.

Acknowledgements

My deepest thanks go to my supervisor, Dr. Bela Joós for his helpful guidance, advice, support, understanding and encouragements, without which I cannot imagine how I could fulfil the requirements for the submission of the Ph.D thesis.

I would like to thank Dr. M.S. Duesbery for fruitful discussions and a lot of e-mails. I would also like to thank Dr. E. Kaxiras for providing us with his values for the generalized stacking-fault potential.

I would like to thank all my friends, Z. Zhou, Y.Cai, R. Parent, G. Nixon, C.Desruisseaux, ... for their help and encouragement.

This thesis could not have been written without a lot of family support. I want to thank my husband Deyang who gradually became an excellent cook and typist during this period. I owe him a great deal.

Finally, I owe a great debt of gratitude to the Ontario Ministry of College and Universities who has provided me with three years of Ontario Graduate Scholarship.

Contents

Chapter 1. Introduction

Dislocations are the basic topological defects in solids. It is natural then to expect them to play an important role in structural transformations. The processes of interest to us are: the melting in monolayers, plastic deformation in silicon and strain relaxation in the epitaxial strained layers. These are problems particularly suitable for dislocation driven kinetics for different reasons. In two dimensional (2D) systems, dislocations are point defects, singularities in the strain field which can be thermally excited in pairs called dislocation dipoles. Plastic deformation intrinsically relies on the sliding of atomic planes which can be represented by dislocation arrays. And finally strain relaxation in a strained layer is initiated as misfit dislocations. The actual role that dislocations play in such problems depends sensitively on their properties. These have been investigated in the following four closely related projects which are:

1). To study the behaviour of dislocations in 2D systems by using atomic relaxation techniques. Dislocation architectures of various sizes have been investigated including dislocation dipoles and dislocation lozenges. Two kinds of 2D systems with the Lennard-Jones potential and the nearest-neighbour piecewise linear force are used to study the impact of the range of potential on the energies and configurations of dislocations. The information obtained from this project will help to better define the source of the controversy existing on the nature of 2D melting.

2). With the knowledge of dislocations in 2D systems, the calculations are extended to three-dimensional (3D) systems. The second research goal is to construct a zero temperature model for dislocations in silicon within the framework of a Peierls-Nabarro (PN) model using

generalized stacking-fault energies obtained from first-principles density-functional approximations, and using this new model to study core width, core energies, PN pinning energies and stresses of various possible perfect and imperfect dislocations in silicon.

3). In order to verify the new model and the results obtained from 2), a different approach is taken. This part of the project is to investigate the properties of dislocations in silicon by atomic relaxation techniques, modelled by the empirical potential of Stillinger and Weber. The Peierls stresses of various dislocations and the characteristics of the dislocation displacement field are calculated. The motion and dissociation of glide and shuffle dislocations are also studied.

4). Our final project was to study relaxation mechanisms in epitaxial layers using relaxation techniques. Various layer thicknesses and strains are simulated in a simple two dimensional model. We try to determine the conditions and source of nucleating misfit dislocations through which the strain in epitaxial layers is released.

The outline of the thesis is as follows. In the next chapter, I briefly review the theory of dislocations. In chapter 3,4,5 and 6, the details of the model, procedure and results for each of the above four research projects are presented and discussed respectively. An overall conclusion ends the thesis.

Chapter 2. Theory of Dislocations

2.1 History of Dislocations

The history of dislocations has two starting points. The concept of the dislocation as an elastic singularity was first introduced by considering the deformation of a body occupying a multiply connected region of space, and a systematic theory was given by Volterra [1], as illustrated in Fig. 1, following earlier work by Michell [2], Weingarten [3] and Timpe [4]. Configurations (b) and (c) in Fig. 1 correspond to edge dislocations and (d) corresponds to a screw dislocation. Configuration (e) (f), which are twist disclinations, and (g) ,which is a wedge disclination, are not discussed further here, since they do not correspond to crystalline imperfections; the essential reason for this is that the displacements produced by these configurations are proportional to the outer cylinder radius and hence do not vanish as the radius tends to infinity. Volterra described the conditions under which the displacement function is continuous but multivalued (or single-valued but discontinuous), and Love [5] gave an account of this work in his famous treatise on elasticity. The word dislocation in English is due to Love, who referred to Volterra's "distorsioni" and remarked " I have ventured to call them dislocations".

Somigliana [6,7] developed further the elastic theory of dislocations, but the relation of this work to the structure of the real crystals was not perceived until much later. When x-ray diffraction techniques were used to examine crystals, it very soon became evident that most real

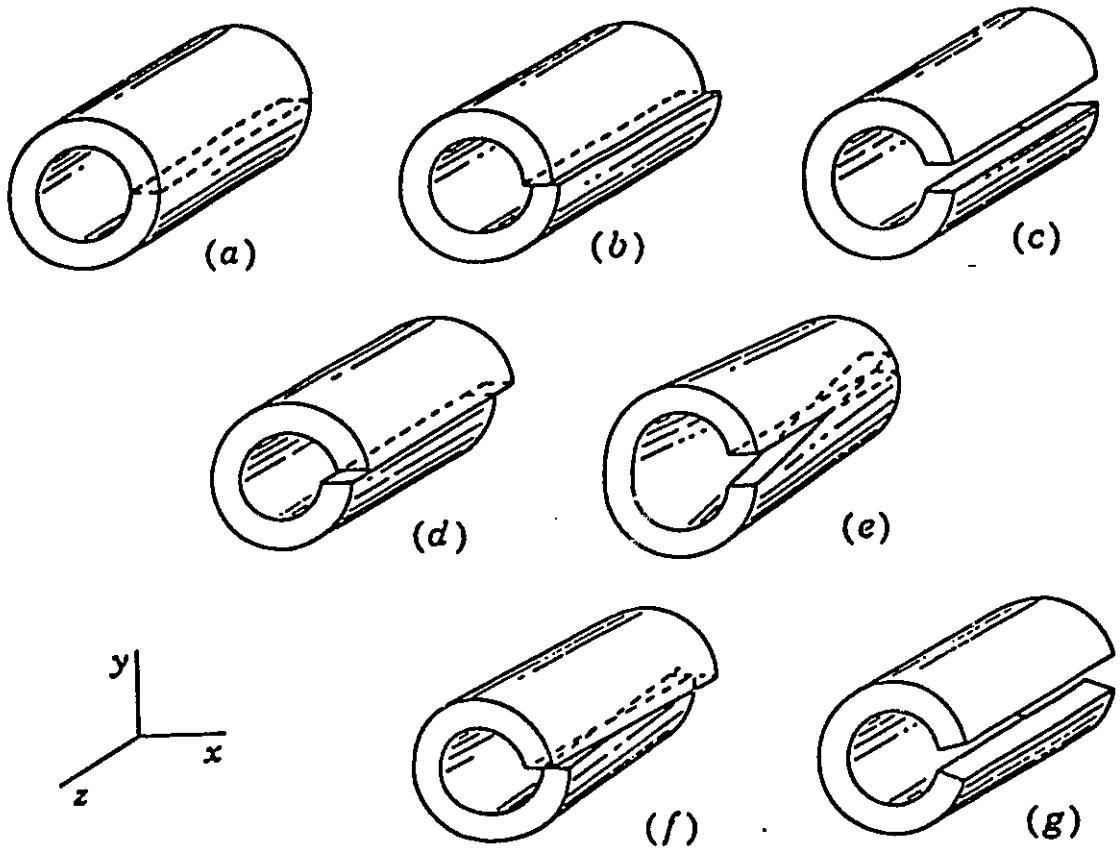

Fig. 1 A cylinder (a) as originally cut, and (b) to (g), as deformed to produce the six types of dislocations as proposed by Volterra.

crystals have imperfect structures (Darwin [8,9]). In principal, crystal dislocations might then have been postulated to explain the observed magnitudes of the diffracted intensities, but in fact the model of the mosaic structure, which evolved that real crystals consisted of small crystallites, 10^{-4} to 10^{-5} cm in diameter, slightly misoriented with respect to one another, used in Darwin's paper became the generally accepted crystallographic description, and the problem of the structure of the boundaries between misoriented regions was not pursued. The first suggestions that dislocations exist in real crystals thus arose not from direct observations on structure but in order to interpret experiments on the plastic behaviour of crystals [10,11], where plastic deformation of metals proceeded by formation of slip bands or slip packets.

Crystalline defects similar to dislocations were discussed by Prandtl [12] and Dehlinger [13] as a possible explanation for the large discrepancy between the theoretical and experimental strength of a crystal. The real introduction of the dislocation into physics came a few years later, when edge dislocations, shown in Fig. 2, were described by Taylor [14], Orowan [15] and Polanyi [16]; these papers form the second starting points for dislocation theory. Screw dislocations depicted in Fig. 3 and dislocations of general type were first considered by Burgers [17], and his classic papers mark the beginning of the systematic development of the theory. Other important publications at this time include the Peierls-Nabarro model of calculation of the stress needed to move a dislocation [18,19], and the first demonstration that low-angle grain boundaries may be regarded as planar arrays of dislocations [17,20].

The progress of dislocation theory since 1945 has been too rapid to permit any short historical summary, but for many years the existence of dislocations was disputed by some physicists and metallurgists. The discoveries of experimental techniques for the observation of

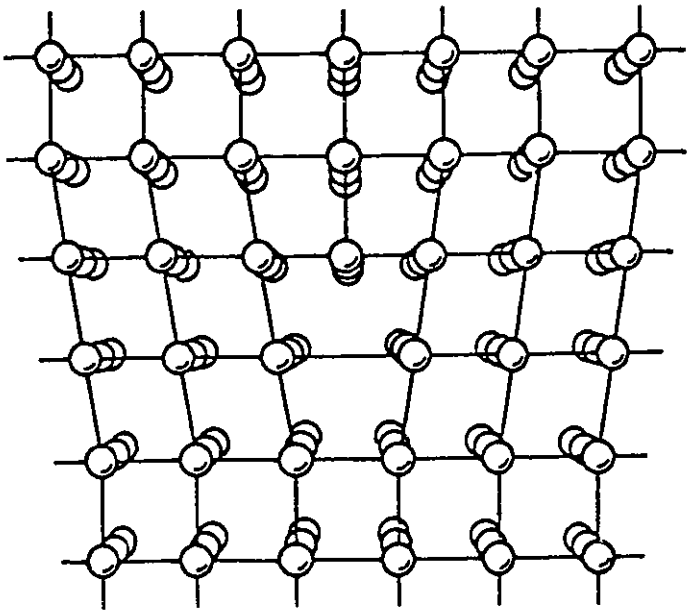

Fig. 2 An edge dislocation in a simple cubic crystal.

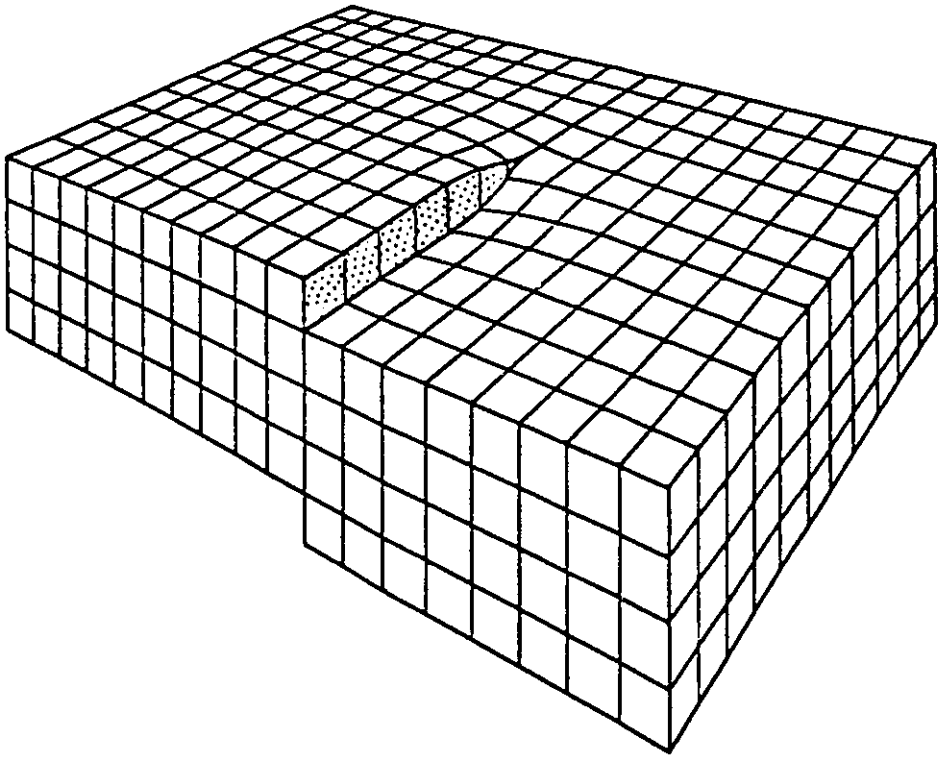

Fig. 3 A screw dislocation in a simple cubic crystal.

dislocations should thus be accorded particular significance in the development of the subject. Careful optical, electron, field ion and x-ray microscopy have provided such an abundance of evidence for dislocations that there can be no doubt that dislocations exist. The techniques can be divided into five main groups: (1) Surface methods, in which the point of emergence of a dislocation at the surface of a crystal is revealed, (2) Decoration methods for examining dislocations in bulk crystals transparent to light, (3) Transmission electron microscopy in which the dislocations are studied in specimens 1000-10,000 Å thick (0.1-1.0 μ where μ is a micron $= 10^{-4}$ cm $= 10^{4}$ Å), (4) X-ray diffraction which relies on local differences at dislocations in the scattering of x-rays, (5) Field microscopy which reveals the position of the individual atoms. Except for (5) and isolated examples in (3) these techniques do not reveal directly the structure of the dislocation, but rely on such features as the strain field of the dislocation. The techniques were reviewed in detail by Pashley [21].

2.2 Continuum Theory of Dislocation

2.2.1 Dislocation Line

The best description of a dislocation is obtained from a study of its formation in the crystalline lattice. Consider Fig. 4. In the centre is the starting material, a perfect , undeformed simple cubic lattice. (A simple cubic lattice is used for the sake of clarity. The only substance known to crystallize in this lattice structure is the metal polonium). Cut this lattice along any of the planes indicated in the auxiliary cubes. Let the atoms on one side of the cut shift in a

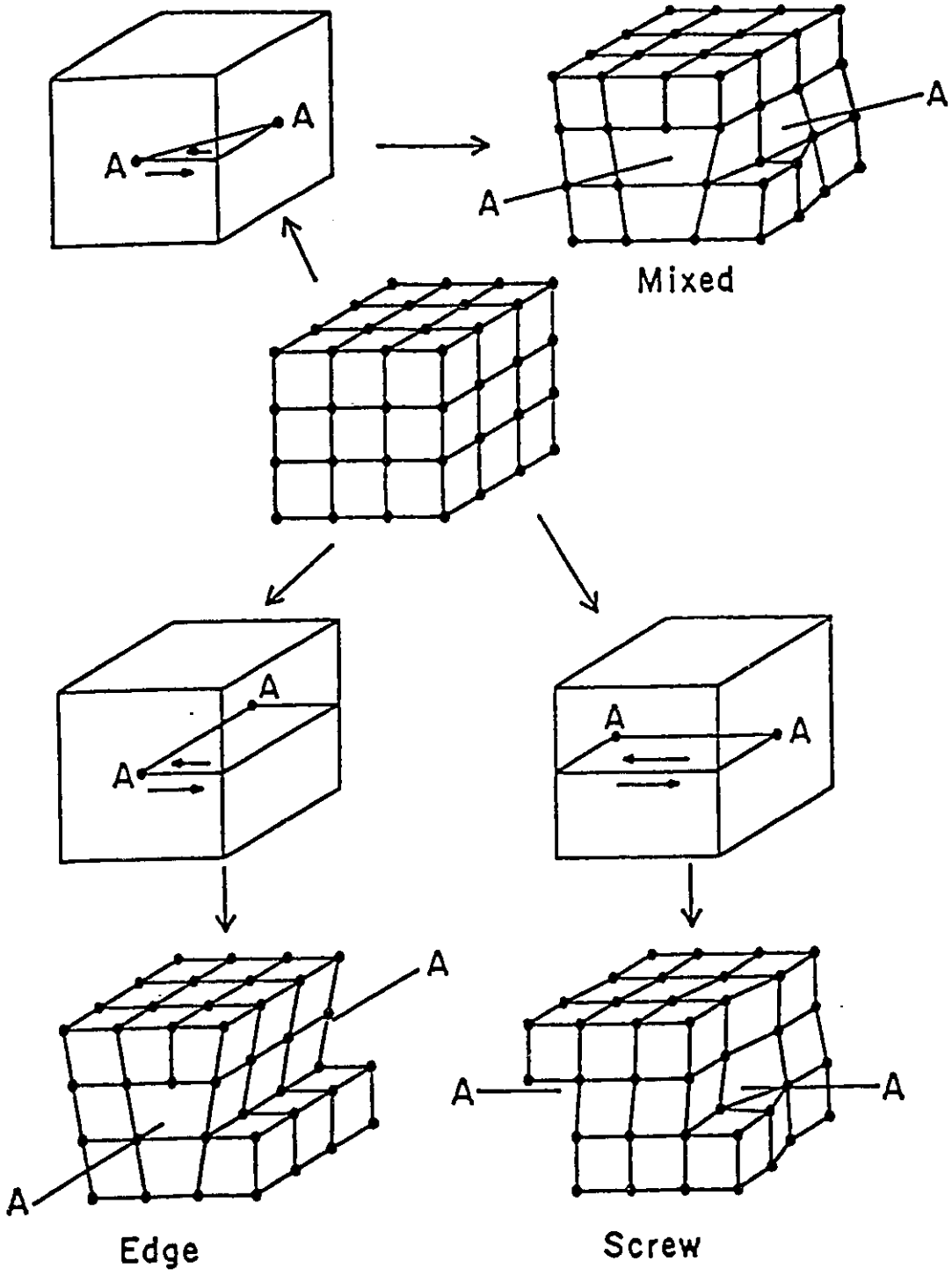

Fig. 4 The creation of an edge, a screw and a mixed dislocation.

direction parallel to the cut surface through a distance, relative to the corresponding atoms on the other side, equal to one atom spacing. Then rejoin the atoms on either side of the cut. The new, distorted lattice is shown in the outer figures. The lattice structure itself actually is almost perfect except near the lines AA of the various figures. The line imperfections AA in the lattice are dislocation lines.

The three types of dislocation lines are shown in Fig. 4. If the atoms over the cut surface are shifted in a direction perpendicular to the line AA, an edge dislocation is created in the lattice; if the shift is parallel to AA, a screw dislocation is produced; if the shift is neither parallel nor perpendicular to AA but rather at some arbitrary angle, a dislocation having the characteristics of both an edge and a screw dislocation is placed into the lattice. This third type is called mixed dislocation.

2.2.2 Burgers Vector and Burgers Circuit

Consider first the Burgers vector of the pure edge dislocation shown in Fig. 5(a). Two circuits have been drawn in this figure. The upper circuit is drawn clockwise [1] around the edge dislocation; the lower circuit avoids the dislocation. In each circuit the same number of jumps from atom to atom are made up as are made down, to the left as to the right. The starting point and the end point (the atoms shown solid) are one and the same atom in the case of the circuit that does not include the dislocation. However the starting and ending points are not the same atom for the circuit that does enclose the dislocation. Thus there is a closure failure in this circuit. The Burgers vector is defined to be this closure failure. The sense of the vector is from

---

[1] as that is the usual convention.

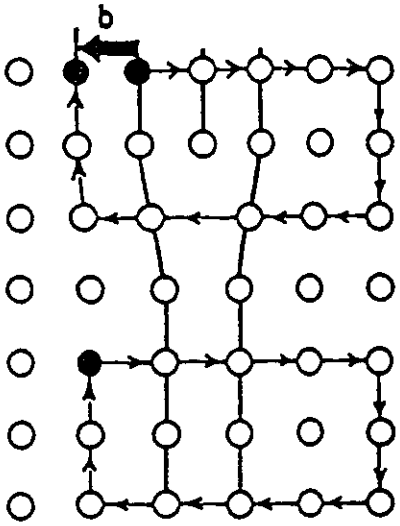

Fig. 5(a) Burgers circuit around edge dislocation. Positive direction of the dislocation line is taken to be out the plane of the figure.

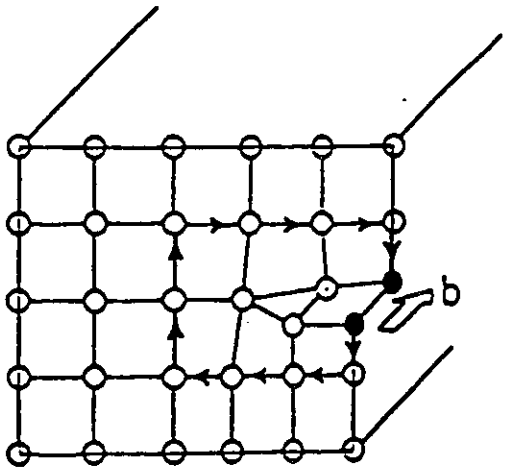

Fig. 5(b) Burgers circuit around screw dislocation.

the beginning point of the circuit to its end point. A circuit about a screw dislocation is shown in Fig. 5(b). In this case the closure failure leads to a vector *parallel* to the dislocation line. The Burgers vector of an edge dislocation is *perpendicular* to the dislocation line. In the case of a mixed dislocation the Burger vector makes some other angle with the dislocation line.

2.2.3 Stress Field of a Dislocation

Screw Dislocation

The elastic deformation around a dislocation can be represented in terms of the deformation of a cylindrical ring of isotropic material. The ring of isotropic material in Fig. 6(a) has been deformed to produce a screw dislocation. A radial slit LMNO was cut in the ring parallel to the z-axis and the free surfaces were displaced rigidly with respect to each other by a distance b, the magnitude of the Burgers vector of the screw dislocation, in the z-direction. For details, see ref. [22]. Here, I just summarize the main results for later use.

A uniform shear strain $u_{\theta z}$ ($= u_{z\theta}$) is produced throughout the ring which is equal to the step height b divided by the circumference $2\pi r$, of a cylindrical element of radius r,

$$u_{\theta z} = \frac{b}{2\pi r} \qquad \ldots(2.1)$$

The corresponding stress

$$\sigma_{\theta z} = \sigma_{z\theta} = \frac{\mu b}{2\pi r} \qquad \ldots(2.2)$$

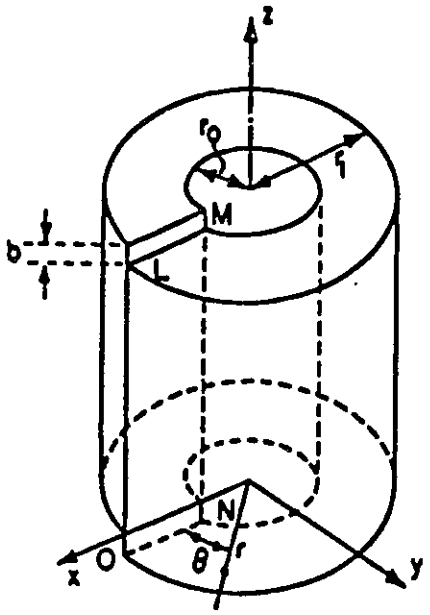

Fig. 6(a) Elastic distortion of a cylindrical ring simulating the distortion produced by the screw dislocation.

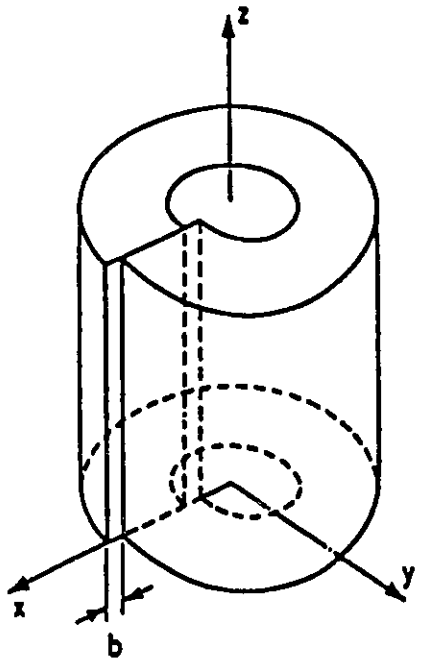

Fig. 6(b) Elastic distortion of a cylindrical ring simulating the distortion produced by the edge dislocation.

where μ is the shear modulus. Since the displacement of the ring is produced by a shear in the z-direction there will be no displacements in the x- and y-directions and the other stress components will be zero.

$$\sigma_{rr} = \sigma_{\theta\theta} = \sigma_{zz} = \sigma_{\theta r} = \sigma_{r\theta} = \sigma_{rz} = \sigma_{zr} = 0 \qquad \ldots(2.3)$$

Thus the stress field consists of two pure shears; $\sigma_{\theta z}$ in radial planes parallel to the z-direction and $\sigma_{z\theta}$ in planes normal to the z-axis perpendicular to the radius.

The stress fields has radial symmetry around the dislocation, ie. $\sigma_{\theta z} = \mu b/2\pi r$ and is independent of θ. This is closely related to the fact that a screw dislocation has no extra half plane and cannot be identified with a particular slip plane.

In rectangular coordinates the components of stress and displacement of a screw dislocation are

$$\sigma_{xz} = \sigma_{zx} = -\frac{\mu b}{2\pi}\frac{y}{x^2+y^2} ,$$

$$\sigma_{yz} = \sigma_{zy} = \frac{\mu b}{2\pi}\frac{x}{x^2+y^2} ,$$

$$\sigma_{xx} = \sigma_{yy} = \sigma_{zz} = \sigma_{xy} = \sigma_{yx} = 0 ,$$

$$u_z = \frac{b}{2\pi}\arctan\frac{y}{x} \qquad \ldots(2.4)$$

Edge Dislocation

The stress field is more complex than that of a screw dislocation but can be represented

in an isotropic ring in a similar way. Consider the edge dislocation in Fig. 2. The same elastic strain field can be produced in the ring by a rigid displacement of the faces of the slit by a distance b in the x-direction (Fig. 6(b)). The strain in the z-direction is zero and the deformation is basically planar. The stress and displacement components determined using isotropic theory are

$$\sigma_{xx} = -\frac{\mu b}{2\pi(1-\nu)} \frac{y(3x^2+y^2)}{(x^2+y^2)^2} ,$$

$$\sigma_{yy} = \frac{\mu b}{2\pi(1-\nu)} \frac{y(x^2-y^2)}{(x^2+y^2)^2} ,$$

$$\sigma_{xy} = \frac{\mu b}{2\pi(1-\nu)} \frac{x(x^2-y^2)}{(x^2+y^2)^2} ,$$

$$\sigma_{xz} = \sigma_{yz} = 0 ,$$

$$\sigma_{zz} = \nu(\sigma_{xx}+\sigma_{yy}) ,$$

$$u_x = \frac{b}{2\pi}\left[\tan^{-1}\frac{y}{x} + \frac{xy}{2(1-\nu)(x^2+y^2)}\right] ,$$

$$u_y = -\frac{b}{2\pi}\left[\frac{1-2\nu}{4(1-\nu)}\ln(x^2+y^2) + \frac{x^2-y^2}{4(1-\nu)(x^2+y^2)}\right] \qquad \ldots(2.5)$$

where ν is Poisson's ratio. The stress field has, therefore, both dilational and shear components. The largest normal stress is σ_{xx} which acts parallel to the slip vector. Since the slip plane can

be defined as y=0, the maximum compressive stress (σ_{xx} is negative) acts immediately below the slip plane. This observation is implied qualitatively by the type of distortion illustrated in Fig. 2.

The equations listed above have been used widely in studying dislocations problems. There are a number of limitations which must be realised. First, the elastic solutions apply to a *ring* of isotropic materials and not to a *solid* cylinder. Equations (2.4) and (2.5) show that stress varies inversely with distance from the centre of ring, ie. as 1/r, and therefore it will rise to infinity at r=0. Clearly infinite stresses cannot be supported at the centre of a dislocation and there is a limiting radius r_o below which the elastic solutions do not apply. Estimates of r_o suggest that it is of the order of 1nm. The central region of the dislocation of radius r_o is referred to as the *core of the dislocation*. Secondly, a real crystal is not an isotropic continuum and in the core of the dislocation continuum elastic theory is not applicable, it is necessary to consider the displacements of individual atoms and their interactions. These can be studied by computer simulations.

2.2.4 Strain Energy of a Dislocation

The existence of an elastically distorted region around a dislocation implies that a body containing a dislocation has an extra strain energy and the strain energy per unit length of the screw dislocations in the region from the core to the radius R is

$$E_s = \int_{r_o}^{R} \frac{\mu b^2}{4\pi r} dr = \frac{\mu b^2}{4\pi} \ln\left(\frac{R}{r_o}\right) \qquad \ldots(2.6)$$

If R is taken to be the external diameter of the crystal it follows that the elastic energy in a crystal containing a single dislocation will depend on the size of the crystal. The corresponding equation for the strain energy of an edge dislocation is

$$E_e = \frac{\mu b^2}{4\pi(1-\nu)} \ln\left(\frac{R}{r_o}\right) \qquad \ldots(2.7)$$

Thus the elastic energy of an edge dislocation is more than that of the screw dislocation by 1/(1-ν). For a mixed dislocation, where the Burgers vector makes an angle θ with the dislocation line, by superposition one finds

$$E_m = \frac{\mu b^2}{4\pi}\left[\frac{\sin^2\theta}{(1-\nu)} + \cos^2\theta\right] \ln\left(\frac{R}{r_o}\right) \qquad \ldots(2.8)$$

2.2.5 Interaction Energy Between Two Parallel Straight Dislocations

Consider two dislocations parallel to each other with Burgers vectors $\mathbf{b}_1$ and $\mathbf{b}_2$. ξ is a unit vector along the dislocation line. The energy of the interaction per unit length is

$$E_{12} = -\frac{\mu(\boldsymbol{b}_1\cdot\boldsymbol{\xi})(\boldsymbol{b}_2\cdot\boldsymbol{\xi})}{2\pi} \ln\frac{R_{12}}{r_o} - \frac{\mu}{2\pi(1-\nu)}\left[(\boldsymbol{b}_1\times\boldsymbol{\xi})\cdot(\boldsymbol{b}_2\times\boldsymbol{\xi})\right] \ln\frac{R_{12}}{r_o}$$

$$-\frac{\mu}{2\pi(1-\nu)R_{12}^2}\left[(\boldsymbol{b}_1\times\boldsymbol{\xi})\cdot\boldsymbol{R}_{12}\right]\left[(\boldsymbol{b}_2\times\boldsymbol{\xi})\cdot\boldsymbol{R}_{12}\right] \qquad \ldots(2.9)$$

This equation was first developped by Nabarro [23] and is very useful in the discussion of interactions between parallel dislocations. Note that $\mathbf{R}_{12}$ is the distance vector between two parallel dislocations.

2.3 Peierls-Nabarro (PN) Model

Begin with the edge dislocation in Fig. 2; above the slip plane the atoms are squeezed together (in the direction of slip), below the slip plane, the atoms are pulled apart. The shear stress acting across the slip plane hold the upper and lower halves of the crystal in equilibrium. Peierls [18] and Nabarro [19] treat the parts of the crystal above and below the slip plane as elastic continua; they take account of the periodic structure of the crystal by recognizing that the shear stress τ acting across the slip plane (x direction) is a periodic function of the relative displacement f of the adjoining atomic planes. For example, when f=b ,the atoms are again in register across the slip plane; hence the period is b.The condition of equilibrium leads to a relation between τ(f) and f(x) called the PN integro-differential equation

$$\frac{\mu}{2\pi(1-\nu)}\int_{-\infty}^{\infty}\frac{1}{(x-t)}\frac{df(t)}{dt}dt = \tau(f) \qquad \ldots(2.10)$$

In their original papers [18,19], the force law τ(f) was chosen to be the simplest form having elastic limit for small displacement ($\tau \approx \mu f/d$) and the periodicity of the lattice; that is a following sine function;

$$\tau = \frac{\mu b}{2\pi d}\sin\left(\frac{2\pi}{b}f\right) \qquad \ldots(2.11)$$

d is the distance between the neighbouring slip planes. In this special case, the solution of (2.10) is found by Cauchy principal to be

$$f(x) = \frac{b}{\pi}\tan^{-1}\frac{x}{\zeta}+\frac{b}{2} \qquad \ldots(2.12)$$

The parameter

$$\zeta = \frac{d}{2(1-\nu)} \qquad \ldots(2.13)$$

characterizes the dislocation width. The stress required to move the dislocation is called the Peierls stress σ_p and is given by

$$\sigma_p = \frac{2\mu}{(1-\nu)} \exp\left(-\frac{4\pi}{b}\right) \qquad \ldots(2.14)$$

The screw dislocation can be treated similarly to the edge dislocation. The PN integro-differential equation is

$$\frac{\mu}{2\pi} \int_{-\infty}^{\infty} \frac{1}{x-t} \frac{df(x)}{dt} dt = \tau(f) \qquad \ldots(2.15)$$

where the relative displacement f is perpendicular to the x direction. Proceed as outlined above for the edge dislocation and the results for the screw dislocations are the following:

$$f(x) = \frac{b}{\pi} \tan^{-1} \frac{x}{\eta} + \frac{b}{2} \qquad \ldots(2.16)$$

where

$$\eta = \frac{d}{2} \qquad \ldots(2.17)$$

The only notable difference for the screw dislocation is that η replaces ζ, where $\eta=(1-\nu)\zeta$. Thus the width of the screw dislocation, 2η is less than the width of the edge dislocation.

Dislocation Density $\rho(x)$

The PN model has been derived by taking displacements along the slip plane as an equilibrium continuous distribution of infinitesimal dislocations with Burgers vector density ρ [24],

$$\rho(x) = \frac{df}{dx} \qquad \ldots(2.18)$$

so that the Burgers vector of dislocations between x and x+dx is db $= \rho(x)$ dx and

$$\int_{-\infty}^{\infty} \rho(x)\, dx = b \qquad \ldots(2.19)$$

The solution of (2.12) corresponding to the sine force law leads to one maximum on the $\rho(x)$ curve.

The advantage of the PN model is that it takes into account the periodic nature of the crystal and yet is simple enough to apply to imperfect crystals. The chief limitation concerns the simple sine law, which is too crude an approximation for real crystals (as will be discussed later).

Chapter 3. Dislocations in Monolayers

3.1 Introduction

In contrast with three dimensional (3D) solids where two types of dislocations can be found, there is only one kind of dislocation in two-dimensional (2D) systems. It is the edge dislocation, and it essentially corresponds to a missing or extra half line of atoms. Therefore this kind of dislocation is low-energy thermal defect. For this reason dislocations are likely to play an important role in 2D phase changes [25-28].

Earlier papers [29-33] reported studies on dislocations in rare gas monolayers which have an interparticle interaction essentially of the Lennard-Jones potential (LJP) form. The dislocations were found to have extended cores. And 60° vacancy dipoles, which can be considered as linear arrays of vacancies, have energies quite lower than those predicted by elasticity theory. In this thesis I further investigate the vacancy and interstitial dipoles in LJP system to compare their properties with those of a system with a very short range interparticle interaction, the nearest-neighbour piecewise linear force (PLF) interaction [33]. The emphasis is on the asymmetry between vacancy and interstitial dipoles and the angular dependence of their energy. I chose these two interparticle interactions because they have been and are still extensively used to explore new properties of materials whether 2D or 3D. In 2D the LJP has been used in particular to model melting behaviour [28,34], whereas the PLF system has been used in a variety of problems related to the plasticity of solids [33,35-38] including melting [39].

The LJP and PLF systems are still the first systems which come to mind when a simple model for a new property of materials is being sought [40,41]. The PLF system is in particular attractive because, with the triangular lattice in which it usually condenses, it behaves as a continuum model discretized by the finite element method. For these reasons it is important to understand well the properties of the dislocations in these two systems. The fact that one potential is very short range (PLF) and the other relatively long range (LJP) will allow us to comment on the effect of the range of the interparticle interaction on dislocation properties.

Elasticity Theory in 2D

As in 3D, the edge dislocation in 2D can be quantified using the notion of a Burgers vector. First, one follows a closed circuit in the perfect crystal. One then does the same thing on the dislocated crystal. The vectorial difference between the two paths is the Burgers vector as in section 2.2.2. The dislocation is a structural type of defect which distorts the lattice up to infinity. Two dislocations of opposite Burgers vectors (see Fig. 7) form a dislocation dipole. The defect can be viewed as one or more rows of vacancies or interstitials and is a local defect. Dislocations and dislocation interactions have been described by the continuum elasticity theory. For example, the interaction energy between two dislocations of Burgers vectors $\mathbf{b}_1$ and $\mathbf{b}_2$ and of separation $\mathbf{R}_{12}$ is given by equation (2.9).

Because dislocation dipoles are low-energy defects in 2D, it is particular easy to create a dislocation dipole with opposite Burgers vectors, particularly one with $b_1 = -b_2$, $b_1 = a$, where a is the lattice parameter and θ is the angle between $\mathbf{R}_{12}$ and $\mathbf{b}_1$. The energy then takes the following form:

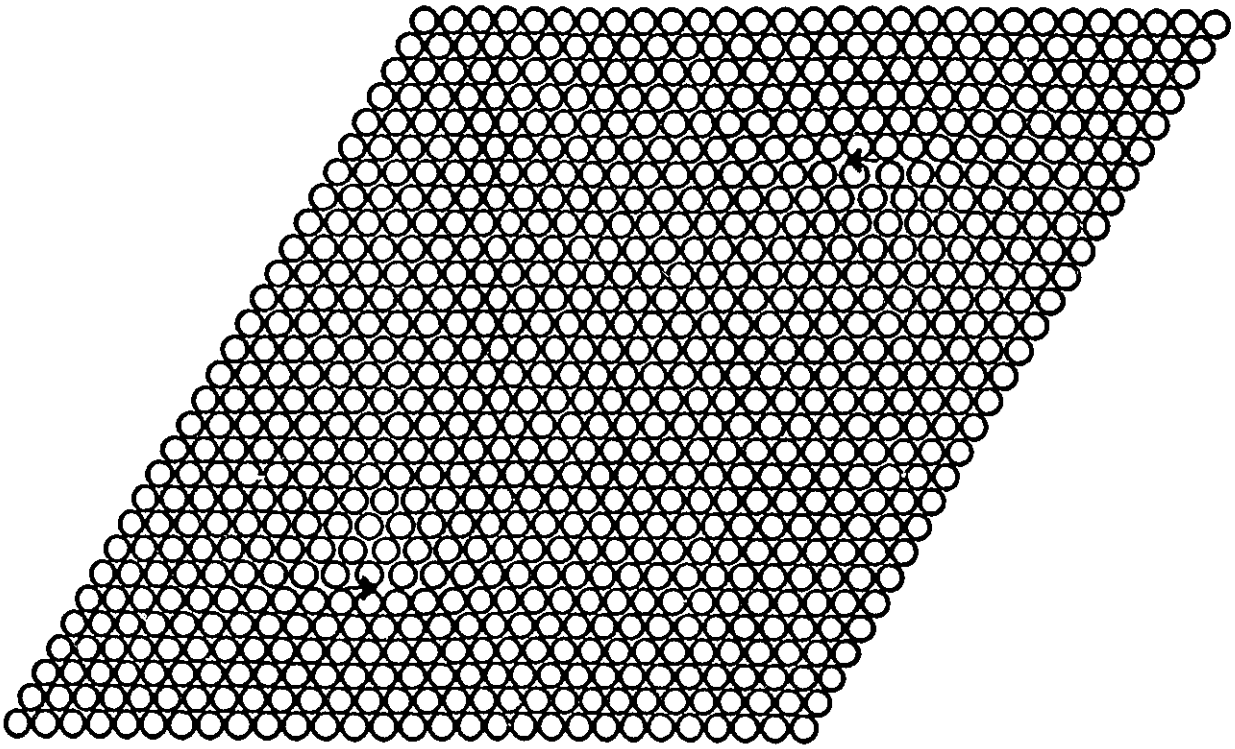

Fig. 7 A dislocation dipole in a triangular lattice. The burger's vectors are indicted in the figure. This is a sample taken from a 91 × 91 system with LJP interactions. The dipole contains 17 vacancies.

$$E_{12} = 2E_c b^2 + Jb^2 [\ln(\frac{R_{12}}{a}) - \cos^2(\theta)] \qquad \ldots(3.1)$$

where E_c is the core energy, J = K/4π where K is the 2D Young's modulus which can be expressed in terms of the two elastic constants λ and μ known as the Lamé constants:

$$K = \frac{4\mu(\lambda+\mu)}{\lambda+2\mu} \qquad \ldots(3.2)$$

The lowest energy dipoles have a Burgers vector b equal to a, the lattice parameter.

3.2 Computer Simulations

We first discuss some general features of computer simulations, which are included in our calculations. The detail simulation models used are presented in the next section. We assume that the system under consideration has a classical model Hamiltonian H. We denote a state of the system by $\mathbf{r} = (\mathbf{x}^N(t), \mathbf{P}^N(t))$, where **P** is the momentum and N is the number of particles in the system. The property A to be calculated should be a function of the states of the system. The quantity A is then given by

$$\langle A \rangle = \frac{1}{Z} \int_{\Omega} A(r)\ f(H(r))\ dr \qquad \ldots(3.3)$$

where Ω is the phase space constituted by the set of states, Z is

$$Z = \int_{\Omega} f(H(r))\ dr \qquad \ldots(3.4)$$

And f is the distribution function of the system. The equation (3.3) is the *ensemble average* with the partition function Z. The distribution function f specifies the appropriate ensemble for the problem at hand.

The ensemble average is, however, not accessible in computer simulations. What we are computing is a *time average*

$$\overline{A_t} = (t-t_o)^{-1} \int_{t_o}^{t} A(\boldsymbol{r}(\tau))\, d\tau \qquad \ldots(3.5)$$

According to ergodicity, we allow the replacement of ensemble averages by time averages

$$\langle A \rangle = \overline{A_\infty} \qquad \ldots(3.6)$$

At this point, one of the two major limitations of computer-simulation methods arises. Clearly a computer simulation cannot follow a path over an infinite time. The *observation time is limited* to a finite path length so that actually the available phase space is a sample of the whole space.

As well as the finite observation time, computer simulation is faced with a second major limitation: *finite system size*. In general, one is interested in the computation of a property in the thermodynamic limit, i,e., the number of particles tends to infinity. Computer simulations allow, however, only system sizes small compared to the thermodynamic limit so that there are possible *finite size effects*. In order to reduce the finite-size effects an approximation is made that has thus far been suppressed, namely the introduction of the boundary conditions. Boundary conditions clearly affect some properties.

3.2.1 Periodic Boundary Conditions (pbc)

Periodic boundary conditions (pbc) are the most popular ones in a simulation of N atoms confined to a volume V, we imagine that volume V is only a small portion of the bulk material. The volume V is called the *primary cell* ; it is representative of the bulk material to the extent that the bulk is assumed to be composed of the primary cell surrounded by exact replicas of itself. These replicas are called image cells. The image cells are each the same size and shape as the primary cell and each image cell contains the same N atoms, which are *images* of atoms in the primary cell. Thus the primary cell is imagined to be periodically replicated in all directions to form a macroscopic sample of the substance of interest. In order to fill all the space, it is important that the shape of volume V is regular. This periodicity extends to the positions and momenta of the images in image cells.

In the course of the simulation, as an atom moves in the primary cell, its images move exactly the same way in the neighbouring image cells. Thus, as an atom leaves the primary cell, one of its images will enter through the opposite face. There are no walls at the boundary of the primary cell. A two-dimensional version of such a periodic system is shown in Fig. 8. The rhombic shape primary cell is labelled A.

It is important to make sure that contributions of the image atoms have only a slight effect on the properties of the primary cell which we are interested in. In this case, we have to choose the size of the primary cell carefully to make it big enough to exclude the image effects and small enough to be manageable. The correct size of the primary cell depends both on the range of the interaction potential and the properties under investigation. For long range interparticle interactions, the size of the cell tends to be larger. However, if we are only

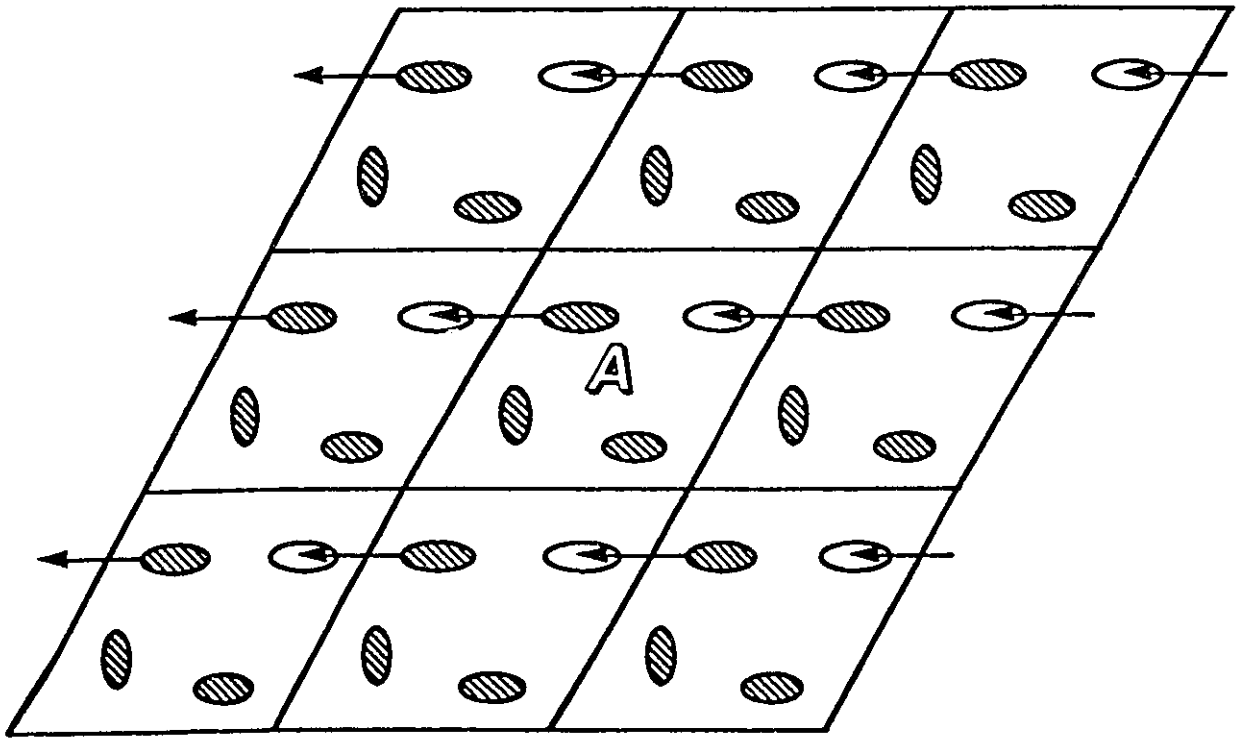

Fig. 8 A two-dimensional periodic system showing the rhombic shape primary cell *A*. Atoms can enter and leave each cell across each of the four edges. In a three-dimensional system atoms would be free to cross any of the six faces.

concerned about the average energy of the cell, we can use a small cell. But if what we investigate involves in part of the cell, say, the energy of the dipole, the size of the cell needs at least to be 2-3 times the length of the dipole.

The use of pbc inhibits the occurrence of long-wavelength fluctuations. The periodicity will suppress any atom arrangement on the boundary of the cell. Thus, it would not be possible to simulate a complicated motion of the dislocation which is assisted by extra atoms such as dislocation nucleation.

3.2.2 Calculation of the Forces

The correct calculation of the forces resulting from a given potential model is essential in the construction of a proper simulation program. In general, the potential energy may be divided into terms depending on the coordinates of individual atoms, pairs, triplets etc. :

$$V = \sum_{i} v_1(\boldsymbol{r}_i) + \sum_{\substack{i,j \\ i>j}} v_2(\boldsymbol{r}_i, \boldsymbol{r}_j) + \sum_{\substack{i,j,k \\ i>j>k}} v_3(\boldsymbol{r}_i, \boldsymbol{r}_j, \boldsymbol{r}_k) + \cdots \qquad \ldots(3.7)$$

The Σ with $i>j$ at the bottom indicates a summation over all distinct pairs i and j without counting any pair twice (i.e. as ij and ji); the same care must be taken for triplets etc. The first term in equation (3.7), $v_1(\mathbf{r}_i)$, represents the effect of an external field (for example, the substrate field in a two-dimensional system), which is not included in our calculations. The remaining terms represent particle interactions. The second sum over v_2 is the pair potential which is most important. The pair potential depends usually only on the magnitude of the pair separation $r_{ij} = |\mathbf{r}_i - \mathbf{r}_j|$, and is then written as $v_2(r_{ij})$. The v_3 term in equation (3.7), involving triplets of atoms, depends not only on the magnitude of the pair separations r_{ij}, r_{jk}, r_{ki} but also the bending angles

between those pair separations. The configuration of an arbitrary set of three atoms is shown in Fig. 9 . Atoms are labelled by i, j, k and their position coordinates $\mathbf{r}_i$, $\mathbf{r}_j$, $\mathbf{r}_k$. The vectors which separate the centres of the atoms are defined as

$$\begin{aligned} \boldsymbol{r}_{ab} &= \boldsymbol{r}_a - \boldsymbol{r}_b \\ r_{ab} &= |\boldsymbol{r}_{ab}| \end{aligned} \qquad a \neq b; \qquad a,b=i,j,k \qquad \ldots(3.8)$$

The angles between the separation vectors are θ_{jik}, θ_{ikj}, θ_{kji}. Then the general form of v_3 can be expressed as

$$v_3(\boldsymbol{r}_i, \boldsymbol{r}_j, \boldsymbol{r}_k) = v_3(r_{ij}, r_{jk}, r_{ki}, \cos\theta_{jik}, \cos\theta_{kji}, \cos\theta_{ikj}) \qquad \ldots(3.9)$$

The cosine functions of those angles may be easily calculated from:

$$\cos\theta_{jik} = \cos\theta_{kij} = \frac{\boldsymbol{r}_{ji} \cdot \boldsymbol{r}_{ki}}{r_{ji} \cdot r_{ki}}$$

$$\cos\theta_{kji} = \cos\theta_{ijk} = \frac{\boldsymbol{r}_{ij} \cdot \boldsymbol{r}_{kj}}{r_{ij} \cdot r_{kj}} \qquad \ldots(3.10)$$

$$\cos\theta_{ikj} = \cos\theta_{jki} = \frac{\boldsymbol{r}_{ik} \cdot \boldsymbol{r}_{jk}}{r_{ik} \cdot r_{jk}}$$

since the position coordinate of atom i appears in the potential energy expressions for pair and three-body terms. Hence there will be contributions to the force on atom i from these two sources. These contributions are evaluated by simple differentiation:

$$\boldsymbol{f}_i = \sum_{\substack{i,j \\ i>j}} -\nabla_{\boldsymbol{r}_i} v_2(r_{ij}) + \sum_{\substack{i,j,k \\ i>j>k}} -\nabla_{\boldsymbol{r}_i} v_3(r_{ij}, r_{jk}, r_{ki}, \cos\theta_{jik}, \cos\theta_{kji}, \cos\theta_{ikj})$$

$$- \sum_{\substack{i,j \\ i>j}} -\frac{\partial v_2}{\partial r_{ij}} \nabla_{r_i} r_{ij} + \sum_{\substack{i,j,k \\ i>j>k}} -\left[\frac{\partial v_3}{\partial r_{ij}} \nabla_{r_i} r_{ij} + \frac{\partial v_3}{\partial r_{jk}} \nabla_{r_i} r_{jk} + \frac{\partial v_3}{\partial r_{ki}} \nabla_{r_i} r_{ki}\right.$$

$$\left. + \frac{\partial v_3}{\partial \cos\theta_{jik}} \nabla_{r_i} \cos\theta_{jik} + \frac{\partial v_3}{\partial \cos\theta_{kji}} \nabla_{r_i} \cos\theta_{kji} + \frac{\partial v_3}{\partial \cos\theta_{ikj}} \nabla_{r_i} \cos\theta_{ikj}\right] \quad \ldots(3.11)$$

We assume that the derivatives of the potentials with respect to pair separations r_{ij}, r_{jk}, r_{ki} and cosine functions $\cos\theta_{jik}$, $\cos\theta_{kji}$, $\cos\theta_{ikj}$ may be readily calculated. The evaluation of the gradients of cosine functions is more complicated. But we first calculate the gradients of pair separations with respect to the $\mathbf{r}_i$

$$\nabla_{r_i} r_{ij} = \frac{r_{ij}}{r_{ij}}$$

$$\nabla_{r_i} r_{jk} = 0 \qquad \ldots(3.12)$$

$$\nabla_{r_i} r_{ki} = -\frac{r_{ki}}{r_{ki}}$$

and the gradients of the scalar products of pair separation vectors with respect to $\mathbf{r}_i$

$$\nabla_{r_i}(r_{ji} \cdot r_{ki}) = -r_{ji} - r_{ki}$$

$$\nabla_{r_i}(r_{ij} \cdot r_{kj}) = r_{kj} \qquad \ldots(3.13)$$

$$\nabla_{r_i}(r_{ik} \cdot r_{jk}) = r_{jk}$$

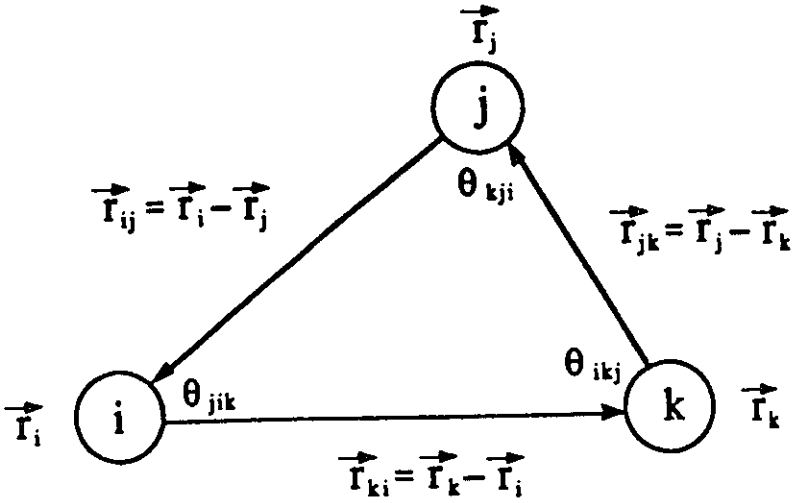

Fig. 9 Configuration of the three atoms i, j, k with position coordinates r_i, r_j, r_k. The angle θ_{jik} is the angle between the r_{ji} and r_{ki} (or r_{ij} and r_{ik}). The pair separation vectors and bending angles are used in calculating the force.

These relations are derived with the help of the identity

$$\nabla(\boldsymbol{A}\cdot\boldsymbol{B}) = (\boldsymbol{B}\cdot\nabla)\boldsymbol{A} + (\boldsymbol{A}\cdot\nabla)\boldsymbol{B} + \boldsymbol{B}\times(\nabla\times\boldsymbol{A}) + \boldsymbol{A}\times(\nabla\times\boldsymbol{B}) \qquad \ldots(3.14)$$

in which the two terms involving $\nabla\times$ vanish for the vectors involved here. The expressions required in equation (3.11) are then

$$\nabla_{r_i}\cos\theta_{jik} = \frac{-r_{ji}-r_{ki}}{r_{ji}\cdot r_{ki}} + r_{ji}\cdot r_{ki}\left[\frac{r_{ji}}{r_{ji}^3\cdot r_{ki}} + \frac{r_{ki}}{r_{ji}\cdot r_{ki}^3}\right]$$

$$\nabla_{r_i}\cos\theta_{kji} = \frac{r_{kj}}{r_{ij}\cdot r_{kj}} + r_{ij}\cdot r_{kj}\left[-\frac{r_{ij}}{r_{ij}^3\cdot r_{kj}}\right] \qquad \ldots(3.15)$$

$$\nabla_{r_i}\cos\theta_{ikj} = \frac{r_{jk}}{r_{ik}\cdot r_{jk}} + r_{ik}\cdot r_{jk}\left[-\frac{r_{ik}}{r_{ik}^3\cdot r_{jk}}\right]$$

The terms in equation (3.15) are easily evaluated during a simulation. In this way the force on each atom i can be calculated.

3.2.3 Pressure

The pressure is another important thermodynamic quantity in the computer simulation. it can be easily calculated from the virial theorem

$$P = \frac{1}{3V}\left[\sum_i m\left(\frac{p_i}{m}\right)\cdot\left(\frac{p_i}{m}\right) + \sum_{\substack{i,j \\ i>j}} f_{ij}\cdot r_{ij}\right] \qquad \ldots(3.16)$$

where $\mathbf{P}_i$ is the momentum of atom i , $\mathbf{f}_{ij}$ is the force acting on atom i due to atom j and V is the volume of the system. In general, the pressure is composed of two parts: (a) the kinetic part due to the momentum carried by the atoms themselves and the (b) static part due to the momentum transferred as a result of forces acting between atoms. The two-dimensional version of equation

(3.16) is given by

$$P = \frac{1}{2A}\left[\sum_i m\left(\frac{\boldsymbol{p}_i}{m}\right)\cdot\left(\frac{\boldsymbol{p}_i}{m}\right) + \sum_{\substack{i,j \\ i>j}} \boldsymbol{f}_{ij}\cdot\boldsymbol{r}_{ij}\right] \qquad \ldots(3.17)$$

where A is the area of the system.

3.3 Computer Models in Two-Dimensional (2D) Systems

I first describe the two systems used in the calculations, they are the Lennard-Jones potential (LJP) system and the nearest-neighbour piecewise linear force (PLF) system. The size of the models, the boundary conditions, and the relaxation algorithm is then discussed.

3.3.1 The LJP System and the PLF System

The LJP or 6-12 pair potential in Fig. 10 is well known. It is given by

$$V_{LJ} = 4\epsilon\left[\left(\frac{\sigma}{r}\right)^{12} - \left(\frac{\sigma}{r}\right)^{6}\right] \qquad \ldots(3.18)$$

The LJP provides a reasonable description of the properties of rare gases, via computer simulation, if the parameters ϵ and σ are chosen appropriately. The potential has a long-range attractive tail of the form $-1/r^6$, essentially due to corrections between the electron clouds surrounding the atoms ('van der Waals' or 'London' dispersion). In addition, for charged species, Coulombic terms would be present. There is a negative well of depth ϵ at $2^{1/6}\sigma$, responsible for cohesion in condensed phases. Finally, there is a steeply repulsive wall at short

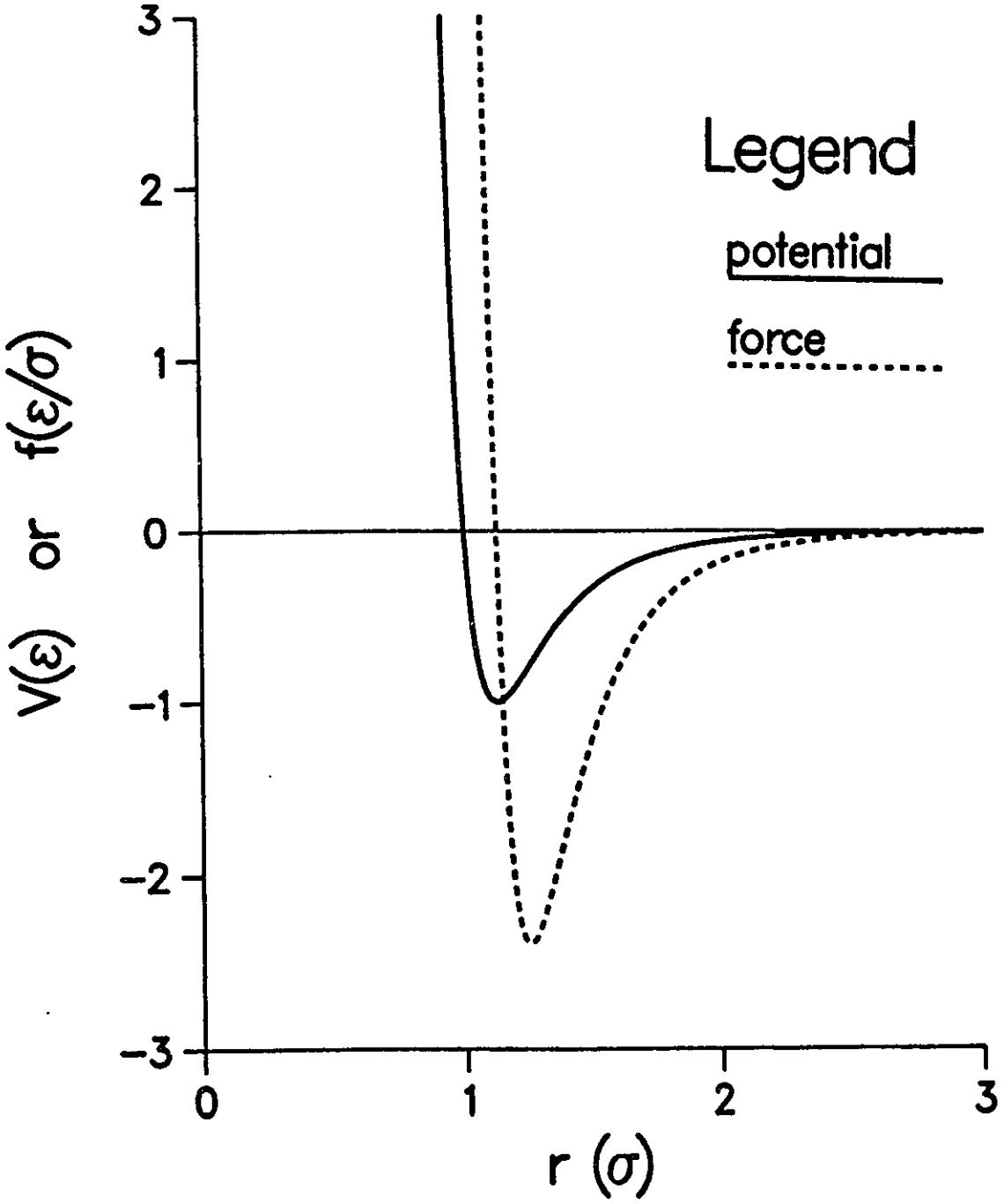

Fig. 10 The Lennard-Jones potential (solid line) and force (dashed line). The unit for potential is ϵ and for force is ϵ/σ.

distances less than $r \sim \sigma$, due to non-bonded overlap between the electron clouds. See in Fig. 10. the force that results from the LJP is

$$f_{LJ} = -\frac{dV_{LJ}}{dr} = 24\frac{\varepsilon}{\sigma}\left[2\left(\frac{\sigma}{r}\right)^{13} - \left(\frac{\sigma}{r}\right)^{7}\right] \qquad \ldots(3.19)$$

By convention, repulsive forces are positive while attractive forces are negative.

Another system which has been studied is the nearest-neighbour picewise linear force (PLF) potential (see Fig. 11). The PLF potential is a simple albeit physical interparticle potential which yields a linear restoring force between the nearest-neighbour particles. The potential is given by

$$V_{PLF}(r) = \begin{cases} \frac{1}{2}\kappa(r-d_0)^2 - \kappa\omega^2, & r \le d_0+\omega, \\ -\frac{1}{2}\kappa(r-d_0-2\omega)^2, & d_0+\omega < r \le d_0+2\omega, \\ 0, & r > d_0+2\omega. \end{cases} \qquad \ldots(3.20)$$

ω is taken to be $0.15d_0$ as in Ref. [38]. There is no strong core repulsion in this potential and this leads, as we will see, to some peculiar properties of the dislocations. The well-depth is $0.0225\kappa d_0^2$ at equilibrium lattice constant d_0. And the attractive part is very short only $0.3d_0$ long. For this short range potential the interactions between the atoms include only the nearest neighbours.

The PLF potential consists of two parabolic functions and the force derived from this potential is continuous and formed by two linear segments:

$$f_{PLF}(r) = \begin{cases} -\kappa(r-d_0), & r \le d_0+\omega, \\ \kappa(r-d_0-2\omega), & d_0+\omega < r \le d_0+2\omega, \\ 0, & r > d_0+2\omega. \end{cases} \qquad \ldots(3.21)$$

As seen from Fig. 11, for all values of $r \le 1.15d_0$, this potential is equivalent to a purely harmonic Hooke's-law interaction.

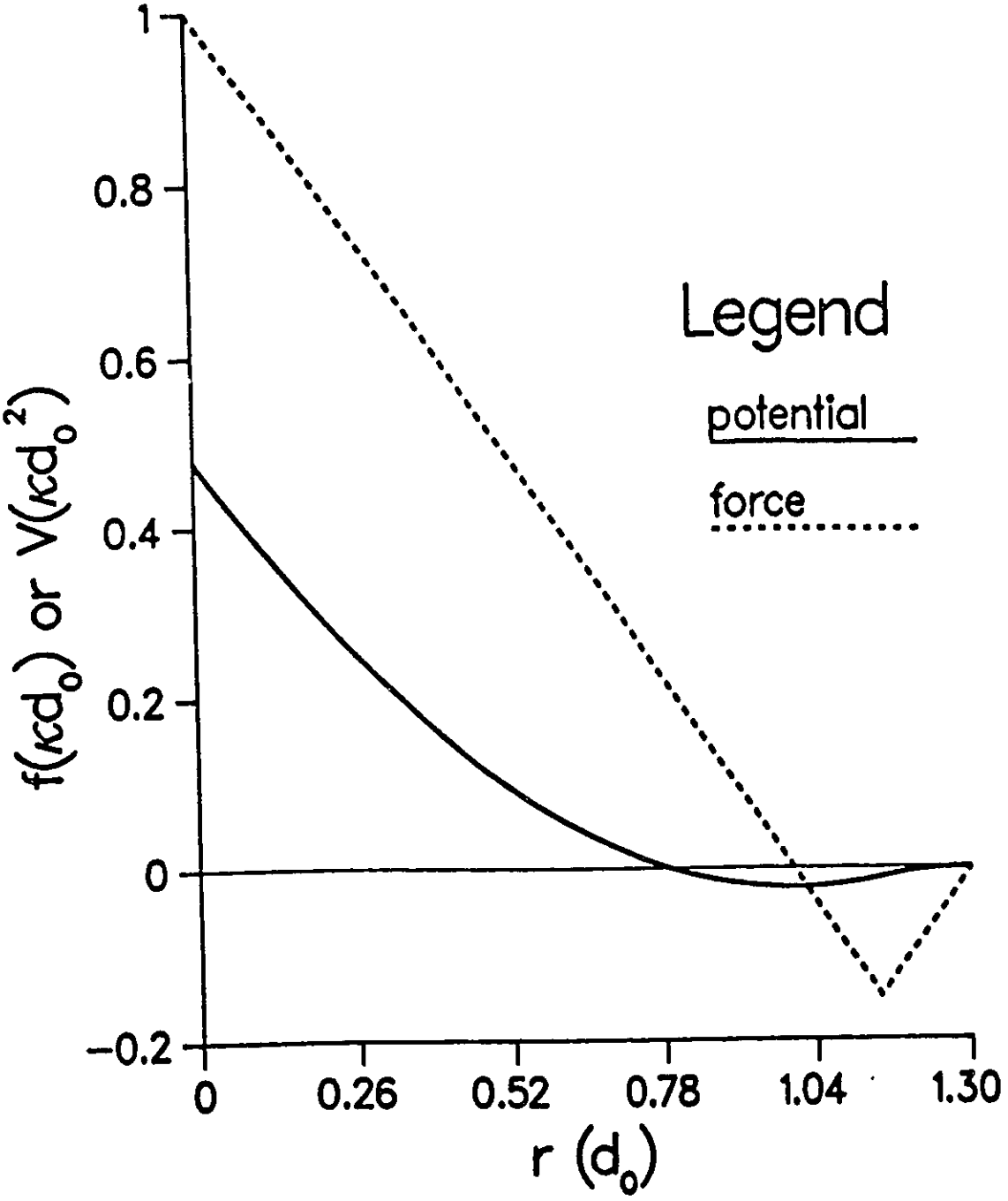

Fig. 11 The nearest-neighbour piecewise linear force (PLF) potential (solid line and force (dashed line). The unit for potential is κd_0^2 and force is κd_0.

3.3.2 Reduced Units

The parameters ϵ and σ are used as units of energy and length, respectively in the LJP system. It is also natural to use the mass of the atom as another fundamental unit. From these definitions, units of other quantities (pressure, force etc) can be determined.

energy	$E^* = E/\epsilon$
length	$L^* = L/\sigma$
mass	$m^* = 1$
density	$\rho^* = \rho/\sigma^2$
pressure	$P^* = P\sigma^2/\epsilon$
force	$\mathbf{f}^* = \mathbf{f}\sigma/\epsilon$

For the PLF system, the parameter κd_0^2, d_0, mass of the atom are used as units of energy, length and mass respectively. The list of other quantities is

energy	$E^* = E/\kappa d_0^2$
length	$L^* = L/d_0$
mass	$m^* = 1$
density	$\rho^* = \rho/d_0^2$
pressure	$P^* = Pd_0^2/\kappa$
force	$\mathbf{f}^* = \mathbf{f}/\kappa d_0$

The use of reduced units avoids the possible embarrassments of conducting essentially duplicate simulations. There are also technical advantages in the use of reduced units. If parameters such as ϵ and σ in the LJP system have been given a value of unity, they need not appear in a computer simulation program at all; consequently some time will be saved in the

calculation of potential energies, forces etc. Of course, the program becomes numerically identical for the thermodynamic variables.

3.3.3 Simulation Model

The Bravais lattices of the system that I have studied are hexagonal. Periodic boundary condition (pbc) is used. It might be noted that when using pbc significant influences on the energy from dipole-image dipole interactions occur only when the dipole separation exceeds about 60% of the block size. To minimize this problem, my computer model consisted of a periodic array of lozenge-shaped disks with atoms from 51 to 91 on the side.

The LJP System

I used a slightly compressed system with a lattice parameter $a = 1.09\,\sigma$ (equilibrium lattice constant is $a_0 = 1.12\sigma$) in order to compare with previous results [29]. This corresponds to the situation occurring for Xe adsorbed on graphite.

The potential was truncated at $3a_0$ where the potential is just about 0.28% of the well depth. Of course the penalty of applying a circular cutoff is that the thermodynamics properties of the model will no longer be exactly the same as for the non-truncated LJP system. Since the potential is real small when the pair separation is greater than the cutoff distance, I am not surprised that the results of the system in which the potential was truncated at $5a_0$ are almost the same as those truncated at $3a_0$.

A dipole was placed in the middle of the system by supposing that the displacements of the atoms from perfect lattice positions are given by elasticity theory--equation (2.5) with Burgers vector b = a. The zero temperature elastic constants for the central LJP interactions are

given by the well known formulae [30].

$$\mu = \frac{1}{4A_0}\sum_l T(l)\,r^2(l) + \frac{1}{4A_0}\sum_l \frac{R(l)-T(l)}{r^2(l)}\,r^2{}_1(l)\,[r^2{}_1(l)-r^2{}_2(l)]$$

$$\lambda = -\frac{1}{4A_0}\sum_l T(l)\,r^2(l) + \frac{1}{2A_0}\sum_l \frac{R(l)-T(l)}{r^2(l)}\,r^2{}_1(l)\,r^2{}_2(l) \qquad \ldots(3.22)$$

where A_0 is the atomic area, r(l) is the distance of the lth neighbour and $r_i(l)$ its ith component. λ and μ are Lamé constant, and ν is Poisson's ratio defined with the additional relation.

$$\nu = \frac{\lambda}{2(\lambda+\mu)} \qquad \ldots(3.23)$$

The force constants R(l) and T(l) are given in terms of the potential V(r) by

$$R(l) = \left.\frac{d^2V}{dr^2}\right|_{r=r(l)}, \qquad T(l) = \left.\frac{1}{r}\frac{dV}{dr}\right|_{r=r(l)} \qquad \ldots(3.24)$$

The displacements produced by the two dislocations forming a dipole are added linearly. Applied to a lozenge shaped disk the formulae (2.5) and (3.22-3.24) produce an additional row of atoms on the edge (for the vacancy dipole) which is removed or a missing row of atoms on the edges (for the interstitial dipole) which is filled. The size of a dipole is decided by the numbers of atoms removed or filled. And the angle of a dipole refers to the angle between the Burgers vector **b** and $\mathbf{R}_{12}$, the vector joining the two dislocations. Fig. 12 shows the configurations of dislocation dipoles of various sizes and different angles. (a) and (b) in Fig. 12 correspond to a 30° and a 60° vacancy dipole with the same size 11 and (c) corresponds to a 60° interstitial dipole with size 15.

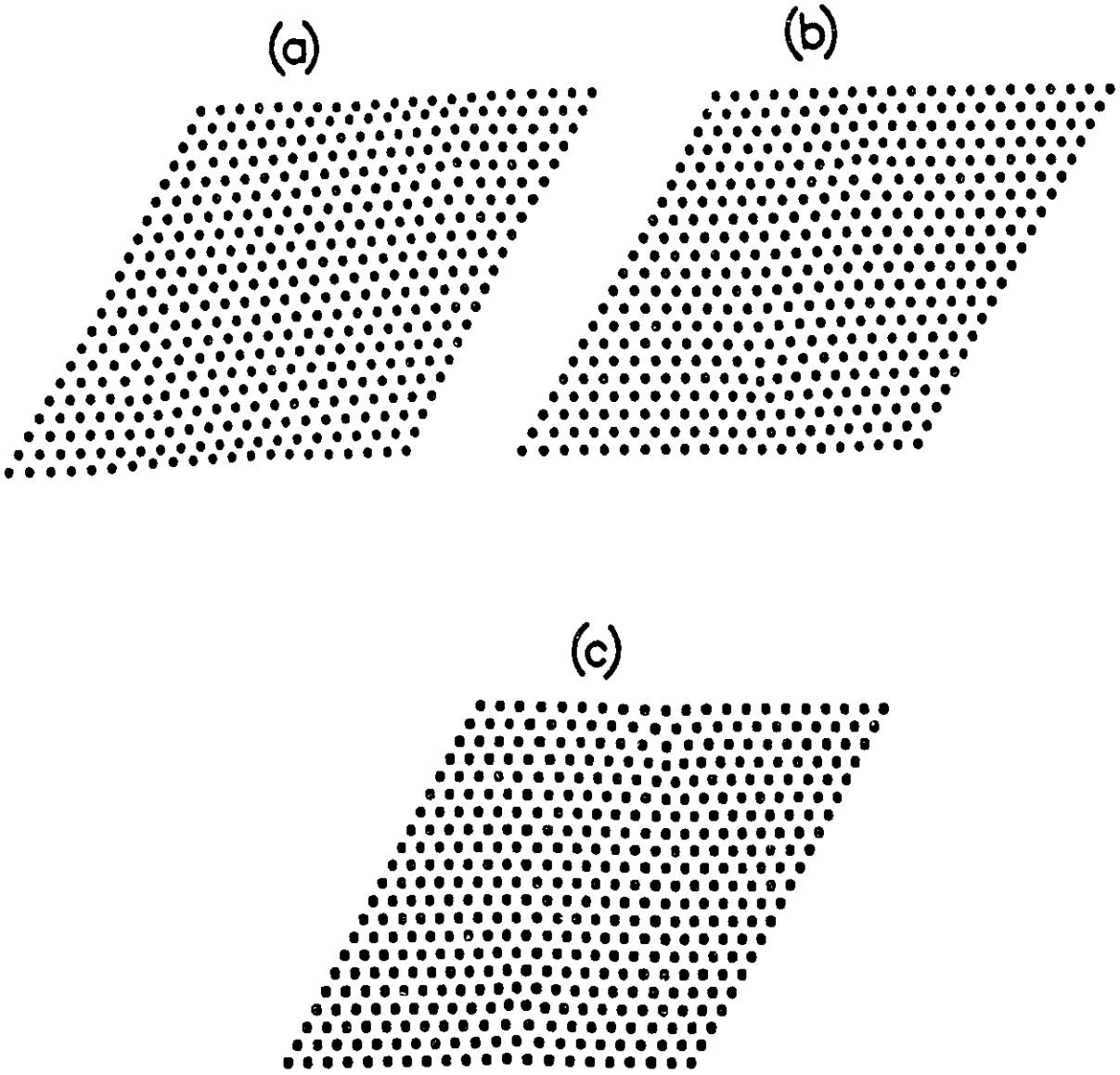

Fig. 12 Configurations of dislocation dipoles with various angles θ , which is the angle between the Burgers vector of the dislocation and the $\mathbf{R}_{12}$ the vector joining the two dislocations, and different sizes the numbers of atoms removed or filled between the dipole. (a) 30° vacancy dipole with size 11 (b) 60° vacancy dipole with size 11 and (c) 60° interstitial dipole with size 15.

The PLF System

The calculations use the same simulation model as in the LJP system - Bravais lattices, boundary conditions. A slightly compressed system with a lattice parameter $a=0.971\ d_0$ (equilibrium lattice constant is $a_0 = d_0$) in order to compare with the LJP system. The Lamé constants are given by [37]

$$\mu = \left(\frac{\sqrt{3}}{4}\right)(4-3\sqrt{\rho})$$

$$\lambda = \left(\frac{\sqrt{3}}{4}\right)(5\sqrt{\rho}-4) \qquad \ldots(3.25)$$

where ρ is the density relative to the stress-free density, i.e. 1.000 and 1.061 for the equilibrium and the compressed system. These elastic constants were used to set up the starting configurations for the dislocations as outlined for the LJP system.

Calculations also used groups of four dislocations placed in the corners of a lozenge so that total Burgers vector of the dislocation group is zero. A typical arrangement of dislocations is shown in Fig. 13. The size of the lozenge is 17a. The arrows in the figure correspond to the Burgers vectors of each dislocations.

3.3.4 Dipole Energy

Since the system simulated is compressed , an artificial external pressurizing fluid is necessary to maintain the system in equilibrium. Calculations must be performed at constant area, while the experimental environment is one of constant pressure p_o. The starting point of all calculations are the solutions given by elasticity theory, which ensures that to leading order

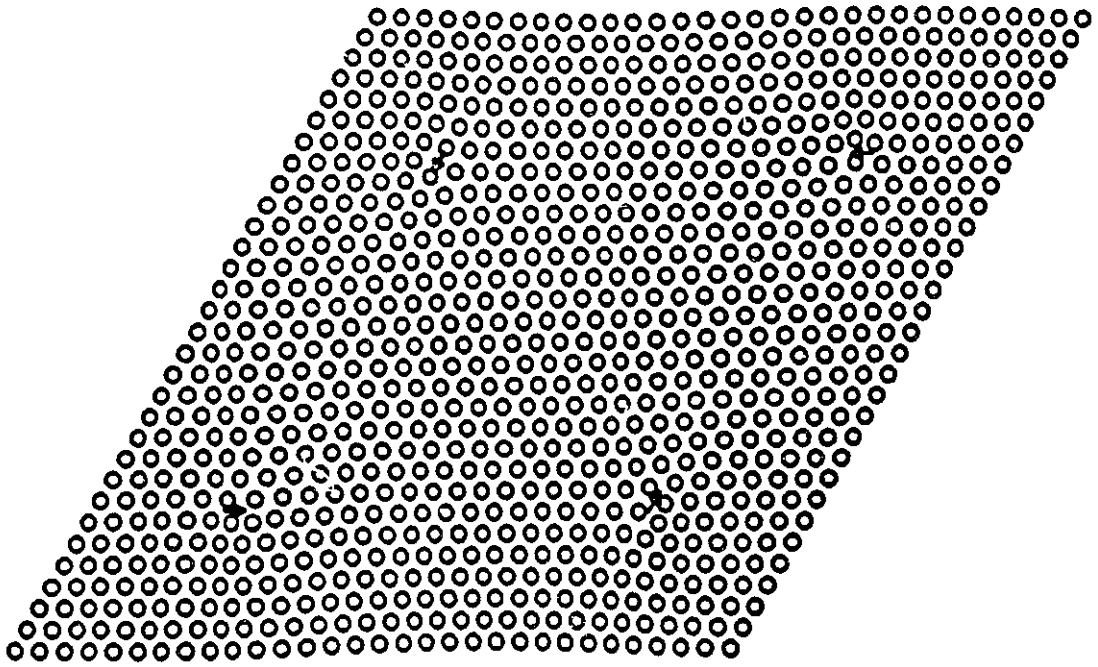

Fig. 13 A Typical dislocation arrangements of a lozenge. Arrows represent Burgers vectors of each dislocation. As we can see that the total Burgers vector is zero for this configuration.

the pressure is maintained at p_o. However, because of contributions from the core region and inelastic behaviour in general, the assembly relaxed at constant area will have an internal pressure p which is not equal to the external pressure p_o, and to allow for this a correction to the constant-area defect energy is necessary. A Tayor expansion with respect to area change $\triangle A$ of the total energy E of the imperfect assembly yields an energy change

$$\Delta E = \frac{\partial E}{\partial A}\Delta A + \frac{1}{2}\frac{\partial^2 E}{\partial A^2}(\Delta A)^2 + p_o \Delta A \qquad \ldots (3.26)$$

The last term is the work done by the external pressurizing fluid. Equation (3.26) can be rewritten as

$$\Delta E = -(p - p_o)\Delta A + \frac{K}{2A}(\Delta A)^2 \qquad \ldots (3.27)$$

where K is a constant. This expression is easily minimized with respect to $\triangle A$ to determine the area change to convert to constant-pressure condition yielding

$$\Delta A = \frac{A}{K}(p_o - p) \qquad \ldots (3.28)$$

It can be verified that the internal pressure after applying the correction (3.28) equals the external pressure p_o. The constant K in correction (3.28), however, depends on the characteristics of the dipoles. A lot of effort have been put into deciding the K for each individual dipole. The energy of a defect E_D is obtained by taking the difference between the energy of a defected system E_1 and a perfect system E_0 with the same number of atoms and at the same pressure and subtracting the work done by the pressurizing environment to deform the system. This work is simply equal to pressure times the area change. In other words, as

illustrated by the following equation, if we take a perfect system and deform it to produce a defect, the energy change E_1-E_0 measured by a simulation consists of the energy of the defect plus the work done by the pressurizing environment:

$$E_1 - E_o = E_D + p(-\Delta A) \qquad \ldots(3.29)$$

If upon introduction of the defect the area change is negative, positive work is done by the environment. On the other hand, if the area change is positive, which is the expected behaviour, negative work is done by the pressurizing environment, and this has to be added to the energy difference between the defected and the perfect systems. The sign in equation (3.29) is easy to understand. If a defect was created the energy difference would simply reflect the energy increase or decrease due to the change in the lattice constant.

3.3.5 Relaxation Techniques

The calculations were performed using static relaxation techniques. During the relaxation procedure, each atom was displaced through a distance proportional to the force until the maximum force fell below a critical value. The area of the system was then adjusted to restore the pressure of the perfect system. The system was considered to have reached the ground state when the maximum atomic motion decreased below 0.00001a immediately after a surface change required to get the exact value of the pressure. Normally, for the LJP system, 8000 relaxation steps were sufficient for a large angle dipole containing 21 vacancies but 20000 steps were required for small angle dipoles. The typical CPU time required for one relaxation procedure is approximately 20000 seconds (5.5 hours) for a LJP system with 91×91 atoms in our mainframe computer system. However, only one fifth of CPU time is required for the same

relaxation procedure in a PLF system. To avoid settling into a metastable state, the system was disordered with random displacements. All the results remain the same.

Neighbour Lists

The most time-consuming part of a computer simulation program is the calculation of the forces on the atoms. For a system of N atoms, forces are computed by sampling, at each time step of the simulation, ½N(N-1) unique r_{ij} distances. But when a truncated potential is used, the force equals zero for any $r_{ij} > r_c$ (where r_c is the potential cutoff distance described earlier which is 3σ for LJP); consequently, evaluating distances r_{ij} that are greater than r_c wastes computer time.

This wasted time can be saved by using a bookkeeping scheme such as that originally devised by Verlet [42]. The computer cell is divided into numbers of small mesh cells with length slightly larger than the cutoff distance shown in Fig. 14, for the LJP, the length of the side of the mesh cell is 3.3σ. For each atom i, say in mesh cell a, the forces acting on the atom i are nonzero only from atoms in cell a and in the neighbouring mesh cells, for 2D, 8 neighbouring mesh cells. The list of those atoms is kept for each atom i, which identifies those atoms that contribute to the force on the atom i. The same neighbour list is used during the simulation and it is updated only when there is an atom crossing the boundary and reentering from the other side of the cell due to pbc. The length of the mesh cell is larger than r_c so that atoms can cross r_c and still be properly considered in evaluating the force on atom i.

3.3.6 Finite Size Effects

As we discussed in 3.2 section, to eliminate the finite size effects is an important

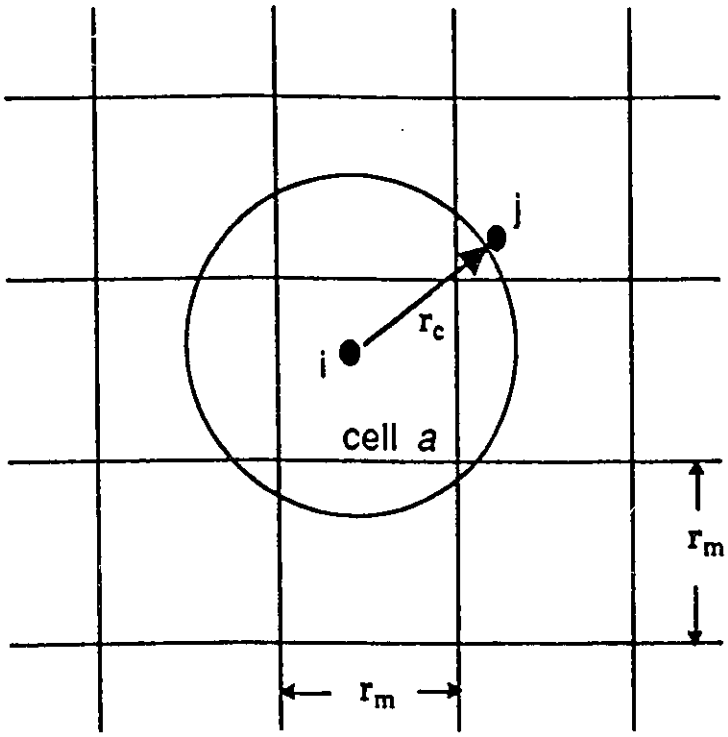

$r_m > r_c$

r_c = cutoff distance

r_m = length of mesh cell

Fig. 14 In the force calculation, the primary cell is divided into smaller mesh cells with size slightly larger than cutoff distance. Contributions to the force $\mathbf{f}_i$ on atom i in mesh cell *a* are nonzero only from atoms j in cell *a* and the 8 neighbouring cells.

consideration in computer simulations. During the computer simulation, we found that the dislocation dipoles in the LJP are mobile whereas for the PLF system they are pinned. This gives us an opportunity to estimate the importance of finite size effects on the energies of dipoles in the PLF system. Our calculations involve atoms, from 2601(51×51), 5041(71×71) to 8281(91×91) in the PLF system, for the same dislocation arrangements. The energies of various sizes of 30^0,60^0 vacancy dipoles and dislocation lozenges in three different PLF systems are listed in Table 3.1.

Plots of energy vs 1/N are shown for 30^0 vacancy dipoles (Fig. 15(a)) and dislocation lozenges (Fig. 15(b)), where N is the number of atoms. The sizes of vacancy dipoles are from 3 to 21 and the sides of the lozenges are from 5a to 21a. It can be seen that the dislocation energy is essentially linear in 1/N as predicted by Ref. 43. The N dependence is large and varies strongly with the dislocation separation and arrangements. For the dislocation dipoles, the N dependence with 1/N has the positive sign and energies of dislocation lozenges have a negative 1/N dependence. And the larger the dipole sizes or the lozenge sizes, the stronger the N dependence. Thus, to get precise values of the energies, extrapolation to the infinite system is required.

However, for our calculations, we are only concerned with the lattice configurations and the general features of the energy variations not the precise energy values of the individual dipoles. As we investigate the dislocations in the different sizes of systems, we found that the configurations and energy variations for both LJP and PLF system remain the same.

TABLE 3.1 Energies of dislocations in finite size PLF systems. N is the number of atoms.

(a) 60^0 vacancy dipoles

dipole size	dipole energy (κd_0^2) N = 8281	dipole energy (κd_0^2) N = 5041	dipole energy(κd_0^2) N = 2601
1	0.1069	0.1067	0.1069
3	0.2733	0.2733	0.2734
5	0.3169	0.3169	0.3174
7	0.3421	0.3423	0.3427
9	0.3615	0.3614	0.3623
11	0.3769	0.3774	0.3785
13	0.3901	0.3907	0.3921
15	0.4018	0.4021	0.4041
17	0.4116	0.4132	0.4151
19	0.4206	0.4218	0.4253
21	0.4293	0.4305	0.4347

(b) 30^0 vacancy dipoles

dipole size	dipole energy (κd_0^2) N = 8281	dipole energy (κd_0^2) N = 5041	ipole energy(κd_0^2) N = 2601
3	0.2835	0.2837	0.2844
5	0.3210	0.3216	0.3236
7	0.3471	0.3484	0.3521
9	0.3672	0.3697	0.3760
11	0.3848	0.3883	0.3981
13	0.3994	0.4050	0.4196
15	0.4132	0.4208	0.4411
17	0.4263	0.4361	0.4634
19	0.4386	0.4512	0.4867
21	0.4508	0.4669	0.5106

(c) dislocation lozenges

size of lozenge (a)	total energy (κd_0^2) N = 8281	total energy (κd_0^2) N = 5041	total energy(κd_0^2) N = 2601
5	0.6173	0.6163	0.6146
7	0.6787	0.6773	0.6742
9	0.7245	0.7218	0.7172
11	0.7545	0.7506	0.7456
13	0.7795	0.7756	0.7683
15	0.8004	0.7957	0.7873
17	0.8183	0.8129	0.8036
19	0.8341	0.8280	0.8178
21	0.8479	0.8413	0.8300

3.4 Dislocation Dipoles in the Lennard-Jones Monolayer

3.4.1 The Core and Interaction Energies

We first looked at the dependence on the size of the dipole. The starting configurations were 60^0 elastic dipoles which are linear arrays of interstitials or vacancies. In the process of

(a)

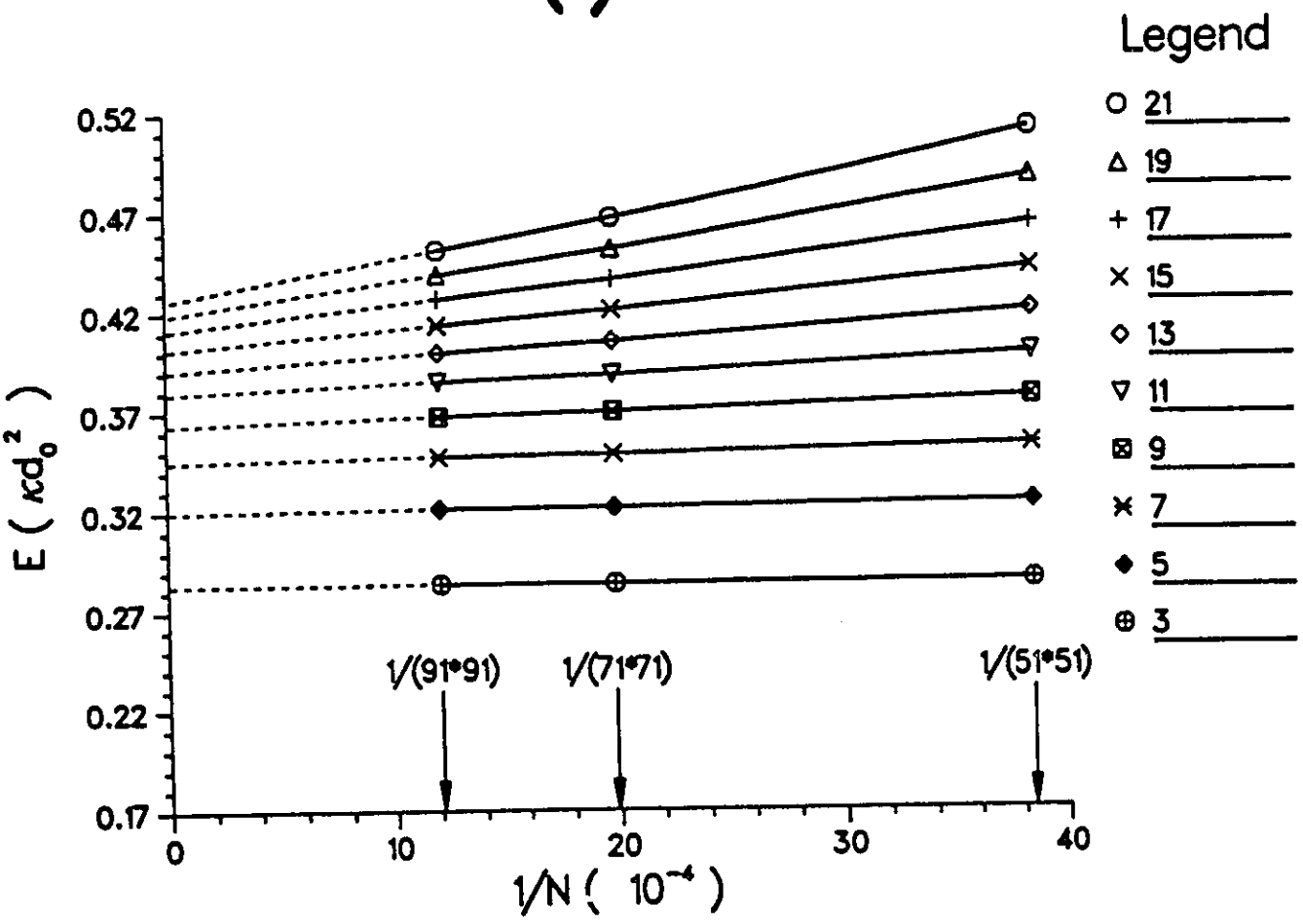
Legend
21
19
17
15
13
11
9
7
5
3
0.52
0.47
0.42
0.37
0.32
0.27
0.22
0.17
E (κd$_0^2$)
0
10
20
30
40
1/N (10^{-4})
1/(91*91)
1/(71*71)
1/(51*51)

(b)

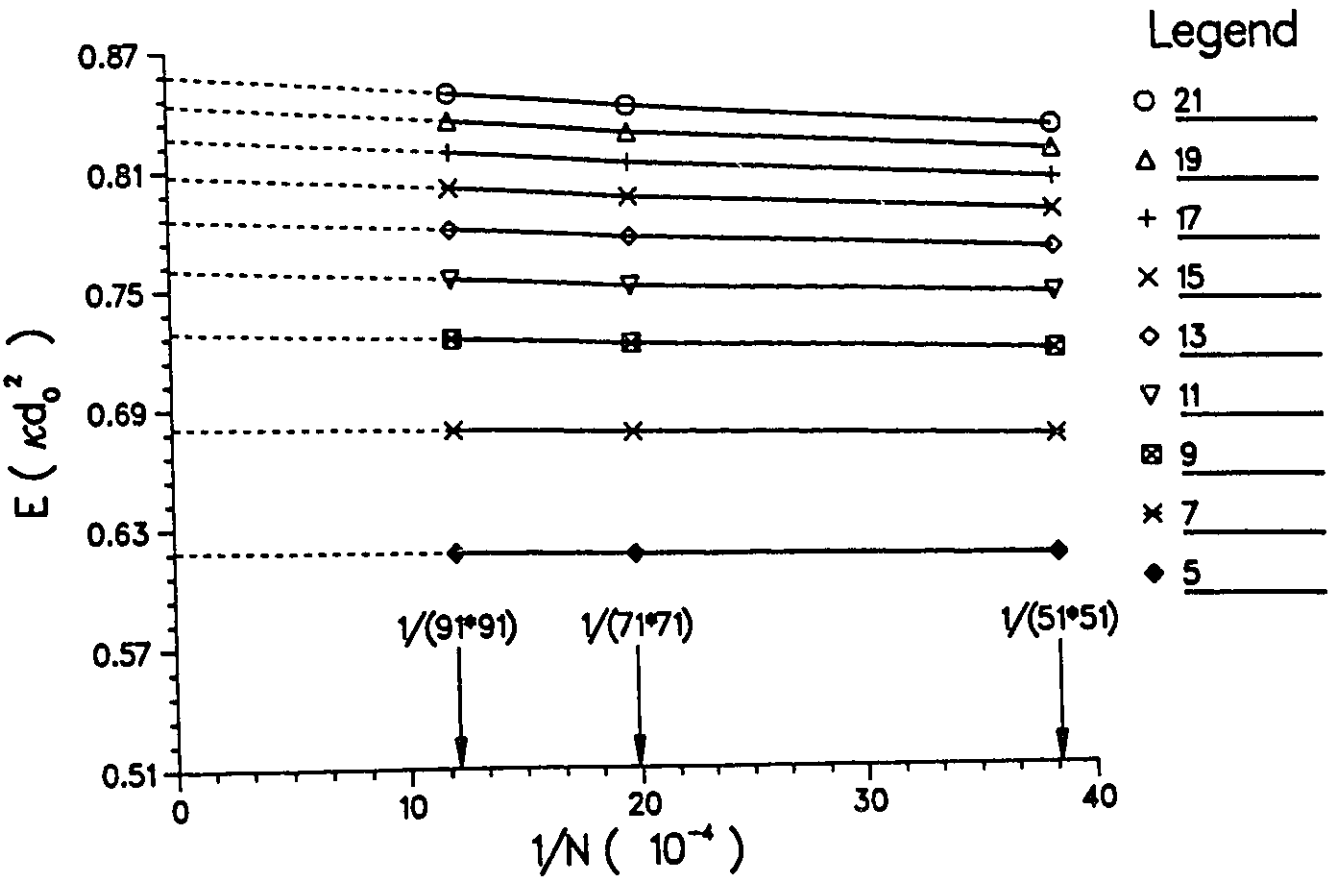

Fig. 15 Energies of dislocations in the finite size PLF system with a = 0.971d_0. The straight lines correspond to our estimates of the linear (1/N) deviations of the energies of the 30° dislocation dipoles (a) and the dislocation lozenges(b) from the infinite-system results. The numbers such as 21,19, ... on the graphs correspond to the sizes of dipoles (a) or sizes of lozenges (b).

relaxation the small residual stresses in the core were sufficient to permit the glide of the dislocation away from the starting 60^0 direction; a consequence of the high mobility of the core in this system [32]. Since the quantities of interest were the core energy E_C and the interaction parameter J we plotted the dipole energy E_{12} as a function of $\ln(R_{12}/a)-\cos^2\theta$ or $\ln(n\sin 60°/\sin\theta)-\cos^2\theta$, where n is the vacancy content of the dipole (see Fig. 16). This eliminated the effect of the glide noticeable in particular for larger dipoles. For our 91×91 size samples, to minimize the effects from the images dipoles in the periodic cells the maximum size we considered was $n=21$. The results of Ref. [29-32] are reproduced. In that reference the full Aziz potential was used for the Xenon and Krypton interparticle interactions which is essentially a Lennard-Jones type of potential. The large departure in the vacancy dipole energy is observed over many lattice sites (~ 15) and appears to remain significant over twice that length. The interstitial dipole becomes rapidly elastic. The difference in behaviour is explained by the asymmetry in the potential between expansion and compression. The hard repulsive core in the interaction potential is to be contrasted with the softness of the large distance interaction. These make the energies of vacancies much lower than that of interstitials. The lowest energy vacancy dipole configurations exploit the low energy of the vacancy. Gliding of the dipole by one atomic line away from the 60^0 configuration creates a five- fold coordinate vacancy (**FCV**) configuration in each core (see Fig. 17). At smaller angles more usual core structures are found (see Fig. 7) but the vacancy character is still quite noticeable. In Fig. 7 a clear linear interface between expanded and compressed regions can be observed which extends over quite a few lattice sites along the Burgers vector. The energy in this core region is mainly in the form of a misfit energy. These are precisely the assumptions inherent in the Peierls-Nabarro model [22].

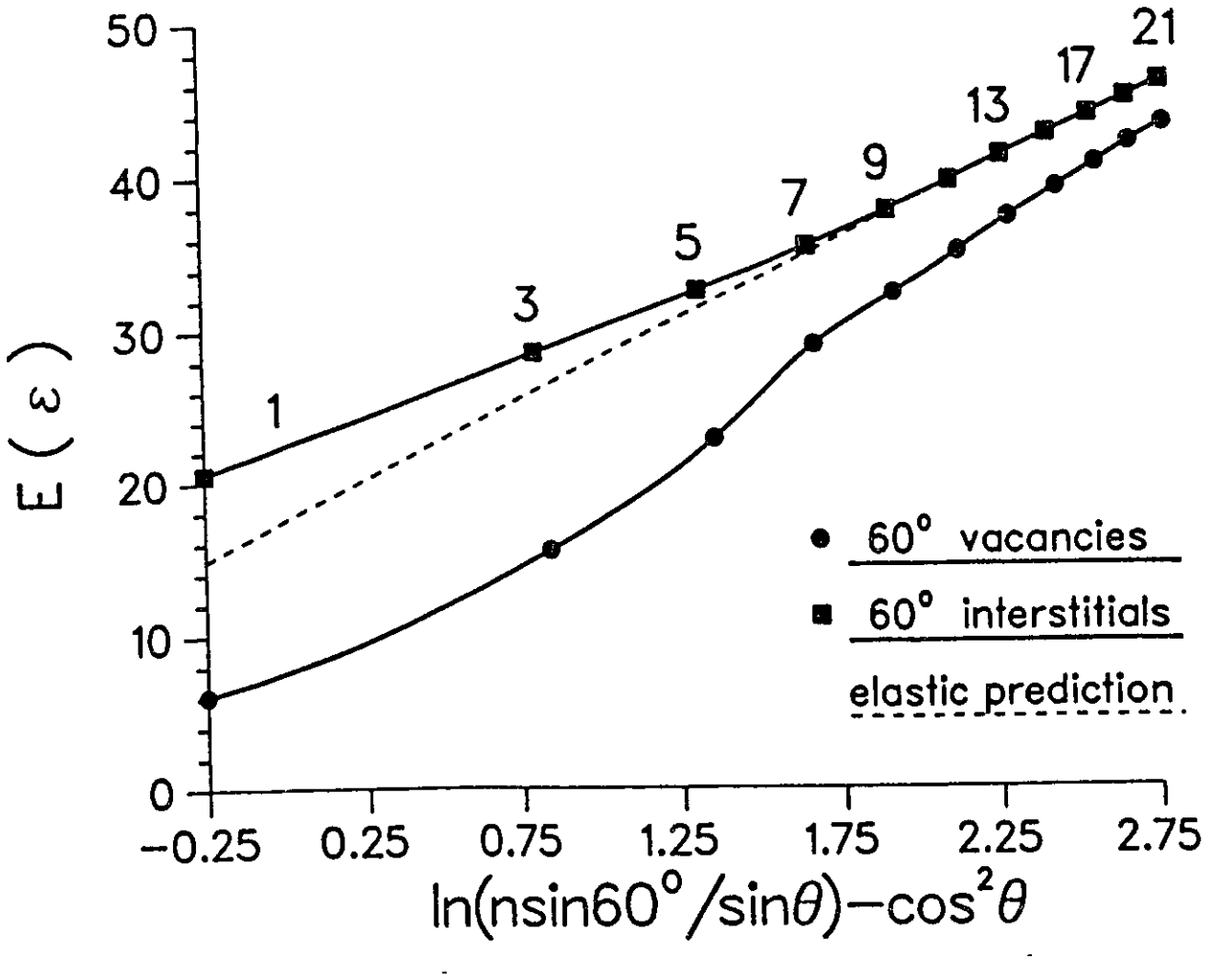

Fig. 16 Variation of the energy of vacancy and interstitial dipoles for LJP system in units of the LJP parameter ϵ as a function of $\ln(R_{12}/a)-\cos^2\theta$. For $\theta = 60^0$ this is equal to $\ln(n)-¼$ where n is the vacancy or interstitial content of the dipole.

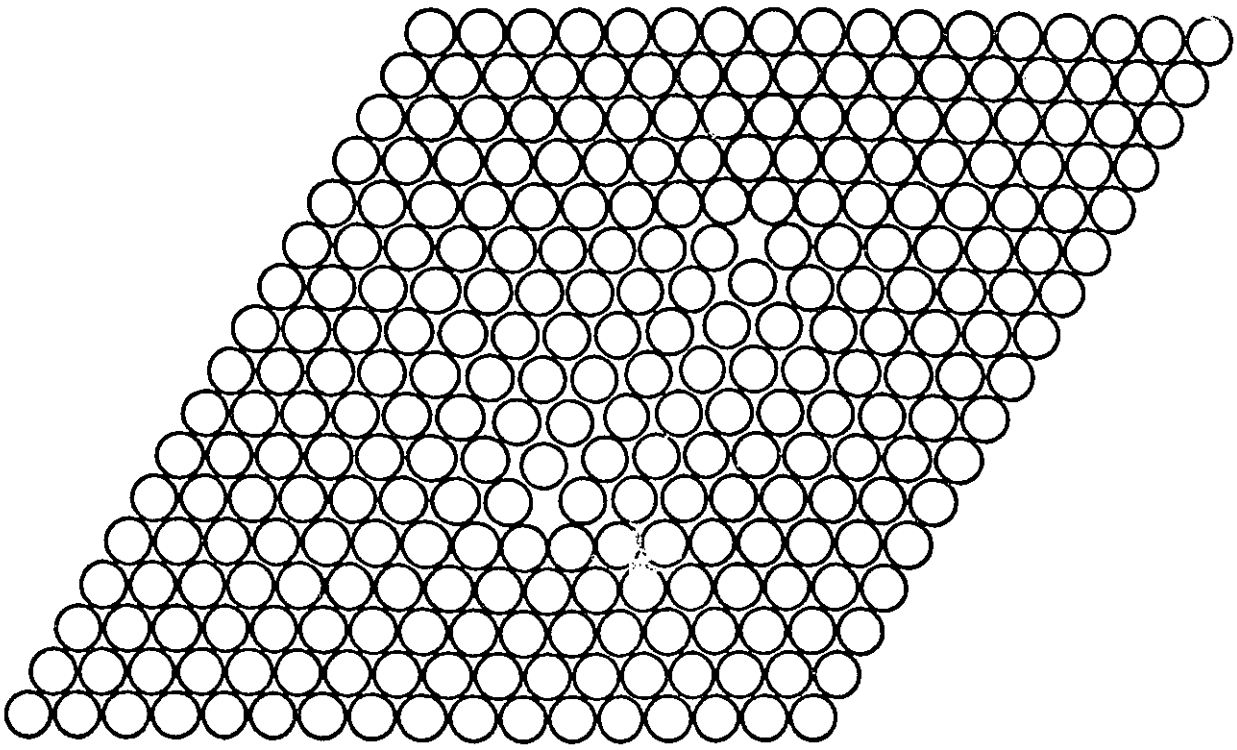

Fig. 17 A five-fold coordinate vacancy (FCV) configuration in LJP system.

The interstitial dipole energy can be used to extract a core energy (E_c). If the elastic value 10.63ϵ is used for J, $E_c a^2 = 8.82\epsilon$ for our system under slight pressure. The quantities E_c and J are sensitive function of the lattice constant [29-32].

3.4.2 Angular Dependence of the Vacancy Dipole Energy

Dislocations glide along the direction of their Burgers vector. In a dipole the two dislocations interact strongly. Elasticity theory predicts, as follows from equation (3.1), that the minimum in the dipole energy occurs at angles 45^0 and 135^0, symmetric with respect to the 90^0 orientation. The FCV configuration competes with the elastic forces to produce a much weaker angular variation than predicted by elasticity theory for angles between 45^0 and 135^0 (see Fig. 18 and 19). Fig. 18 shows the angular variation predicted by elasticity theory. It is a quantity independent of the size of the dipole. There is a local maximum at 90^0 and the rise below 45^0 is fairly rapid. The energy difference between the 45^0 and 90^0 configurations is 0.15J. With the elastic value $J = 10.63\epsilon$ this is 1.59ϵ. What is called "pseudo-elastic" in Fig. 18 is the variation predicted by using the elastic formula of equation (3.1) with E_c and J parameters obtained from the energy variation in the vicinity of the dipole size being considered.

The results of our numerical calculations are shown for a particular size in Fig. 18 and for a variety of sizes of vacancy dipoles in Fig.19.

The same overall behaviour is observed from 21 vacancy dipoles down to sizes as small as 9 vacancies. Between 45^0 and 135^0 the energy variation is significantly smaller than the prediction of elasticity theory. There is still a broad maximum centred around 90^0 but the energy rise is about 0.05J varying little for the different sizes of dipoles (for a 19 vacancy dipole the

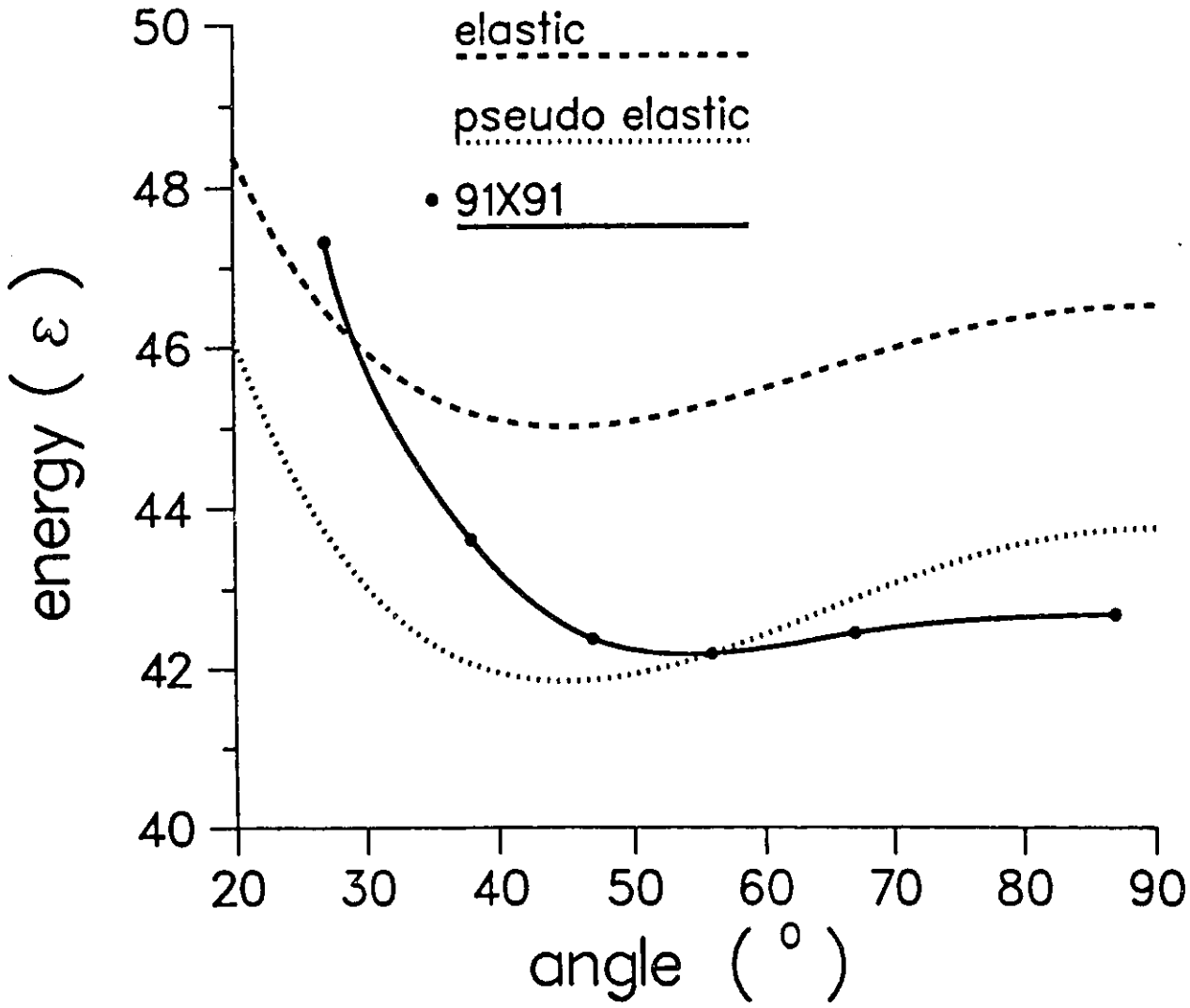

Fig. 18 Variation of the energy of a vacancy dipole of size n = 19 in the LJP system as a function of angle. Both the predictions of elasticity theory and the numerical results are shown. The curve labelled "pseudo-elastic" uses effective J and E_c parameters derived from the energy variation of the vacancy dipoles in the vicinity of n = 19.

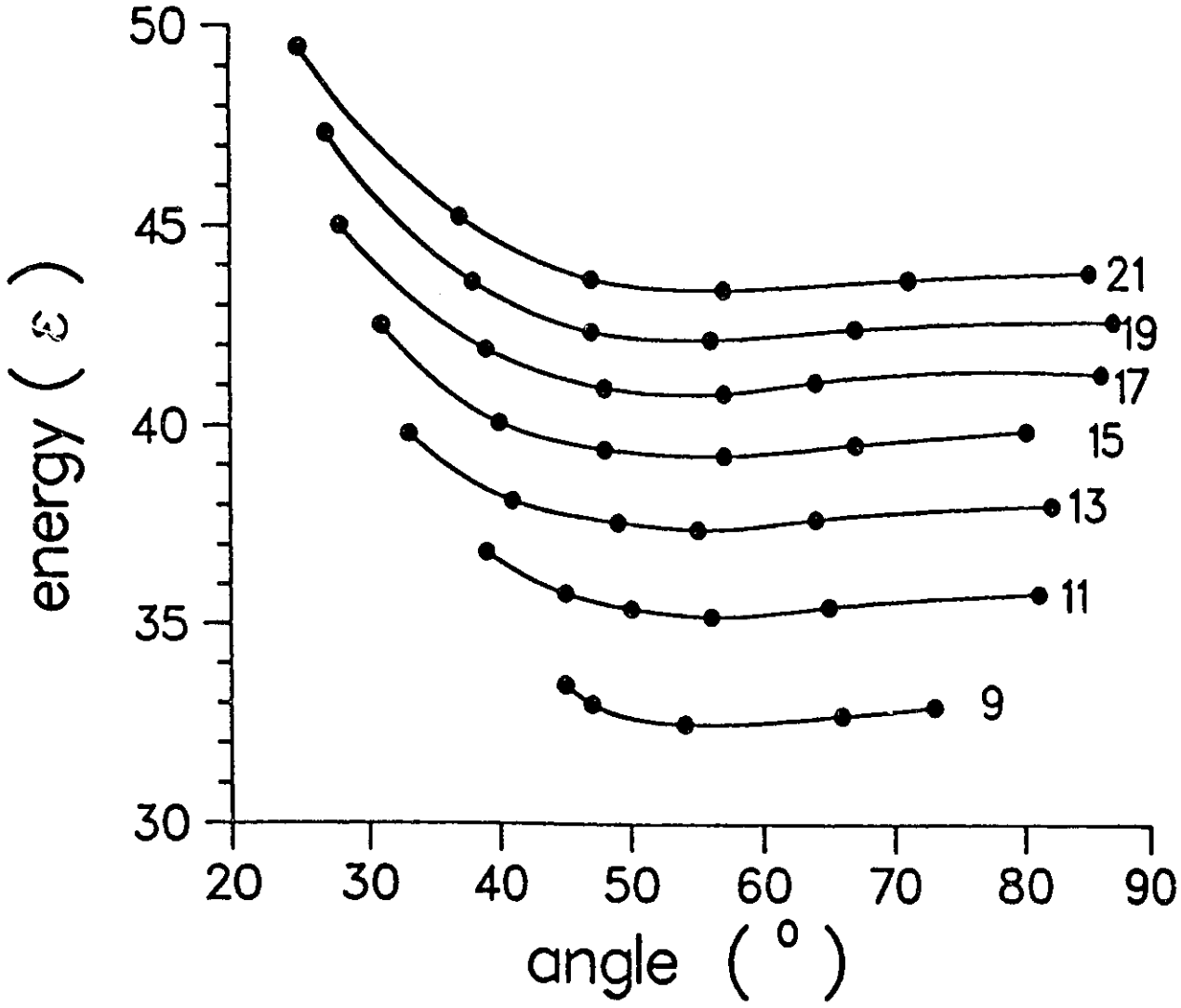

Fig. 19 Variation as a function of angle of the energy of vacancy dipoles of various sizes in the LJP systems. The sizes are measured in terms of the number vacancies in the dipoles.

energy rise is $0.49\epsilon = 0.046J$), and the minimum is closer to 60^0 than to 45^0. The dipoles rest in a broad potential well and the key parameter for the above range of angles is their vacancy content rather than their angles.

3.4.3 The Small Vacancy Dipoles

The small vacancy dipoles have been studied previously [29-32]. Here I discuss some new results obtained by considering different starting configurations with displacements predicted by elasticity theory. The trivacancy when started at a small angle θ relaxes into a triangular configuration but for larger angles (45^0 to 90^0) it relaxes into a linear defect oriented along the 60^0 direction. Interestingly the two defects have exactly the same energy within the accuracy of our calculation. At finite temperature the linear defect is expected to be favoured because of its higher entropy. For the pentavacancy, all initial configurations from 20^0 to 90^0 relaxed into a single arrangement, the 60^0 line of vacancies.

3.5 Dislocation Dipoles in the PLF Monolayer

3.5.1 Dipole Energies

Fig. 20 shows the variation of the energies of 60^0 dipoles for the monolayer with the equilibrium lattice parameter and Fig. 21 for the compressed monolayer. As for the LJP system vacancy and interstitial dipoles do not have the same energy. In this case it may appear a little surprising since the interparticle potential is parabolic and previous studies give no hint of

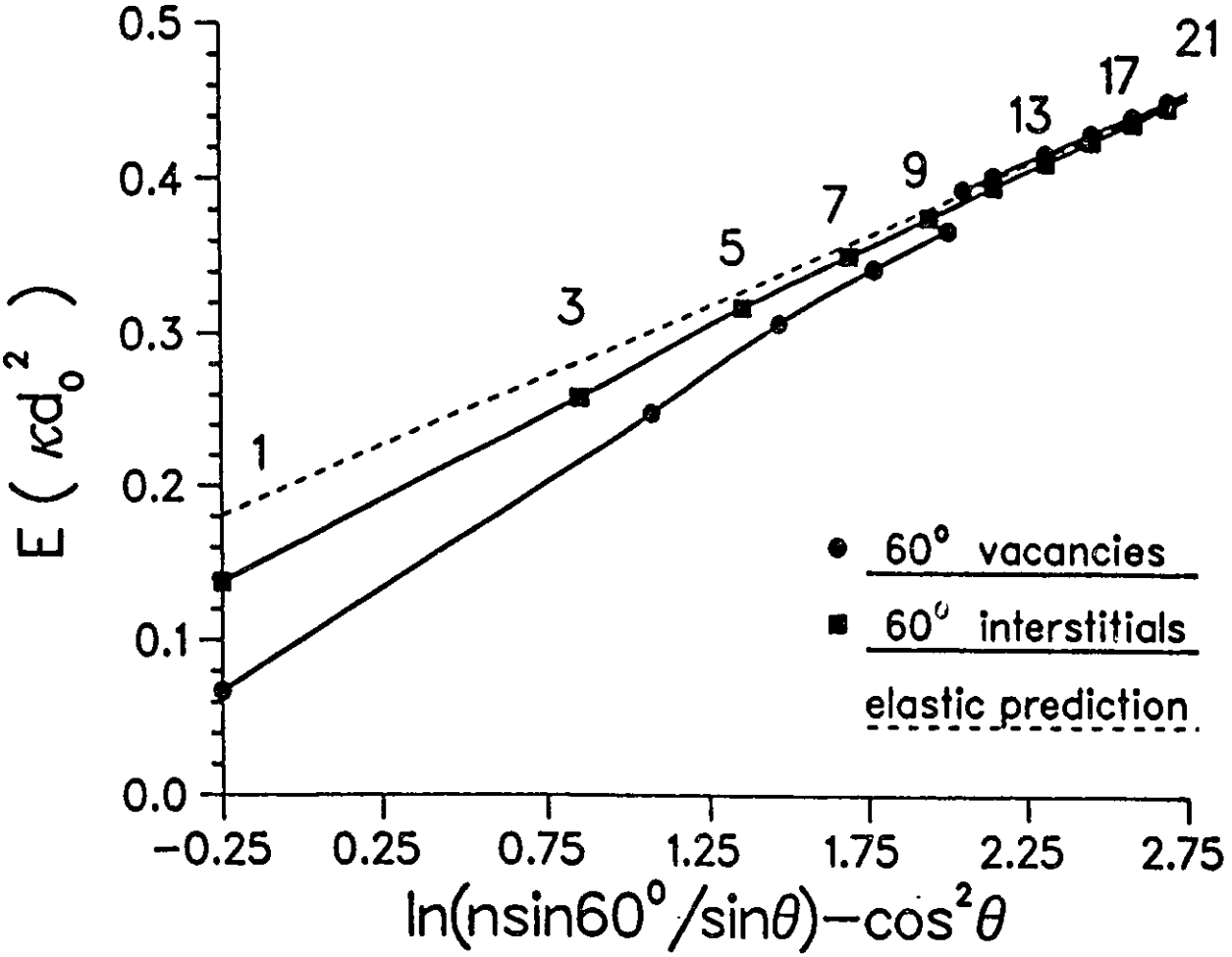

Fig. 20 Dislocation dipole energies in the PLF system for the equilibrium lattice parameter $1.000d_0$.

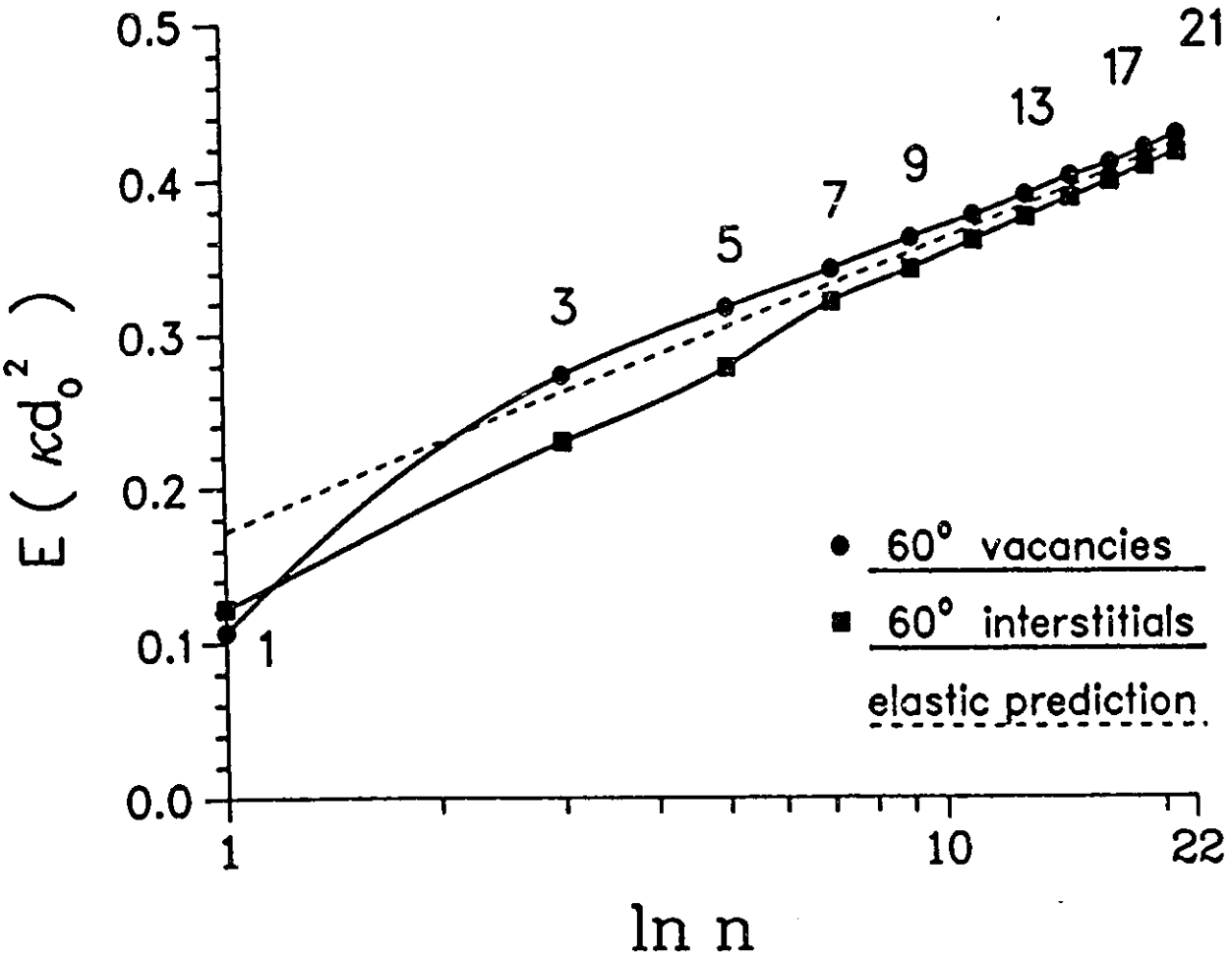

Fig. 21 Dislocation dipole energies in the PLF system for the lattice parameter $0.971d_0$.

significant departure from elastic behaviour [38]. Pressure also changes the behaviour of the system considerably. In general interstitial dipoles are lower in energy than vacancy dipoles. A common feature in this system is that the lattice compresses upon introduction of the dislocation, a result of the weak core repulsion in the PLF force system. The short vacancy dipoles in the uncompressed system are an interesting anomaly very reminiscent of the vacancy dipoles in the LJP system. They are lower in energy than the interstitial dipoles and exhibit a more standard positive area correction. These results can be explained by comparing the energies of the single vacancy and interstitial defects.

The Zero Pressure Lattice

In the zero pressure lattice the monovacancy has a very low energy about half the interstitial defect value. This leads to a situation comparable to that observed in the LJP system. The small vacancy dipoles displace slightly to form a FVC (see Fig. 22(a)) and these dipoles have a lower energy than the interstitial dipoles (see Fig. 22(b)). These latter differ from their counterparts in the LJP system because the weak core in the interaction potential makes the interstitial itself of relatively low energy. The interstitial dipole energies are below the elastic line instead of above as in the LJP system. For dipoles with more than 9 vacancies an abrupt jump in energy is reported in Fig. 20. This reflects a change in character in the vacancy dipole to a behaviour more typical of the PLF system with energies higher than for the corresponding interstitials dipoles. as stated in Ref. [33] with ω =0.15 or a range of $1.30d_0$ the core of the dislocation has one broken bond. This broken bond is on the vacancy side of the core. So it will be on the inside of a vacancy dipole. There will therefore be increased disorder in the region separating the two cores in a vacancy dipole compared with the more ordered configurations

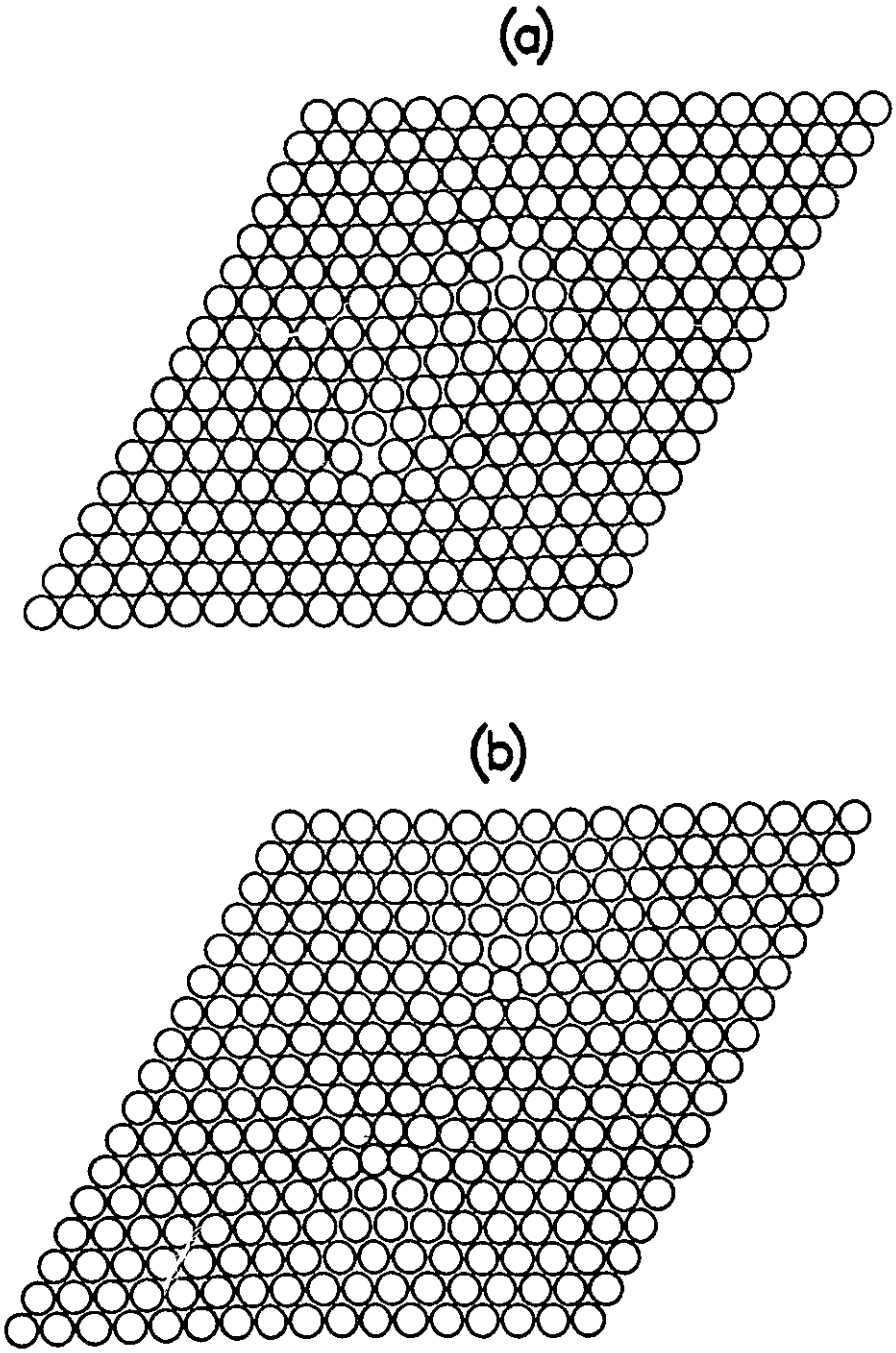

Fig. 22 Typical configurations for small dipoles in the stress free PLF system: (a) vacancy and (b) interstitial dipoles.

observed for interstitial dipoles. We attribute the higher energy of the large vacancy dipoles to this disorder. By carefully choosing the dipole angle in the initial configuration the FCV configuration can be reproduced even for large dipoles yielding energies falling on a curve extending continuously from the small dipole values but these now are special configurations anomalous to the typical behaviour. Except for that very specific configuration the vacancy dipoles will have energies above the corresponding interstitial dipoles with energies close to the 60^0 configuration reported in Fig. 20. This is in contrast with the LJP system where the FCV configuration is a smooth minimum.

The Compressed Lattice

With the application of pressure on the lattice, the vacancy energy rises and the interstitial energy decreases. For the lattice parameter that we have considered $0.971d_0$ the two elemental defects have energies very close to each other. The interstitial dipoles now show energetic behaviour similar to that observed in the vacancy dipoles of the LJP and zero-pressure PLF systems. The five-fold coordinate interstitial is a natural feature of the core so there is no special configuration to comment on (see Fig. 23b). The interstitial dipoles are lower in energy than the vacancy dipoles with the exception of the monovacancy. Fig 23a shows a typical vacancy dipole. Our choice of lattice parameter is the beginning of a reversal in role between interstitial and vacancy dipoles.

Except for the monovacancy all defects show negative area corrections.

3.5.2 Core Energies

The core energies E_C in this system are large compared with the interaction parameters

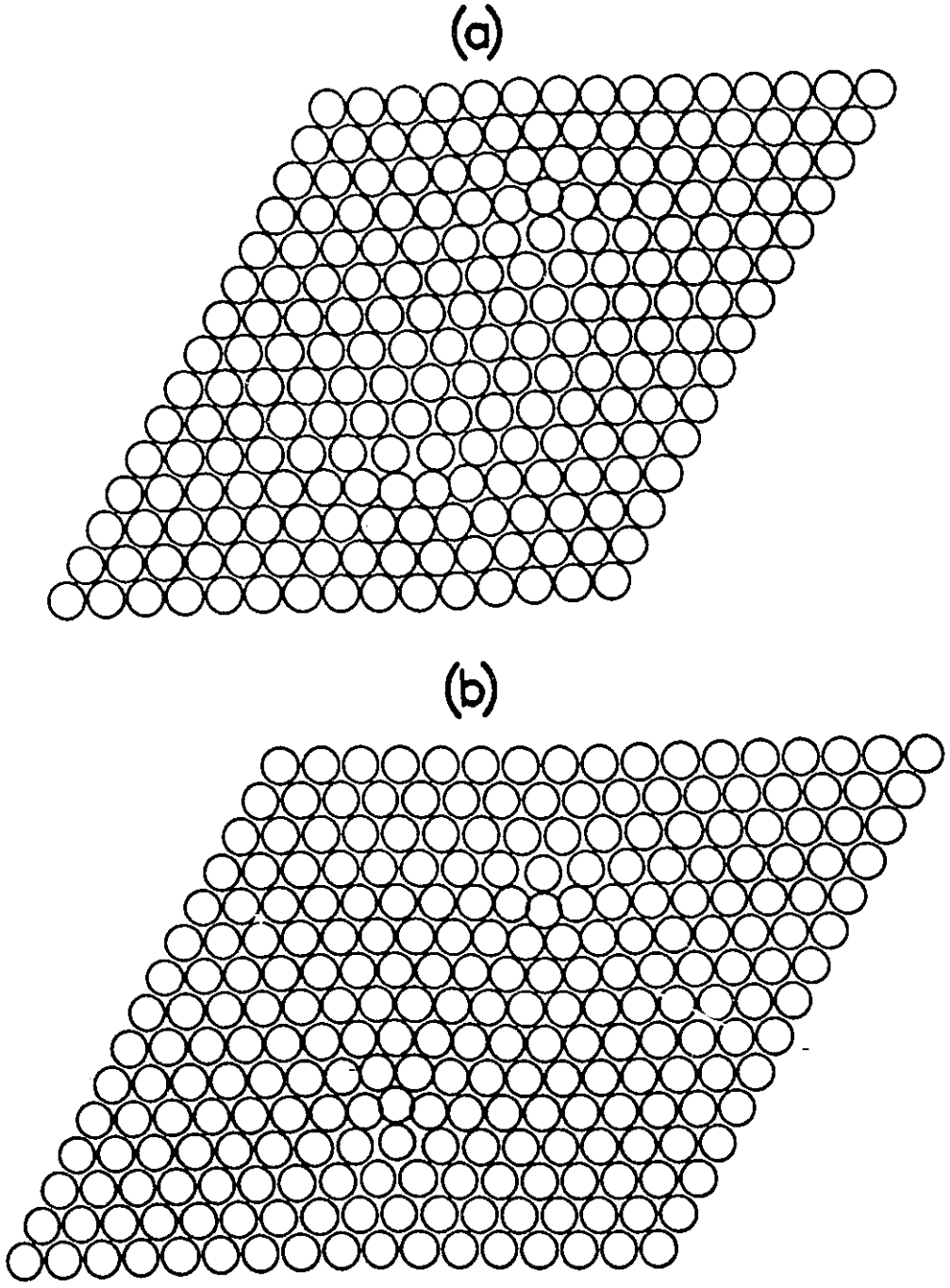

Fig. 23 Typical configurations for small dipoles in the compressed PLF system: (a) vacancy and (b) interstitial dipoles.

J. The ratios E_C/J are consistently higher than one. For the two lattice parameters considered d_0 and $0.971d_0$ using J parameters obtained from elasticity theory, we find E_C equal to $0.1018\ \kappa d_0^2$ and $0.0963\ \kappa d_0^2$, respectively (in accord with Ref. 38 where for lattice parameter of $0.953d_0$ and E_C of $0.0896\ \kappa d_0^2$ is reported.) If our numbers are compared with the corresponding J values $0.0919\ \kappa d_0^2$ and $0.0820\ \kappa d_0^2$, Ec/J is equal to 1.11 for the zero pressure system and 1.17 for the compressed system. The variation of all these energies with pressure differs with the behaviour observed in the LJP system. In the LJP system both the core energy E_C and J increase with pressure [29-32], whereas in the PLF system they decrease, a consequence of the soft core. This suggests that when dealing with problems involving high pressure waves it will be easier to create dislocation pairs in the PLF system.

3.5.3 Angular Dependence of the Dipole Energies

Except for the anomalous configurations involving a FCV the angular dependence is what is predicted by elasticity theory with a minimum at 45^0. Fig. 24 shows a typical result for the compressed lattice. A constant shift is observed from the results of the simulations because the asymptotic elastic regime is not fully reached. The "pseudo-elastic" curve (obtained by using the elastic formula of equation (3.1) with E_C and J parameters obtained from the energy variation) reproduces more faithfully the observed angular dependence of the energy.

3.5.4 Dislocation Lozenges

If we apply the principle of superposition to a dislocation lozenge (see Fig. 14), we expect the energy of the complex to be equal to the sum of the energy of a 30^0 dipole plus the

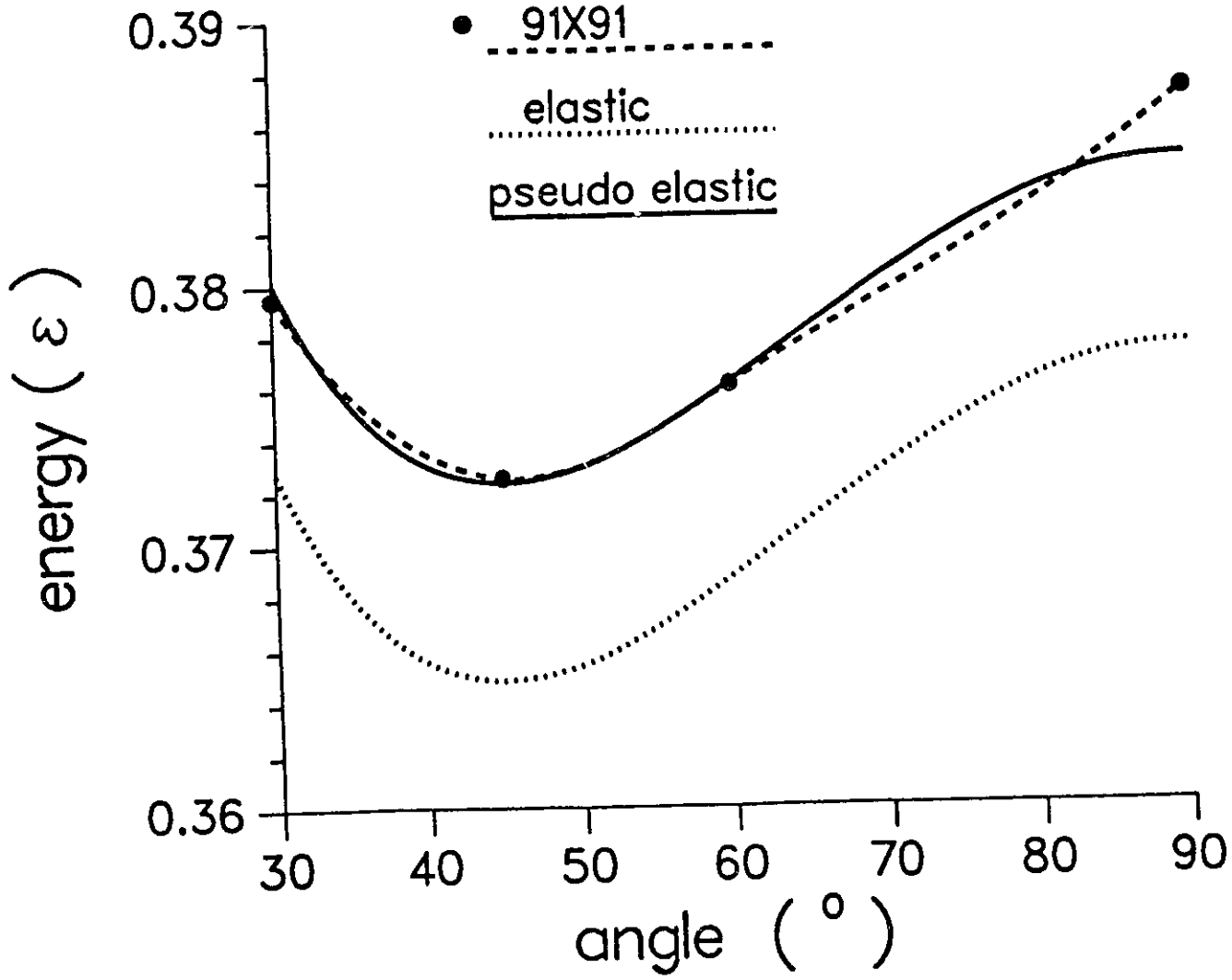

Fig. 24 Variation of the energies of a vacancy dipole with 11 vacancies in the compressed PLF system as a function of angle. The actual data from a system of size 91×91 and elastic theory predictions are shown. "Pseudo-elastic " has the same meaning as in Fig. 18.

energy of a 60^0 dipole plus twice the interaction energy of two dislocations with their Burgers vectors at angle 60^0 and plus twice the interaction energy of two dislocations with their Burgers vectors at angle 120^0. Since the latter two terms cancel each other, the energy of a lozenge is:

$$E \text{ (lozenge)} = E(30^0 \text{ dipole}) + E(60^0 \text{ dipole})$$

The extrapolated energies of dislocation lozenges, 30^0 vacancy dipoles and 60^0 vacancy dipoles are listed in Table 3.2 along with the energies of the sum of two kinds of dipoles.

As we can see from column 4 and column 5, the results of the elastic superposition and the computer simulation of dislocation lozenge are in good agreement.

3.6 Relevance to Melting (if any)

It is interesting to comment here on the debate of the melting of the two-dimensional solid [28,34]. One possible mechanism involving dislocations was proposed a few years ago in a theory developed by Kosterlitz and Thouless [25], Halperin and Nelson [26], and Young [27] (KTHNY) which predicted that the melting of a 2D solid occurred by the unbinding of the dislocations dipoles and proceeded via an intermediate hexatic phase where long range positional order was lost but orientational order was preserved. This was quite unlike the melting transition observed in 3D bulk solid, which is first order. The theory caused a great deal of interest, spawning numerous experimental studies and computer simulations on a variety of 2D systems. But the two types of studies do not agree on the nature of the phase transition [28]. Experiments indicate in some cases a second-order phase transition. Computer simulation however reveals

Table 3.2 Energies of dislocation lozenges (E_4), 30^0 dipoles ($E(30^0)$) and 60^0 dipoles ($E(60^0)$). The units of energies are κd_0^2.

size of lozenge or the size of dipole	$E(30^0)$	$E(60^0)$	$E(30^0)+E(60^0)$	E_4
5	0.3200	0.3168	0.6368	0.6187
7	0.3451	0.3417	0.6868	0.6808
9	0.3635	0.3617	0.7252	0.7289
11	0.3795	0.3761	0.7556	0.7606
13	0.3906	0.3891	0.7792	0.7857
15	0.4014	0.4011	0.8025	0.8078
17	0.4111	0.4092	0.8203	0.8269
19	0.4188	0.4187	0.8375	0.8436
21	0.4259	0.4274	0.8533	0.8582

a more complicated picture. The nature of the phase transition is found to be dependent on the potential used. Melting becomes smoother as interaction potential becomes smoother. The question is whether the trend to smoother melting transitions also coincides with dislocations properties closer to those predicted by elasticity theory.

Several reasons have been pointed out to account for the discrepancy between experiments and computer simulations [28]. I will mention two. First the existence of a third degree of freedom in the experimental studies raises the possibility that the observed continuous transition is not of the KTHNY type. Secondly, the KTHNY theory implicitly relies on two assumptions. The first assumption is that elasticity theory accurately describes dislocation interactions. The second assumption is related to the fact that for the dislocation dipoles to unbind, they have to be able to move freely. Thus the Peierls stress (PS), which is the stress necessary to move one defect by one lattice site, has to be negligible. According to our calculations, we found that in the LJP system dislocations are mobile whereas for the PLF system they are pinned. This means that the PS in the PLF system is much higher than in the LJP system, which indicates that only the LJP system is a suitable candidate for a KTHNY type of melting. Other melting mechanisms have also been proposed such as the grain-boundary theory of melting by Chui [44]. The predictions of these theories also depend on the properties of the dislocations.

If equation (3.1) holds, and if $E_c \sim J$, then it will be energetically favourable for the dipoles to aggregate. The logarithmic dependence of the dipole energy on the separation of the dislocation favours an increase in their sizes and density when the temperature increases. After reaching a critical temperature, the dislocations unbind, effectively destroying the long-range

positional order, but allowing the solid to keep a long-range orientational order. Then, at a second critical temperature, the dislocation cores separate into disclinations, and the solid turns into a true liquid.

Through Monte Carlo simulations on a dislocation vector system, Saito [45] showed that for the small core energy $E_C/J = 0.57$, the melting was first order whereas for the larger core energy 0.82 it was continuous. These are, however, not the actual parameter values used by Saito because in his simulations he used a grid with a lattice parameter of 2a. At a given temperature there is a competition between the creation of new dipole pairs which each require an energy $2E_C + J\ln 2$ when the lattice parameter is 2a and growth of existing pairs which require an energy $J\ln(1+2/R_{12}) \approx 2J/R_{12}$ (for large R_{12}) for an increase of one lattice site. The corresponding values for a lattice parameter of a are $2E_C$ and J/R_{12}. The coarsening of the grid in Saito's simulations would tend to require large core energies to obtain continuous melting behaviour. The values 0.57 and 0.82 correspond to 0.46 and 0.58 in a simulation for a grid of lattice parameter a instead of 2a. What Saito seems to have shown is that for $E_C/J = 0.46$ the melting is first order while for 0.58 it is continuous placing our value of 0.83 of the LJP system decidedly among large core energy values. Within this framework LJP systems are then expected to have a continuous melting transition when they are sufficiently large. If a Saito [45] type of simulation was performed on the PLF system with $E_C/J = 1.17$ a continuous melting transition would also be predicted. However, such a transition is not observed in the molecular dynamics simulations performed by Combs [39]. His simulations support the grain boundary theory of melting of Chui [42]. The possible reason for this discrepancy is that the PS is too high in the PLF system to prevent the simply applying the Saito's results. The question remains as to what

role the extensive core *region* would play beside the finite size effects [28], and whether the melting kinetics are well represented by the type of Monte Carlo simulation done by Saito [45].

3.7 Conclusion

The first overall conclusion is that departures from elastic behaviour are more significant than one would have expected. Even in a system such as the PLF system where the forces are all harmonic, the region where the dipoles behave nonelastically is fairly extended and the asymmetry between interstitial and vacancy dipoles significant. Comparison between the properties of the dislocations in such different systems as the LJP and PLF monlayers shows that the key parameters are the energies of the vacancy and interstitial defects. When the vacancy energy is lower than the elastically predicted core energy value, the lowest energy configuration for a vacancy dipole is a FCV configuration. In the LJP system vacancy dipoles are lower in energy because the LJP system is softer under expansion than compression whereas interstitial dipoles tend to be lower in energy in the PLF system because of its soft core. The non-elastic behaviour is larger in both range and magnitude in the LJP system but it is far from being negligible in the PLF system. In the longer range LJP system the dislocations are harder to form than in the PLF system but easier to move. In the short range PLF system they are easy to form in particular in the compressed systems but hard to move.

These studies therefore reveal that in two dimensions dislocation properties depend sensitively on the nature of the interparticle interactions.

The implications of these results on the melting of two-dimensional solids are mainly in helping to better define the source of the controversy existing on the nature of this transition in two well studied systems. Dislocation core energies are found to be large in both the LJP and PLF systems, in particular in the latter one. A Monte Carlo simulation on a dislocation vector system similar to what has been done by Saito [45] would lead to continuous melting scenarios for both systems. This is, however, not what is observed (see Ref. 34 for LJP systems and Ref. 39 for the PLF system). Maybe the specific properties of the dislocations which are ignored in the Monte Carlo simulation such as the Peierls stress play a key role in the melting kinetics. For LJP system an argument has been made in terms of finite size effects because of the large core region [28]. In the PLF system the short range of the potential inhibits dislocation mobility and could favour the clustering of defects and hence a grain boundary type of melting [42]. The lack of agreement in the predictions of the different approaches demonstrates also the difficulty in simulating the melting of systems where macroscopic defects such as dislocations are expected to play a key role.

Chapter 4. Peierls-Nabarro model of dislocations in silicon with generalized stacking-fault restoring forces

4.1 Introduction

There are several reasons why the study of dislocations in silicon is important. In Si, an elemental covalent semiconductor crystallizing in the diamond structure (Fig. 25), the dislocations have a high-energy and high-frictional resistance. This makes it rather easy to grow crystals with a low dislocation density. Since plastic glide occurs by dislocation motion, Si and, as a matter of fact, the other elements in the same column of the Periodic Table having the diamond structure, are ideal systems for the study of plastic deformation. On the other hand, over the last few years a new generation of optoelectronic devices has been developed from heterostructures made from lattice mismatched Si-Ge alloys [46]. The performance of these devices can be severely impaired by the presence of dislocations. Understanding the properties of these defects is therefore crucial in the design of the new devices.

Quite a few reviews discuss dislocations in Si (see Refs. 47-52], which have been studied for many years. Although the experimental studies are extensive, a comprehensive picture of dislocation generation and mobility is not yet available. The overall geometry and topology of the core structures are understood, but little has been done quantitatively on the microscopic properties such as the Peierls stress of the dislocations and the shuffle-glide controversy [50,51].

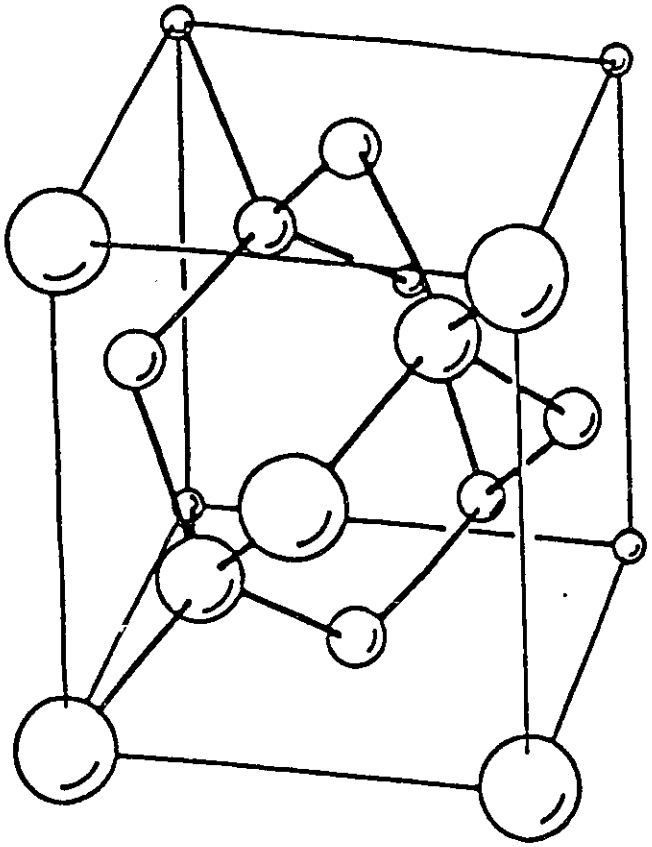

Fig. 25 A diamond cubic unit cell.

The recent first-principles calculations of the generalized stacking fault (**gsf**) energies [53,54] have provided reliable values for the restoring forces occurring close to the core of dislocation. We have replaced the sinusoidal restoring force in the original PN model with the restoring force calculated from gsf and used these results to compute the low-temperature dislocation profiles, core energies, and Peierls stresses for the full and partial dislocations of Si within the framework of the Peierls-Nabarro model [18,19,22]. Vitek and co-worker [55-57] have compared the results of this model with those of atomistic calculations and have shown that for planar dislocations it gives reasonable results. Meanwhile the modern potentials [58] fitted to larger data bases and nominally including electronic effects are expected to provide a better description of dislocations in silicon. In the next chapter, various dislocations are studied by using atomistic relaxation on a silicon lattice modelled by an empirical potential - Stillinger-Weber potential [58]. The comparison of the results from these two models is discussed.

4.2 Dislocations in Silicon

The diamond cubic structure into which Si crystallizes is formed of two interpenetrant face-centre-cubic (fcc) lattices (see Fig. 25). The dislocations are, therefore, expected to be similar in these two crystal structures. In the fcc lattice the main slip plane is the {111} plane and the major slip direction is ⟨110⟩. The smallest Burgers vector is 1/2⟨110⟩. At high temperatures slip has also been observed in the {110} and {100} planes along the same ⟨110⟩ directions. There is a low-energy stacking fault in the {111} plane for the displacement of

1/6⟨112⟩. This permits the dissociation of perfect dislocations into two imperfect dislocations with partial Burgers vectors. For instance,

$$\frac{1}{2}[\bar{1}0\bar{1}] \rightarrow \frac{1}{6}[\bar{2}11] + \frac{1}{6}[\bar{1}\bar{1}2] \qquad \ldots(4.1)$$

Such decomposition reduces dilation and compression on both sides of the slip plane. The imperfect dislocations obtained are glissile on the (111) plane and are known as Shockley partials. These partials are separated by a stacking fault, whose size is determined by the balance of 1/r repulsion between the partials with the attractive force resulting from the stacking fault.

The above characteristics are also found in the diamond lattice. The stacking-fault energy is, however, expected to be even lower than in the fcc lattice. In the diamond-lattice atomic layers come in pairs. So instead of having distortions in the second-nearest-neighbour planes the distortions in the bonds occur in the fourth nearest-neighbour planes. And since, in a covalently bonded structure such as the diamond lattice, atoms interact mainly with their nearest neighbours, these interactions will be weak. For Si one typically quoted value for the intrinsic stacking fault energy is 69 mJ/m^2 or 55 meV/unit cell area [22,50].

In both the fcc and diamond cubic lattices there are two perfect dislocations with Burgers vectors and dislocation lines along ⟨110⟩ directions, a pure screw and a 60° dislocation, the later term arising from the 60° angle between the direction of the dislocation line and the Burgers vector. The difference is that in the diamond cubic lattice there are in principle two distinct {111} glide planes (see Fig. 26), one called the glide plane, situated in between two close-packed planes of different index, and the other the shuffle plane, separating two planes of the same index cutting through bonds oriented perpendicular to the {111} plane. These two planes

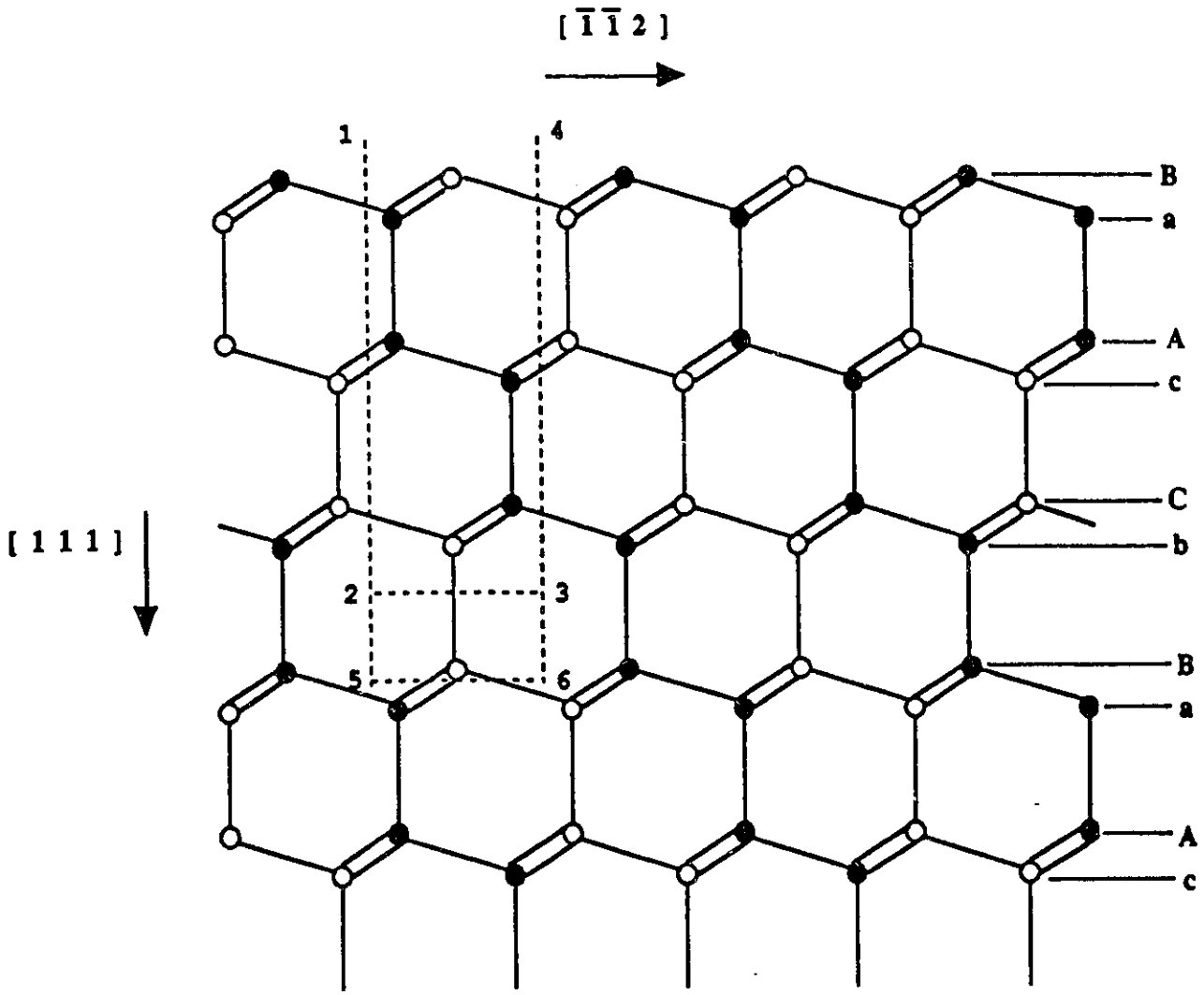

Fig. 26 A diamond cubic lattice projected normal to a (1 -1 0) plane.

lead to two sets of dislocations. The glide set, with properties very similar to those observed in the fcc lattice, can dissociate into two partials separated by a low-energy stacking fault; for the screw two 30° partials and for the 60°, a 30°, and a 90° partial. The dissociation of a 60° glide dislocation into two partials is shown in Fig. 27. They derive their name from the fact that they are believed to undergo glide in the sense of continuum dislocations. In summary, the glide dislocations could dissociate into partials [49,59] and glide in dissociated form [49,60]. This is not the case for the shuffle set, which breaks up two planes of the same index and has no low-energy stacking fault. The dissociation into partials in this case is more complex, and their motion has been argued to be akin to a shuffling motion involving movement of interstitials [22].

Because of covalent bonding, which requires high energy to break or to distort the bond angle, dislocations are expected to be narrow in the diamond structure. Dangling bonds in the core are reconstructed as on surfaces. The width of the stacking fault separating the two partials in a dissociated dislocation is about 40 Å for the screw dislocation and 65 Å for the 60° dislocation [59]. We would expect partials to be nearly decoupled. Experiments by a group in Köln [61,62] and later by another in Poitier [63,64] put them in an intermediate regime between "bound" and "torn away" (using terminology of Ref.[22]). Under applied stress the width of a 60° glide dislocation is observed to be increased if the 90° partial leads and to be narrowed if the 30° partial does. The screw dislocation formed of two 30° partials seems to remain fairly narrow [63,64]. The dissociation width depends on the orientation of the stress. One clear conclusion can be drawn, the 90° partial is more mobile than the 30° partial.

In spite of difficulties to distinguish the glide and shuffle set configurations through high resolution images calculations [65], experimental studies seem to favour glide set dislocations

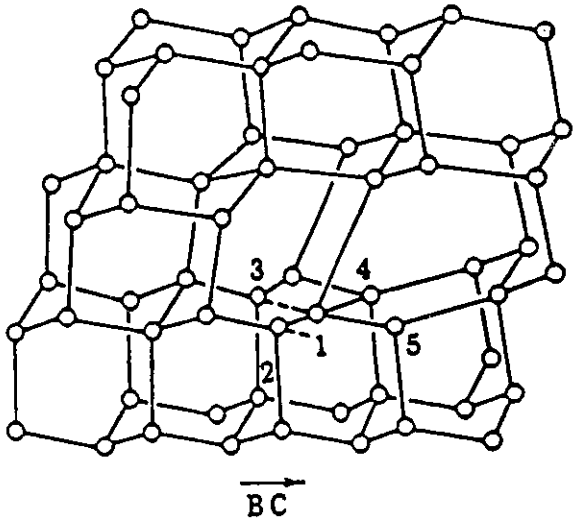

Fig. 27(a) The 60° glide dislocation **BC**.

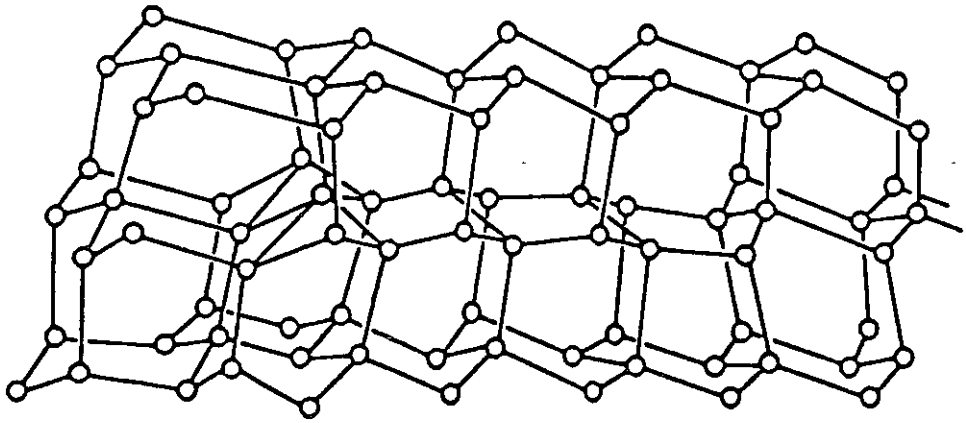

Fig. 27(b) The dissociation of **BC** into 30° partial (left) and 90° partial (right).

over shuffle sets [66-68]. No report so far has been published about the dissociation and motion of the shuffle dislocation. The core structures have also been discussed in detail in several review articles (in particular in Ref. [49]), but the accepted models are not fully consistent with images in high-resolution electron microscopy. Measurements of dislocation mobilities and of electrical activities do not clarify the situation but bring added confusion. We will not discuss these points here but refer to two recent reviews [50,51].

Another important quantity characterizing a dislocation is the Peierls stress, the minimum stress required to move the dislocation from one lattice site to the next. From an experimental point of view, it is usually difficult to obtain the Peierls stress at low temperature due to brittle fracture especially for silicon with high Peierls stress and it is even harder to distinguish the contributions of the different dislocations to the Peierls stress. Nevertheless, attempts have been made to measure the Peierls stress of silicon at a variety of temperatures (as low as 300°C) [69]. The Peierls stress can only be estimated by extrapolating the yield stresses to the absolute zero temperature [70,71] yielding values of about 0.1 to 0.5μ, where μ is the shear modulus of silicon. But this procedure is really crude and brings in a lot of errors.

In the study that follows I will look at the full dislocations in both the glide and shuffle planes and the two partials in the glide plane. These are the dislocations whose glide are expected to be controlled by the Peierls-Nabarro mechanism.

4.3 The Peierls-Nabarro Model

To facilitate the presentation I will adopt the following conventions in all that follows (see Fig. 28). In a Cartesian set of coordinates xyz, the x0z plane is the glide plane {111}. The z axis is the direction of the dislocation line (a ⟨110⟩ line), the x axis the direction perpendicular to it within the glide plane (a ⟨112⟩ direction) and finally the y axis is the normal to the glide plane. The Burgers vector, which is actually the glide direction of the dislocation, lies in the glide plane making an angle θ with the z axis. The dominant direction of displacement of the atoms around the dislocation line is along the Burgers vector. For a pure edge dislocation the Burgers vector would lie along the x axis (or $\theta = 90°$), while for a pure screw dislocation along the z axis (or $\theta = 0°$). A dislocation with any other angle would be mixed, partly edge and partly screw. Its Burgers vector can be decomposed into two components, one along the x axis, the edge component $b\sin\theta$, and the other along the z axis, the screw component $b\cos\theta$.

A continuum theory has been developed, which can be fully solved (see section 2.3). For future purposes, let me just note that for an isotropic crystal an edge dislocation produces in its glide plane, whose normal is along the y axis, a stress field σ_{xy} along its Burgers vector; here the x direction (and hence the two suffixes xy):

$$\sigma_{xy} = \frac{\mu b}{2\pi(1-\nu)}\frac{1}{x} \qquad \ldots(4.2)$$

where μ is the shear modulus and $\nu = \frac{1}{2}\lambda/(\lambda+\mu)$, the Poisson ratio expressed in terms of the conventional Lamé constants λ and μ.

Similarly, for a screw dislocation, whose Burgers vector is along the z direction, the stress along the z direction in the glide plane is

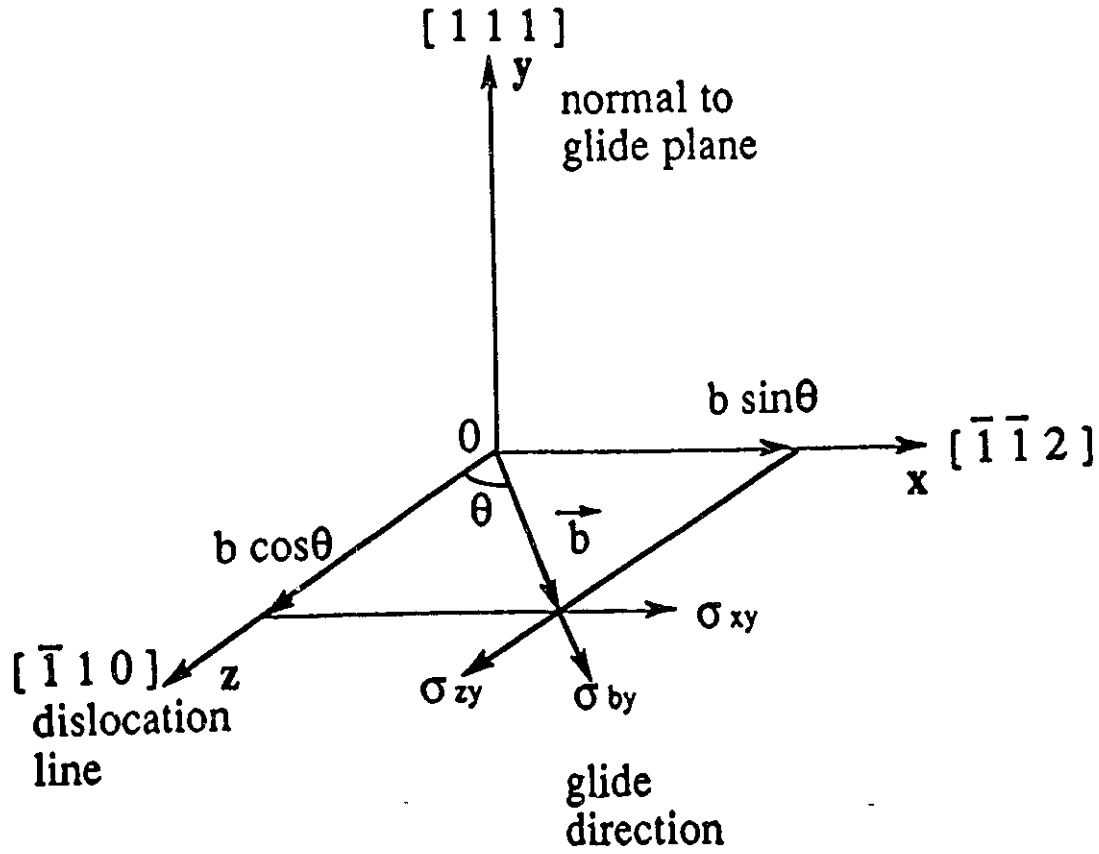

Fig. 28 A Cartesian set of coordinates showing the directions relevant for dislocations in silicon. With the above choice of axes, $\theta = 60°$ gives b along [-101] and $\theta = 30°$ along [-211]

$$\sigma_{zy} = \frac{\mu b}{2\pi}\frac{1}{x} \qquad \ldots(4.3)$$

Equation (4.2) and (4.3) can be easily deduced from equation (2.5) and (2.4) respectively. For a mixed dislocation with a Burgers vector **b** making an angle θ with the z axis, the component of its stress field along the Burgers vector is given by

$$\sigma_{by} = \sigma_{xy}\sin\theta + \sigma_{zy}\cos\theta = \frac{\mu b}{2\pi}\left[\frac{\sin^2\theta}{(1-\nu)} + \cos^2\theta\right]\frac{1}{x} \qquad \ldots(4.4)$$

In the continuum model a dislocation can be displaced without any application of force because the effects of the lattice periodicity are not included. In the Peierls-Nabarro (**PN**) model they are included, for their essential part, in the following way. When a dislocation is present there is a natural interface defined by the glide plane in which the dislocation line lies. The PN model balances at this interface the stress fields predicted by continuum theory with the crystal restoring forces across the interface. The implicit assumption is that the core, the region of inelastic displacements, is spread along the glide plane. This is known to be a good approximation for fcc-type lattices [52]. Specifically, at each point at a distance x from the dislocation line, the stress generated by the displacement **f** of the upper half of the crystal ($y>0$) with respect to the lower half ($y<0$) is viewed as being due to a continuous distribution of infinitesimal dislocations at every points x' of Burgers vectors $\rho(x')dx' = [df/dx]_{x'}\,dx'$. The component of this resultant stress $\sigma_{by}(x)$ along **b** is balanced by the corresponding component of the periodic restoring stress $\tau_b(\mathbf{f})$ acting between atoms on either side of the interface. This equilibrium condition leads to the integrodifferential equation known as the PN equation (see section 2.3 for detail)

$$\frac{K}{2\pi}\int_{-\infty}^{+\infty}\frac{1}{(x-x')}\frac{df(x')}{dx'}dx' - \tau_b(f(x)) \qquad \ldots(4.5)$$

with the normalization condition

$$\int_{-\infty}^{+\infty}\rho(x')\,dx' - \int_{-\infty}^{+\infty}\frac{df(x')}{dx'}dx' - b \qquad \ldots(4.6)$$

K depends on the type of dislocation and the crystalline direction of the Burgers vector. For an isotropic crystal, K follows from equation (4.4):

$$K - \mu\left[\frac{\sin^2\theta}{(1-\nu)} + \cos^2\theta\right] \qquad \ldots(4.7)$$

In the original PN model the restoring stress was taken to be sinusoidal with an amplitude determined by imposing the proper elastic slope. The problem has for this case an analytical solution worth mentioning because it is a reference and a starting point for the general case. The forms used in the original model for an edge dislocation and the general sinusoidal restoring stress are given below

$$\sigma_{xy}(x,0) - \frac{\mu b}{2\pi d}\sin\frac{2\pi f(x)}{b} - \tau_{max}\sin\frac{2\pi f(x)}{b} \qquad \ldots(4.8)$$

where d is the interplanar spacing in the direction perpendicular to the interface, and τ_{max} is the maximum stress that can be generated at the interface. This gives the following PN equation:

$$\int_{-\infty}^{+\infty}\frac{1}{x-t}\frac{df(t)}{dt}dt - \frac{2\pi\tau_{max}}{K}\sin\frac{2\pi f(x)}{b} \qquad \ldots(4.9)$$

Its solution is

$$f(x) = \frac{b}{\pi}\tan^{-1}\frac{x}{\zeta} + \frac{b}{2} \qquad \ldots(4.10)$$

or

$$\rho(x) = \frac{df(x)}{dx} = \frac{b\zeta}{\pi(\zeta^2+x^2)} \qquad \ldots(4.11)$$

where $\zeta = Kb/(4\pi\tau_{max}) = d/[2(1-\nu)]$ can be viewed as the half width of the dislocation, the region wherein the disregistry is greater than one-half its maximum value at x = 0. This is similar to the solution for the Frenkel and Kontorowa [72] or the Frank and van der Merwe [73] model of dislocations (see also Ref. 74). It gives a solitonlike profile with $f(-\infty) = 0$, $f(0) = b/2$, and $f(\infty) = b$ (similar shapes are found in our solutions, see Fig. 32). With the above choice of solution, the lower half plane has an additional plane of atoms. With a negative sign on the $\tan^{-1}$ term, the upper half plane is compressed.

It is to be noted that for every dislocation with sinusoidal restoring forces a solution identical to the one above will be obtained. What changes is only the direction of the displacement field, which is along the Burgers vector and, hence, the elastic constants, which govern the response of the lattice and the interface.

In an actual crystal the restoring forces may be quite different from sinusoidal. Foreman, Jaswon and Wood [75] first considered the effect on dislocation properties of modifying the functional form of the restoring force. The major breakthrough was to derive the restoring force from the gsf energies as had been suggested by Christian and Vitek [76] and applied to bcc crystals by Lejček [77] and Kroupa and Lejček [78]. The gsf of interest to us is obtained by

cutting the crystal along the {111} plane displacing one half with respect to the other by a vector **f** and then rejoining them. The energies of the gsf generate what is known as a γ surface $\gamma(\mathbf{f})$ (energy per unit area). The restoring stress is simply

$$\tau(f) = -\frac{\partial\gamma}{\partial f} \qquad \ldots(4.12)$$

Figure 29(a) and (b) show the gsf energies surfaces for unrelaxed glide and shuffle planes respectively. The unit of energy is eV/unit area of {111} which is equal to 0.0783 eV/Å^2. The unit of x is 1/12⟨110⟩, while y is 1/12⟨112⟩. Those γ surfaces , which I am using, have been obtained from a local-density approximation (LDA) to the density-functional theory (DFT), a first-principle calculation (for details see Refs. 53 and 54). Such calculations are computationally demanding. For this reason fully relaxed atomic configurations were considered for only two points, the lowest-energy barriers in the glide and shuffle planes, known as the unstable stacking-fault energies. In the glide plane this occurs at a displacement of 1/12⟨112⟩ in units of the repeat distance along this crystallographic direction. The metastable stacking fault or intrinsic stacking fault is at 1/6⟨112⟩. For the shuffle plane the preferred slip paths are along ⟨110⟩ directions and the unstable stacking fault occurs for a displacement of ¼⟨110⟩. To construct the variation of the gsf over the two directions of interest, we have scaled the unrelaxed gsf energies by the decrease of the unstable stacking-fault energy for each surface. It is an approximation whose consequence would be hard to assess quantitatively [1] . But I expect the relaxation to be the

[1] More recently Juan and Kaxiras obtained the fully relaxed γ surfaces. They find little change in the <112> directions of the glide plane with the scaled γ surface but significant changes in the other directions. The fully relaxed shuffle plane γ surface is very similar to its scaled counterpart.

(a)

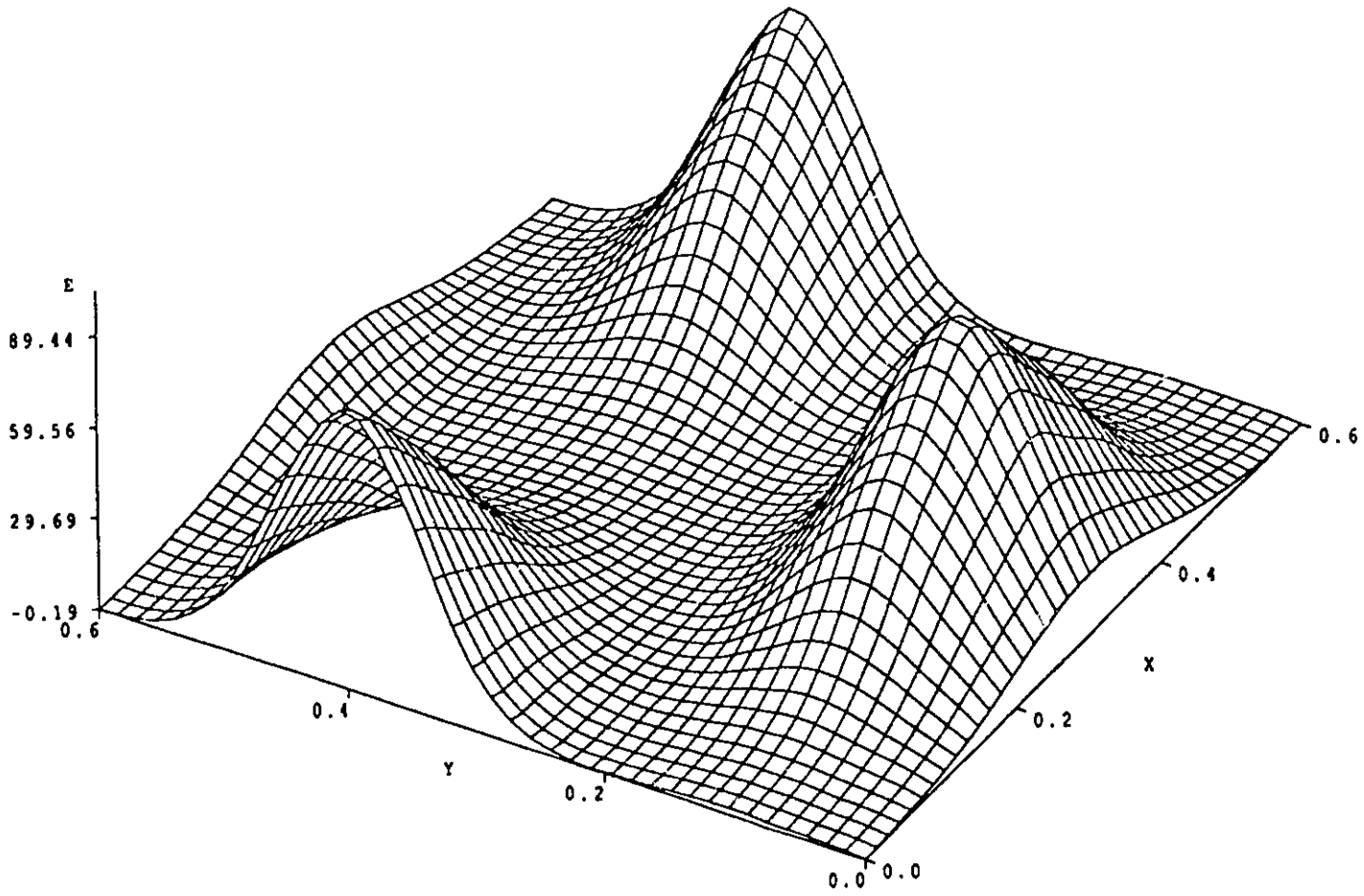

(b)

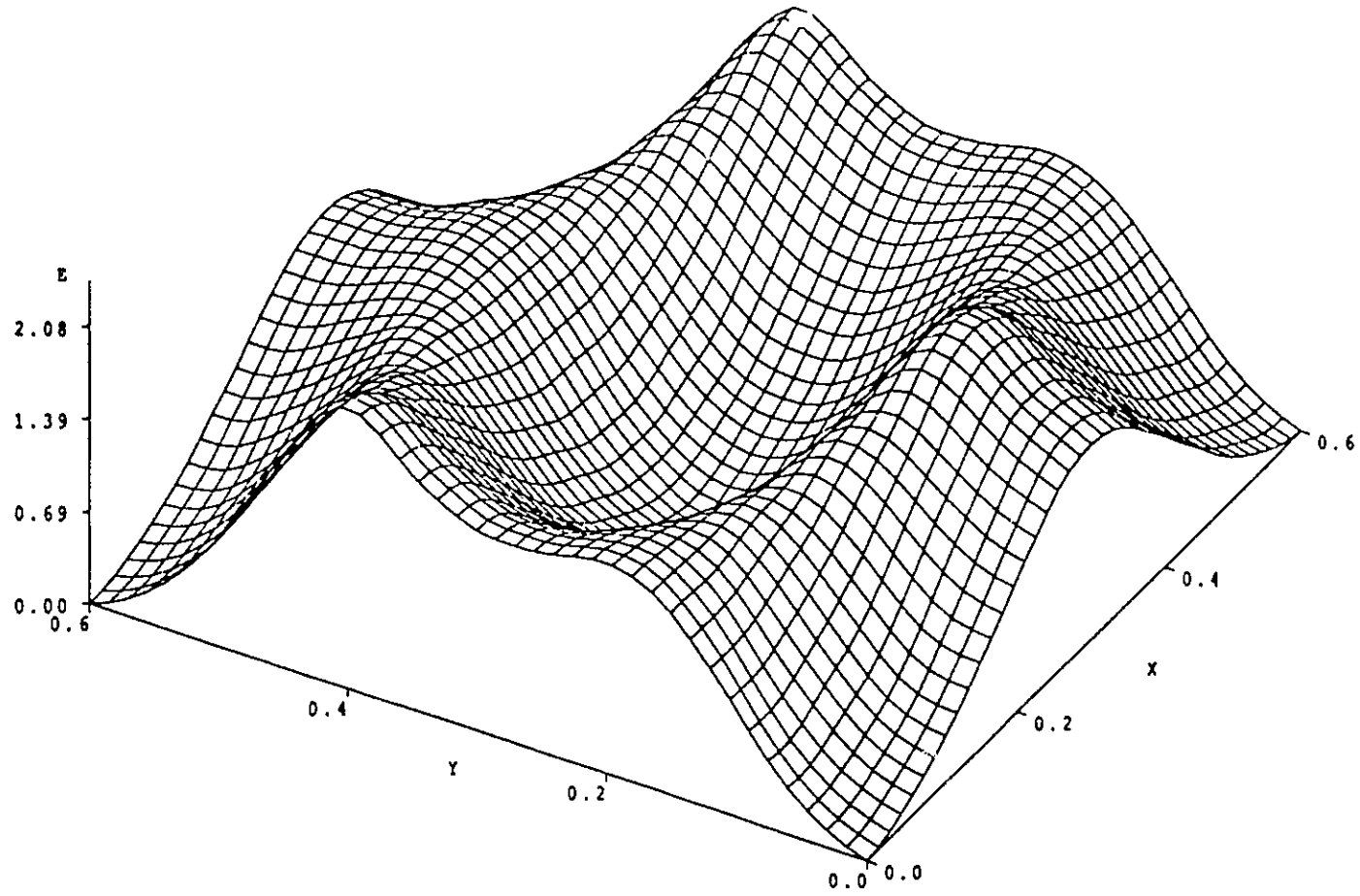

Fig. 29 {111} γ surfaces (a) for glide planes and (b) for shuffle planes. The energy unit is eV/(unit area in {111} plane) = 0.0783 eV/Å^2. x axis is from 0 to ½⟨110⟩ and y from 0 to ½⟨112⟩.

largest at the unstable stacking fault. Consequently my scaling procedure would tend to overestimate γ for small displacements. The important thing for my purpose is that the conclusions are unchanged whether unrelaxed or "relaxed" γ surfaces are used in the calculations, only the absolute values of the quantities are different as we have checked. Figure 30 gives the scaled gsf energies for the shuffle and glide planes along the directions of interest. The energy variations are seen to be mainly sinusoidal with comparable magnitudes for the segments relevant to the shuffle dislocations and glide partials [Fig. 30(b)], while the gsf energy variation relevant to the glide dislocations is an order of magnitude larger. The most important quantities are given in Table 4.1.

To solve the PN equation (4.5), the analytical expressions for the γ surfaces are needed. γ surface sections for the glide and shuffle are periodic with respect to the Burgers vector b (½⟨110⟩) (Fig. 30), it is natural for me to fit the graphs by Fourier series. This part of the work can be done by using any commercial fitting software. The fitting result for glide planes is

$$\gamma_g = 0.469543 - 0.565621\cos\frac{2\pi f}{b} + 0.109131\cos\frac{4\pi f}{b} - 0.015514\cos\frac{6\pi f}{b} - 0.000079\cos\frac{8\pi f}{b} - 0.000098\cos\frac{10\pi f}{b} - 0.000467\cos\frac{12\pi f}{b} \quad \ldots(4.13)$$

and for shuffle planes

$$\gamma_s = 0.049001 - 0.050395\cos\frac{2\pi f}{b} + 0.003815\cos\frac{4\pi f}{b} - 0.001516\cos\frac{6\pi f}{b} - 0.000024\cos\frac{8\pi f}{b} \quad \ldots(4.14)$$

TABLE 4.1. Key parameters characterizing dislocation properties. K measures the stiffness of the Si lattice for a given direction of distortion (see Eq. (4.7)]. γ_{max} is the maximum of the γ surface in the relevant interface along the direction of the Burgers vector $\langle 110 \rangle$ for the full dislocations and $\langle 112 \rangle$ for the partials. τ_{max} is the corresponding maximum restoring stress and 2ζ is the calculated dislocation width but obtained using the criterion given in the text (1 eV/Å^3 = 1.6 $\times 10^{12}$ dyn /cm^2).

dislocations		K (eV/Å^3)	γ_{max} (eV/Å^2)	τ_{max} (eV/Å^3)	b (Å)	2ζ (Å)
glide	60°	0.501	1.159	1.11	3.84	0.37
glide	screw	0.400	1.159	1.11	3.84	0.30
shuffle	60°	0.501	0.105	0.08	3.84	3.95
shuffle	screw	0.400	0.105	0.08	3.84	3.14
glide partials	30°	0.433	0.118	0.15	2.22	0.92
glide partials	90°	0.536	0.118	0.15	2.22	1.16

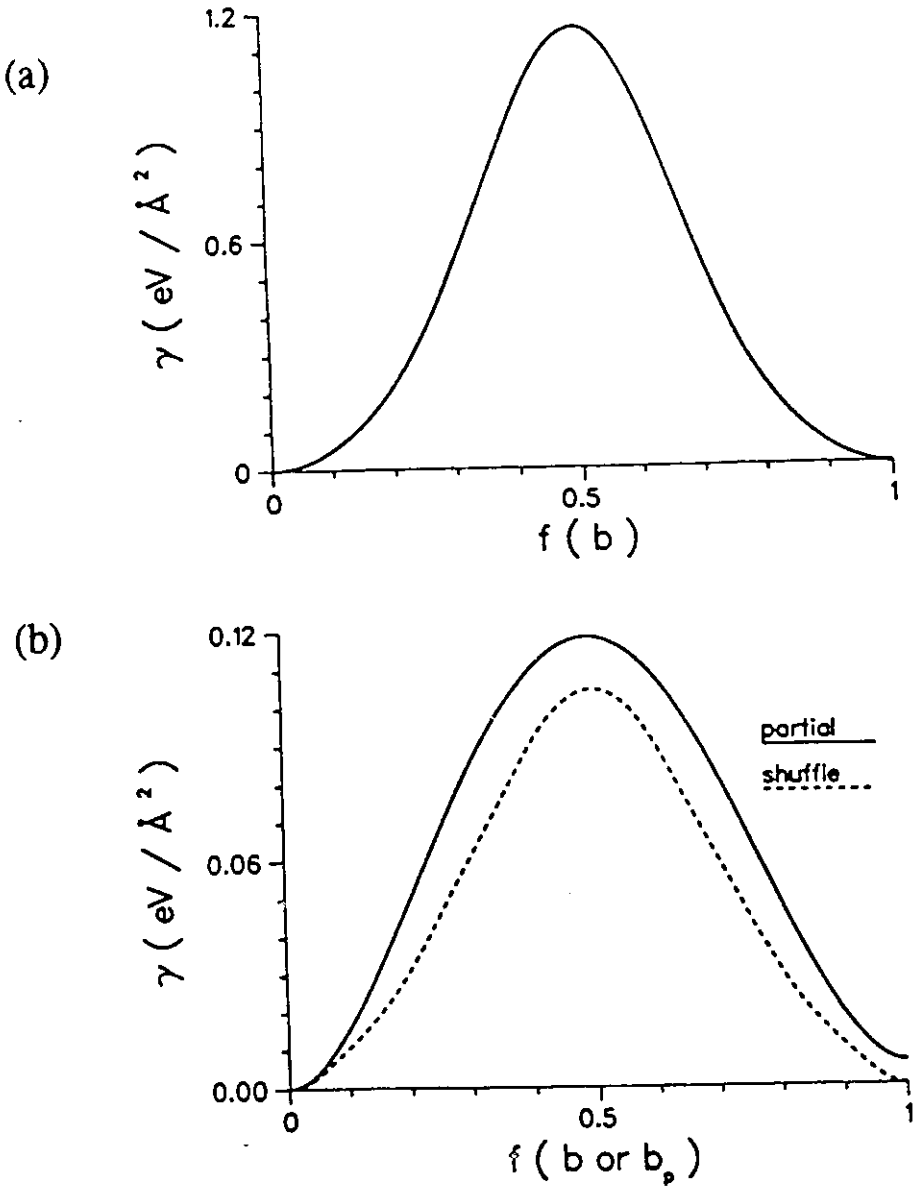

Fig. 30 γ surface sections (a) along a⟨110⟩ direction in the glide plane and (b) dashed line along the same direction in the shuffle plane. Both cover a total displacement of a full Burgers vector $b = 3.84$ Å. The full line in (b) along a⟨112⟩ direction of the glide plane is shown; at $b_p = 2.22$ Å, the Burgers vector for a glide partial, the stacking-fault energy is the energy of the intrinsic fault 0.006 ev/ Å^2.

However for the glide partial dislocation, I fitted it with a power series due to the stacking fault energy at f = b_p, where b_p (1/6(112)) is the Burgers vector for glide partial dislocations. And note that γ is minimum when f = 0 and b_p (see Fig. 29(a) and Fig. 30(b)). The final result is given below

$$\gamma_p = 1.857788\left(\frac{f}{b_p}\right)^2 - 3.212537\left(\frac{f}{b_p}\right)^3 - 0.319585\left(\frac{f}{b_p}\right)^4 + 3.408031\left(\frac{f}{b_p}\right)^5 - 2.253544\left(\frac{f}{b_p}\right)^6 + 0.525926\left(\frac{f}{b_p}\right)^7 \quad \ldots(4.15)$$

The restoring stresses $\tau_b^g(f)$,$\tau_b^s(f)$ and $\tau_b^p(f)$ are derived from γ surface γ_g, γ_s and γ_p respectively, with the help of the relation (4.12).

$$\tau_b^g(f) = -0.925594 \sin\frac{2\pi f}{b} + 0.357169 \sin\frac{4\pi f}{b} - 0.076162 \sin\frac{6\pi f}{b} - 0.000517 \sin\frac{8\pi f}{b} - 0.000802 \sin\frac{10\pi f}{b} - 0.004585 \sin\frac{12\pi f}{b} \quad \ldots(4.16)$$

$$\tau_b^s(f) = -0.082467 \sin\frac{2\pi f}{b} + 0.012486 \sin\frac{4\pi f}{b} - 0.007442 \sin\frac{6\pi f}{b} - 0.000157 \sin\frac{8\pi f}{b} \quad \ldots(4.17)$$

$$\tau_b^p(f) = 1.676108\left(\frac{f}{b_p}\right) - 4.347556\left(\frac{f}{b_p}\right)^2 - 0.576663\left(\frac{f}{b_p}\right)^3 + 7.686867\left(\frac{f}{b_p}\right)^4 - 6.099484\left(\frac{f}{b_p}\right)^5 + 1.660728\left(\frac{f}{b_p}\right)^6 \quad \ldots(4.18)$$

Where superscripts g,s and p represent glide, shuffle and glide partial dislocations and subscript b indicates that the restoring stresses are along the direction of Burgers vectors ⟨110⟩ for full dislocations and ⟨112⟩ for partials. The results of restoring stresses are shown in Fig. 31. The stresses show departure from sinusoidal behaviour, and their magnitudes are in direct correlation with the corresponding γ surface energy variations (see Fig. 30). Table 4.1 shows the input data for the six dislocations considered and their calculated width. Not surprisingly, since the width ζ is essentially inversely proportional to the maximum of the restoring stress τ_{max} the shuffle dislocations widths are an order of magnitude larger than the glide dislocation widths.

4.4 Solving the PN Equation

The solution to the PN equation, Eq. (4.5), requires knowledge of the K parameters and the restoring forces. The K parameters measure the elastic response of the lattice to displacements along the Burgers vector direction. Silicon is an anisotropic crystal, so procedures outlined by Hirth and Lothe [22] for such a situation had to be followed. For the Burgers vectors of interest, which all lie in the {111} plane, the K values obtained are given in Table 4.1. The K values can still be expressed in terms of effective elastic constants μ ' and ν' for the {111} plane using equation (4.7). In other words, within the {111} plane, silicon is essentially isotropic. The values derived within the {111} plane are $\mu' = 6.375\times10^{11}$ dyn/cm^2 and $\nu' = 0.2561$. This is to be compared with quoted averaged values for Si, $\mu = 6.81\times10^{11}$ dyn/cm^2 and $\nu = 0.218$ [22].

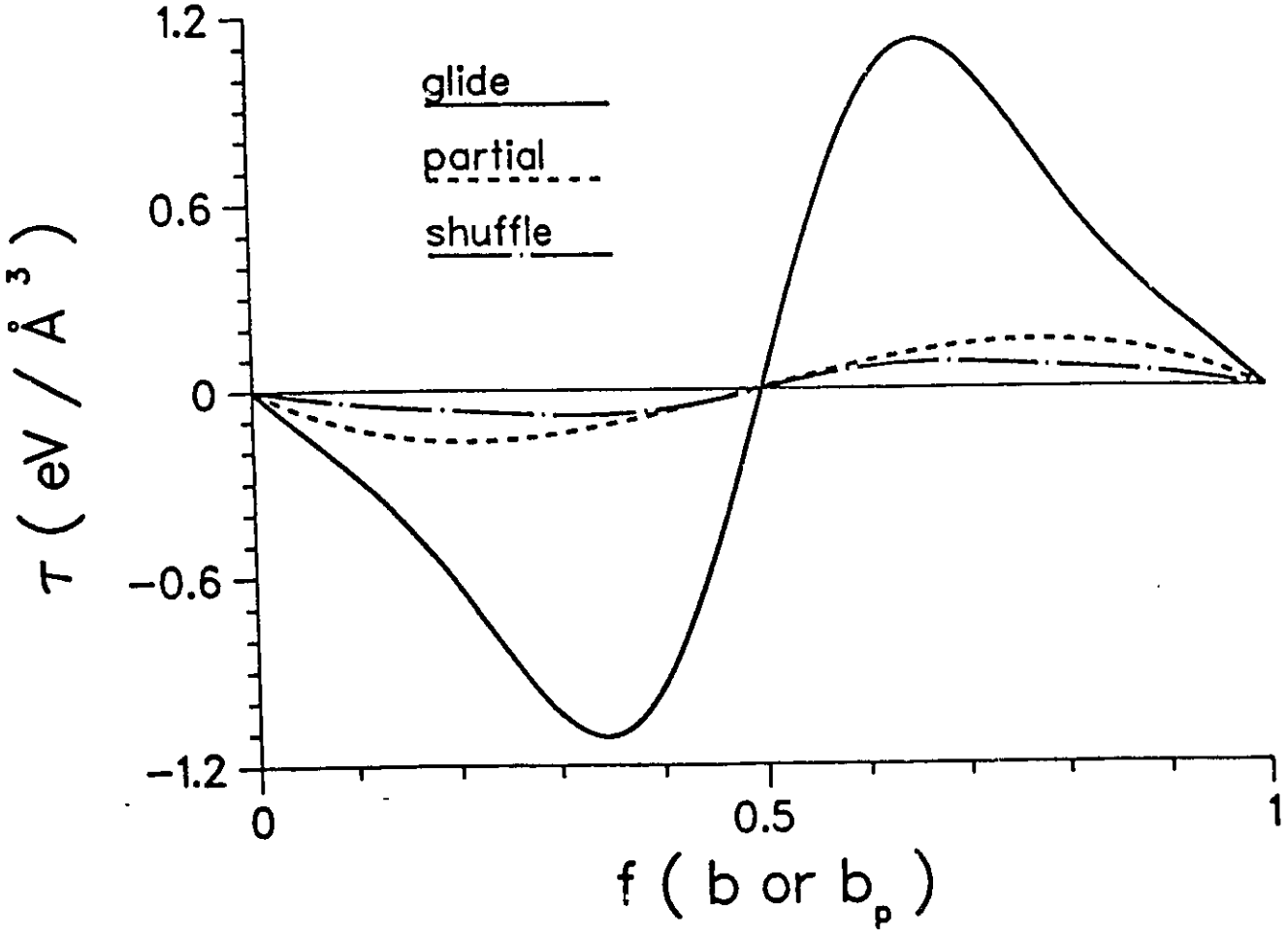

Fig. 31 Restoring forces τ corresponding to the γ surface section of Fig. 30.

A pair of functions, f(x) and $\tau_b(f)$, which is a solution of equation (4.5) can be obtained in the following way: if f(x) is chosen then the left side of equation (4.5) gives, after integration, a function of x, $T_b(x)$, which can be expressed as $T_b(x) = \tau_b(f(x))$. The disregistry was chosen in the form

$$f(x) = \sum_{i=1}^{N} f_i(x) = \frac{b}{\pi} \sum_{i=1}^{N} \alpha_i \arctan\frac{x-x_i}{c_i} + \frac{b}{2} \qquad \ldots(4.19)$$

where α_i, x_i, and c_i are variational constants and N is an integer [63,69]. The normalization condition given in equation (4.6) leads to the sum rule

$$\sum_{i=1}^{N} \alpha_i = 1 \qquad \ldots(4.20)$$

where every α_i is a positive number. The disregistry f(x) is chosen as a sum of elementary functions $f_i(x)$ introduced first by Foreman, Jaswon and Wood [75]. These elementary functions describe here the individual partials which are placed at x_i, with the Burgers vectors $b_i = \alpha_i b$ and dislocation widths characterized by parameters c_i. Substituting the trial function (4.19) into the left-hand side of the PN equation gives

$$T_b(x) = \frac{Kb}{2\pi} \sum_{i=1}^{N} \alpha_i \frac{x-x_i}{(x-x_i)^2+c_i^2} \qquad \ldots(4.21)$$

where the residue theorem is applied. The constants N, α_i, x_i and c_i can be obtained from the equation

$$T_b(x, N, \alpha_i, c_i, x_i) = \tau_b(f(x, N, \alpha_i, c_i, x_i)) \qquad \ldots(4.22)$$

where expressions for restoring stresses $\tau_b(f)$ are given by equations (4.16-4.18).

If the constants N, α_i, c_i,x_i can be found in such a way that Eq. (4.22) is fulfilled exactly for all x then f(x) given by Eq. (4.19) represents an exact solution of the PN equation corresponding to $\tau_b(f)$ given by Eq. (4.17-4.18). However, for our complicated restoring stresses, the equation (4.22) can only be solved approximately. The method of the least squares has been chosen for the numerical calculation of the constants. The expression

$$\Delta^2 = \int_{-\infty}^{\infty} [\ T_b(x, N, \alpha_i, c_i, x_i) - \tau_b(\ f(x, N, \alpha_i, c_i, x_i)\ ]^2\, dx \qquad \ldots(4.23)$$

has been minimized by an iteration method described underneath for fixed N and 3N constants α_i,c_i,x_i found from the condition $\Delta^2 \to 0$.

I showed above that to solve the PN integro-differential equation (4.5) is equivalent to finding minimum of a function of several independent variables.

A minimum point of a function can be either *global* (truly lowest function value) or *local* (the lowest in a finite neighbourhood and not on the boundary of that neighbourhood). Virtually nothing is known about finding global minimum in general. There are two standard heuristics that everyone uses: (i) find local minimum starting from widely varying starting values of the independent variables and then pick the least of these (if they are not all the same). (ii) perturb a local minimum by taking a finite amplitude step away from it, and then to see if your routine returns you to a better point, or "always" to the same one. This is so-called "annealing methods".

I first discuss the simplest method for one-dimensional minimization and then I turn to the multidimensional case. Since I cannot easily calculate the derivatives for my functions I

stayed away from the methods which use these information.

Golden Section Search in One Dimension

This method is to *bracket* a minimum without calculation of the derivative. A minimum is known to be bracketed only when there is a triplet of points, $a<b<c$, such that f(b) is less than both f(a) and f(c). In this case we know that the function (if it is nonsingular) has a minimum in the interval (a,c).

We then choose a new point x, either between a and b or between b and c. Suppose, to be specific, that we make the latter choice. Then we evaluate f(x). If $f(b)<f(x)$, then the new bracketing triplet is $a<b<x$; contrariwise, if $f(b)>f(x)$, then the new triplet is $b<x<c$. We continue the process of bracketing until the distance between the two outer points of the triplet is tolerably small.

Downhill Simplex Methods in Multidimensions

This method has a geometrical naturalness. A *simplex* is the geometrical figure consisting, in N dimensions of N+1 points and all their interconnecting line segments, polygonal faces, etc. In two dimensions, in which a function has only two independent variables, a simplex is triangular. In three dimensions it is a tetrahedron. In general, we are only interested in simplexes that are nondegenerate, i.e. which enclose a finite inner N-dimensional volume. Since this method needs N+1 points to start, if we think of one of these points as being our initial points $\mathbf{P}_o$,then we can take the other N points to be

$$\mathbf{P}_i = \mathbf{P}_o + \lambda \mathbf{e}_i \qquad \ldots(4.24)$$

where the $\mathbf{e}_i$'s are N unit vectors, and where λ is a constant which is our guess of the problem's characteristic length scale.

The downhill simplex method now takes a series of steps, most steps just moving the points of the simplex where the function is largest through the opposite face of the simplex to a lower point. These steps are called reflections, and they are constructed to conserve the volume of simplex (hence maintain nondegeneracy). When it can do so, the method expands the simplex in one or another direction to take larger steps. When it reaches a "valley floor", the method contracts itself in the transverse direction and tries to ooze down the valley. If there is a situation where the simplex is trying to "pass through the eye of a needle" it contracts itself in all directions, pulling itself around its lowest points.

The method requires only function evaluations, not derivatives. However, I find that it is not very efficient in terms of the number of function evaluations that it requires. And N+1 initial points are indeed a computational burden and the minimum somehow depends on those initial points.

Direction Set Methods in Multidimensions

We know how to minimize a function of one variable. If we start at a point **P** in N-dimensional space, and proceed from there in some vector direction **n** , then any function of N variables f(**P**) can be minimized along the line **n** by our one-dimensional methods. The detailed calculation can be taken as:

(i) Given an input **P** and **n**,and function f

(ii) Find the scalar λ that minimizes the f($\mathbf{P}+\lambda\mathbf{n}$)

(iii) Replace **P** by $\mathbf{P}+\lambda\mathbf{n}$, replace **n** by $\lambda\mathbf{n}$

(iv) Goto (i), repeat.

The most efficient way to decide the direction **n** along which the function minimizes is to use the gradients of the function. But this being to complicated to be considered, I use the following algorithm: take the vectors $\mathbf{e}_1,\mathbf{e}_2,\ldots,\mathbf{e}_N$ as a set of directions. Move along the first direction to its minimum, then *from there* along the second direction to its minimum, and so on, cycling through the whole set of directions as many times as necessary, until the function stops decreasing.

This simplest method may not work for other applications. But it works in my calculations and it is very efficient compared with the downhill simplex method.

4. 5 Dislocation Profiles

Some typical dislocation profiles are shown in Fig. 32. The positions x_i, Burgers vectors b_i (α_i) and characteristic widths c_i of each term in equation (4.19) are given in Table 4.2. N =3 was found to be sufficient to provide a good fit.

Corresponding dislocation densities appear in Fig. 33. This figure also shows the contribution of each term in Eq. (4.19) for three of the dislocations. As we can see from Table 4.2 and Fig. 33(b) and (c) , the splittings for the perfect dislocations are symmetrical, those for partials are asymmetrical. The shuffle dislocation profile is nearly that of a PN dislocation with sinusoidal restoring stress. The glide partials have slightly larger widths than the full glide dislocations. The departures from sinusoidal behaviour in the restoring stresses are reflected in the dislocation densities most visibly in the one for the 90° partial in Fig. 33(d).

Table 4.2 The solution to the PN equation for various dislocations in the form of Eq. (4.19). a is the lattice constant of silicon (a = 5.43 Å).

dislocations	α_1	x_1/a	c_1/a	α_2	x_2/a	c_2/a	α_3	x_3/a	c_3
glide 60°	0.576	0.0	0.017	0.212	0.0	0.144	0.212	0.0	0.144
glide screw	0.576	0.0	0.012	0.212	0.0	0.099	0.212	0.0	0.099
shuffle 60°	0.558	0.0	0.226	0.221	-0.501	0.645	0.221	0.501	0.645
shuffle screw	0.558	0.0	0.156	0.221	-0.345	0.444	0.221	0.345	0.444
partial 30°	0.692	0.0	0.134	0.137	-0.185	0.107	0.171	0.217	0.145
partial 90°	0.692	0.0	0.083	0.137	-0.115	0.066	0.171	0.134	0.090

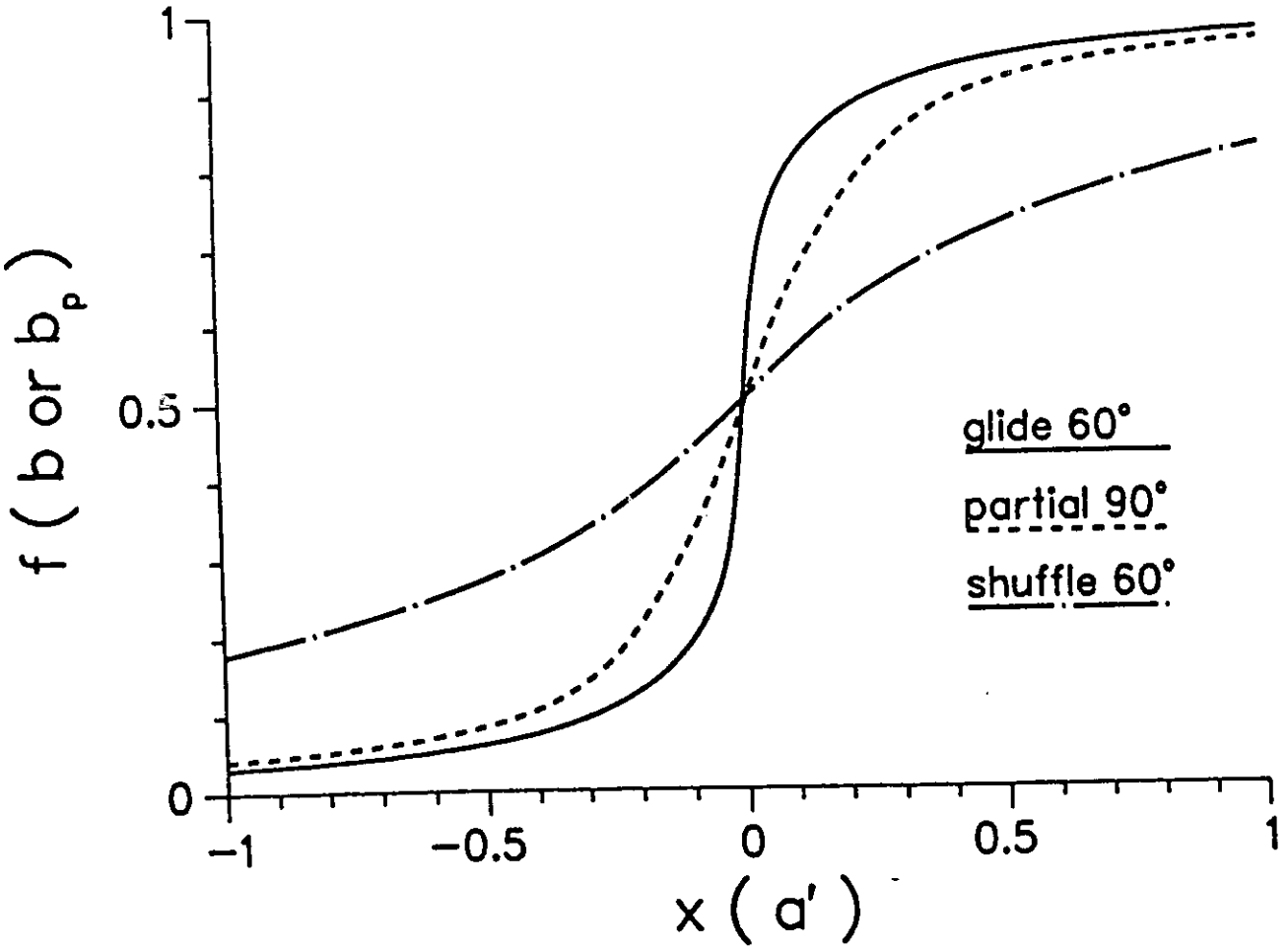

Fig. 32 Typical dislocation profiles. Displacements along the Burgers vectors plotted as a function of the distance from the dislocation line.

(a)

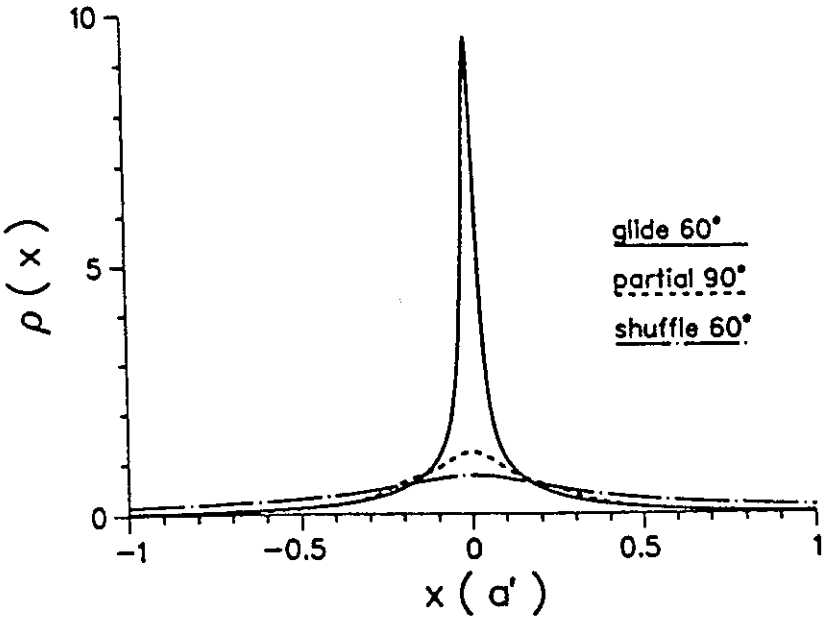
10
5
0
ρ (x)
−1
−0.5
0
0.5
1
x (a')
glide 60°
partial 90°
shuffle 60°

(b)

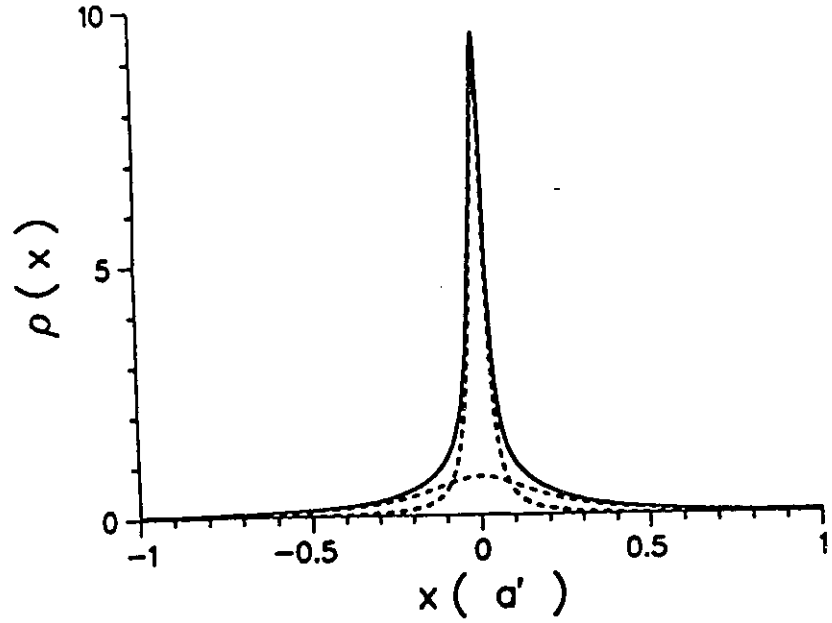
10
5
0
ρ (x)
−1
−0.5
0
0.5
1
x (a')

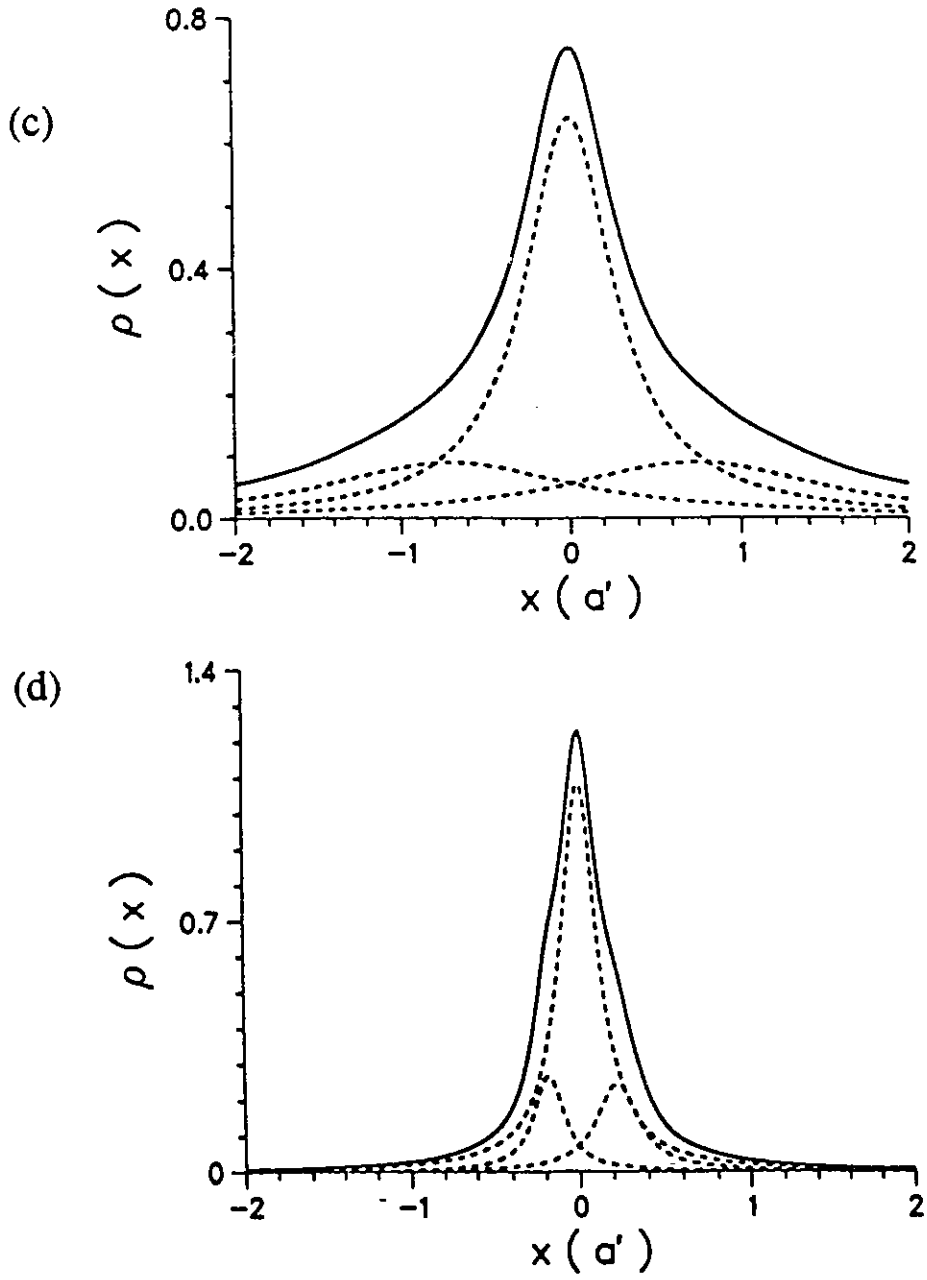

Fig. 33 Some dislocation densities $\rho(x)=df(x)/dx$; (a) compares the distributions for three dislocations; (b),(c) and (d) show the contributions from the three terms in Eq. (4.19) (dashed lines) for the 60° glide, 60° shuffle and 90° partial, respectively. (full lines are the sum of the dashed lines).

4.6 Misfit Energies, Peierls-Nabarro Energies and Stresses

Although a periodic restoring force has been incorporated into the PN model, it still considers the crystal above and below the glide plane as an elastic continuum medium. As in the Frank and van der Merwe model [73] the dislocation is free to glide in the crystal. If f(x) is a solution to the displacement field, so is f(x-u), where u is any constant [f(x-u) corresponds to a dislocation translated by u]. This "continuum-mass" dislocation has no PN stress. However, a stress can be defined by noting that the displacement function f(x-u) corresponds to a real displacement only where an atomic plane is present. In the absence of a dislocation the spacing of atomic planes in the direction x is a'. With the x axis along a⟨112⟩ direction a' = $(\sqrt{6})a/4$ = 3.33 Å, where a is the Si lattice constant 5.43 Å. When the dislocation is introduced, the planes, in the upper half of the crystal at a position ma' in a direction perpendicular to the dislocation line, will be displaced with respect to the lower half by f(ma'-u). The misfit energy can be considered as the sum of misfit energies between pairs of atomic planes and can be written

$$W(u) = \sum_{m=-\infty}^{+\infty} \gamma(f(ma'-u)) a' \qquad ...(4.25)$$

This formula focuses on the variation of the disregistry as one moves across the dislocation core along the interface in a direction perpendicular to the dislocation line. It has the correct period a' (see Fig. 34), and the right limit for very narrow dislocations for which the amplitude of variation of W(u), W_p , the PN energy, is the energy barrier for motion of the dislocation. (Our

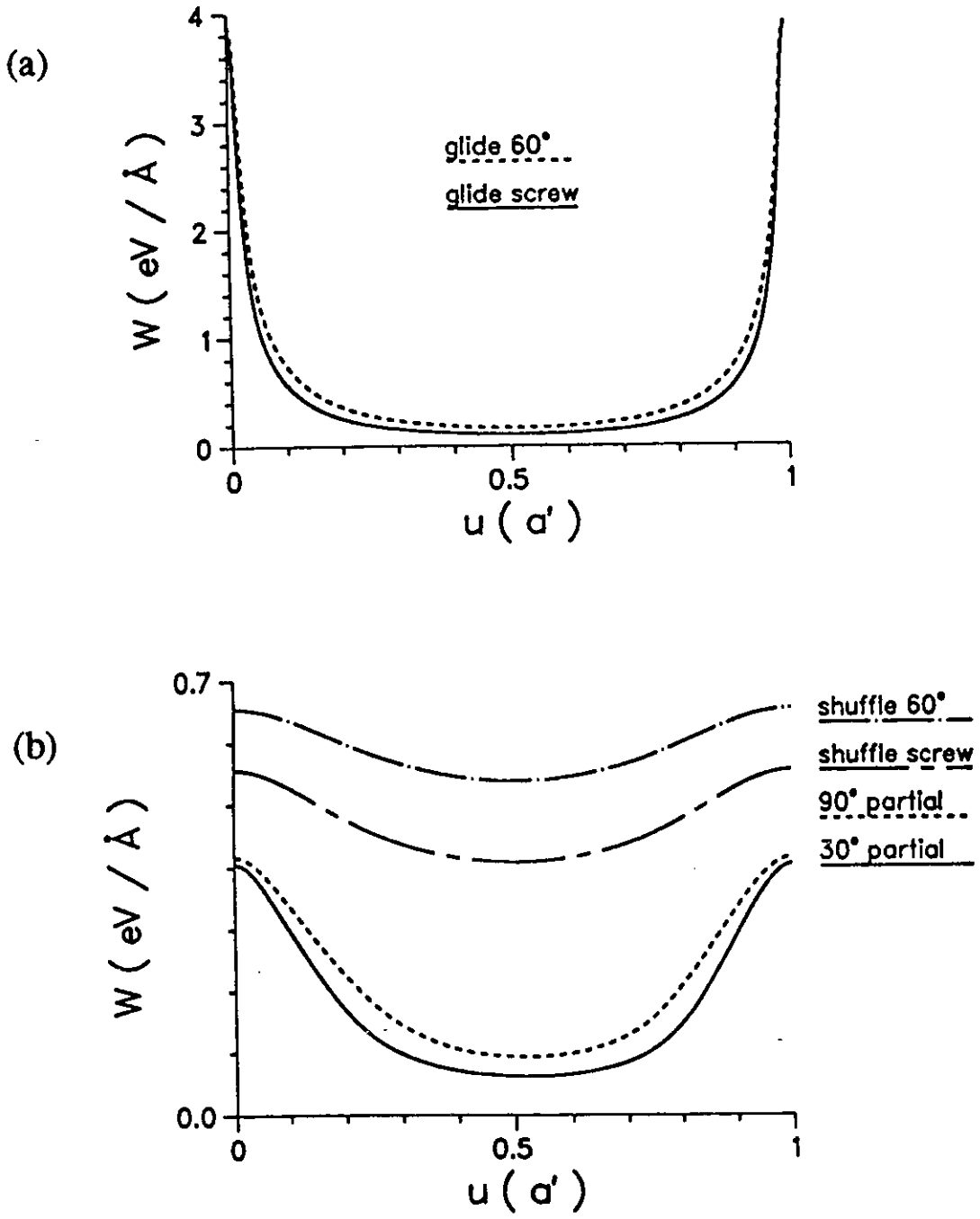

Fig. 34 Misfit energies W(u) for (a) full dislocations in the glide plane and (b) full dislocations in the shuffle plane and partials in the glide plane.

formula is the same as the one suggested by Christian and Vitek [76] but is different from the one discussed in Ref. [22] and originally due to Peierls [18] and Nabarro [19]. That formula is based on a slightly different atomistic basis of the continuum model leading to sums for the upper and lower half planes with coordinates differing by a'/2. The disadvantage of that formula is that both u=0; and a'/2 correspond to maximum energy configurations and the minimum energy configuration is an asymmetric configuration with u=a'/4, resulting in a period for W(u) of a'/2 instead of a'.) A physically related quantity is the Peierls stress σ_p, the maximum stress required to overcome the barrier. Two energy barriers may be comparable, but if the distances are quite different over which this energy rise has to be realized, the corresponding Peierls stresses can be quite different. A longer repeat distance will usually necessitate a smaller Peierls stress. Our formula has the correct period for W(u) and hence is expected to give a reasonable value for σ_p. σ_p is defined as the maximum in the variation of the interface stress, σ, the scaled slope of W(u) for a given position of the dislocation:

$$\sigma_p = \max[\sigma] = \max[\frac{1}{a'}\frac{dW}{du}] \qquad \ldots(4.26)$$

σ_p is obtained from Fig. 35.

An estimate for very narrow dislocations, where the core is less than one lattice site wide can be easily derived using the continuum dislocation profile given in Eq. (4.11) with an adjustable width ζ. Since only one term in the sum in Eq. (4.25) will contribute significantly:

$$\sigma_p = \max[\frac{d\gamma(f(-u))}{du}]$$

$$= \max[-\frac{d\gamma}{df}\frac{df}{du}] \simeq \tau_{max}\frac{b}{\pi\zeta} \simeq 4\frac{\tau_{max}^2}{K} \qquad \ldots(4.27)$$

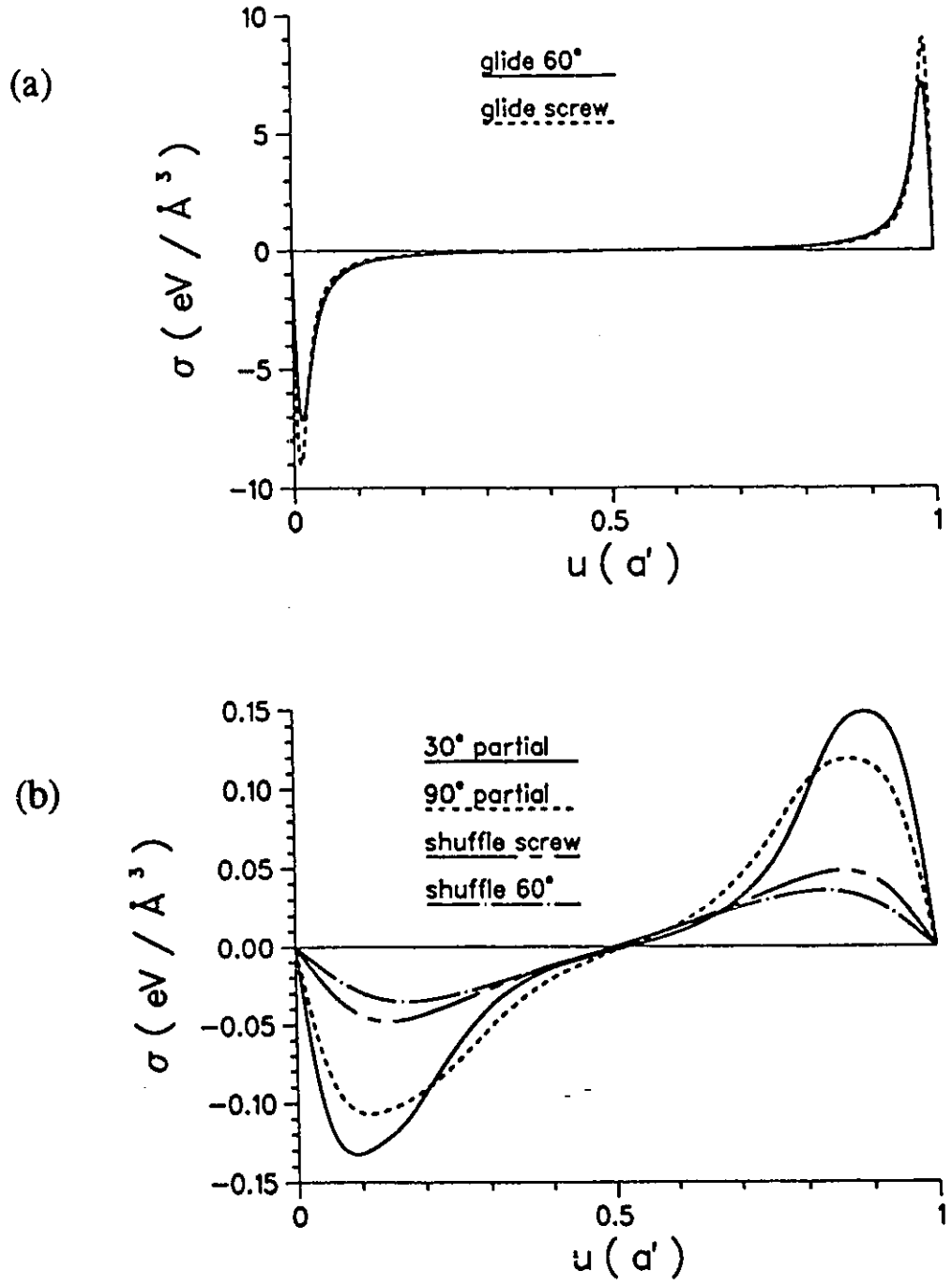

Fig. 35 Interface stresses σ corresponding to variation of the misfit W(u) energy with position u. The maximum corresponds to the Peierls stress σ_p. As in Fig. 34, (a) for full dislocations in the glide plane and (b) for full dislocations in shuffle plane and partials dislocations in the glide plane.

Whereas the PN energy depends in this limit only on the potential barrier to be overcome in the γ surface, the Peierls stress is very sensitive to the width of the dislocation or the relative strength of the lattice with respect to the energy barrier.

Typical variations of W(u) are shown in Fig. 34. The minimum W(a'/2) can be viewed as the misfit energy. It is the total energy stored across the glide surface. It is the nonelastic part of the dislocation energy and provides an estimate for the core energy of the dislocation, which takes into account the discreteness of the lattice. It is different from the obvious definition of this quantity in the PN model, which is the integral of the disregistry energy over the whole interface:

$$W_m = \int_{-\infty}^{+\infty} \gamma(f(x)) \, dx \qquad \ldots(4.28)$$

This last quantity can be shown to be independent of the restoring force. Integration by parts and use of the PN equation gives

$$W_m = -\int_{-\infty}^{+\infty} x \frac{\partial \gamma}{\partial x} dx$$

$$= -\int_{-\infty}^{+\infty} x \frac{\partial \gamma(f(x))}{\partial f} \frac{\partial f}{\partial x} dx \qquad \ldots(4.29)$$

$$= \frac{K}{2\pi} \int\int \frac{x}{x-x'} \frac{\partial f}{\partial x'} \frac{\partial f}{\partial x} \, dx \, dx'$$

Separating this last integral into two equal parts with an interchange in the roles of x and x' yields

$$W_m = \frac{K}{4\pi} \int\int \frac{\partial f}{\partial x} \frac{\partial f}{\partial x'} \, dx \, dx' = \frac{Kb^2}{4\pi} \qquad \ldots(4.30)$$

W_m depends only on the elastic properties of the material and the Burgers vector. The integral reflects the fact earlier noted that the material on each side of the glide plane is taken as a continuum. The restoring forces determine the spreading of this energy over a larger or smaller area but, since the medium is elastic, the total remains unchanged. W_m, therefore, does not distinguish between glide or shuffle plane dislocations. It is interesting to note that W_m is the average of the function W(u), since

$$\frac{1}{a'}\int_0^{a'} W(u)\,du = \int_0^{a'} \sum_{m=-\infty}^{+\infty} \gamma\left(f(ma'-u)\right) du - \int_{-\infty}^{+\infty} \gamma\left(f(u)\right) du = W_m \qquad \ldots(4.31)$$

W_m is, hence, an average misfit energy for all positions of the dislocations as it is displaced through the lattice. As mentioned earlier W(a'/2), an estimate of the core energy, is the minimum and W_p, the PN energy, the amplitude of the variation of W(u).

The results for all these quantities are shown in Table 4.3 for the Si dislocations. As this table shows for a particular dislocation, glide and shuffle sets have the same average misfit energy because that energy depends only on the elastic response of the lattice. For the narrow glide set, this energy has a larger amplitude than for the wide shuffle set. Consequently glide dislocations have larger PN energies and Peierls stresses than the shuffle dislocations. Another consequence is that, since more atomic planes are deformed in the shuffle dislocations, its total minimum misfit or core energy is larger than that of the glide dislocations, where only a couple of planes are affected. These results follow from the relationship developed above between W_p and the core energy W (a'/2).

TABLE 4.3. Properties of dislocations in Si obtained from the Peierls-Nabarro model (μ = 0.426 eV / Å^3)

dislocations	W_m (eV/ Å)	W(a'/2) (eV/ Å)	W_p (eV / Å)	σ_p (μ)
glide 60°	0.588	0.169	3.77	16.92
glide screw	0.468	0.110	3.74	21.29
shuffle 60°	0.588	0.538	0.116	0.083
shuffle screw	0.468	0.408	0.148	0.112
glide partial 30°	0.169	0.062	0.343	0.351
glide partial 90°	0.210	0.093	0.323	0.282

Chapter 5. Test of the Peierls-Nabarro Model with a Stillinger-Weber Potential Model of Silicon

5.1 Introduction

The last chapter presented studies on a zero temperature model for dislocations in silicon constructed within the frame work of the Peierls-Nabarro (PN) model [also see Ref. 79] using generalized stacking fault energies obtained from first principle density functional calculations. Peierls stresses for various possible perfect and imperfect dislocations were obtained. The question is how reliable is this model. In this chapter, I calculate the Peierls stresses for the different dislocations using an atomistic relaxation technique on an empirical potential model of Si. The simulations are extended to the dislocation profiles. I also investigate the dissociation and motion of glide and shuffle dislocations. These results will be compared with those obtained from the PN model.

5.2 Model and Simulation Procedure

5.2.1 Stillinger-Weber potential

To assess the validity of the PN model, we wanted to test it within an atomistic model. The Stillinger-Weber potential (SW) [58] was chosen for several reasons, it is the most widely

used empirical potential for silicon and it produces an overal similar generalized stacking fault (**GSF**) energy surfaces as those obtained from first principal density functional theory calculations (in the local density approximation, **LDA**) [53]. Cross-sections of the GSF energy surface for the glide plane (without atomistic relaxation perpendicular to the glide plane) are shown in Fig. 36a and b for $<110>$ and $<112>$ directions, which are the principal interest. In each case, except for LDA, results of other empirical potentials such as SW potential, Kaxiras-Pandey potential (**KP**) and Tersoff potential(**T**) [58] are also displayed. As we can see from Fig. 36 the SW potential is in reasonable agreement with the LDA curve especially in the $<110>$ direction.

SW potential has proven to be valid in many studies, such as the phase diagram of silicon [80], the critical layer thickness [81], the silicon surface [82] and silicon indentation [83]. Some questions have been raised about its validity in reconstructions in Si in details [84]. The emphasis at this point is using an atomistic model which is compatible to the PN model. The SW potential contains both two-body and three-body interactions

$$\Phi(1,\ldots,N) = \sum_{\substack{i,k \\ i<j}} v_2(i,j) + \sum_{\substack{i,j,k \\ i<j<k}} v_3(i,j,k) \qquad \ldots(5.1)$$

where pair and triple potential v_2, v_3 are as follows

$$\begin{aligned} v_2(r_{ij}) &= \varepsilon f_2\left(\frac{r_{ij}}{\sigma}\right), \\ v_3(\boldsymbol{r}_i,\boldsymbol{r}_j,\boldsymbol{r}_k) &= \varepsilon f_3\left(\frac{\boldsymbol{r}_i}{\sigma},\frac{\boldsymbol{r}_j}{\sigma},\frac{\boldsymbol{r}_k}{\sigma}\right) \end{aligned} \qquad \ldots(5.2)$$

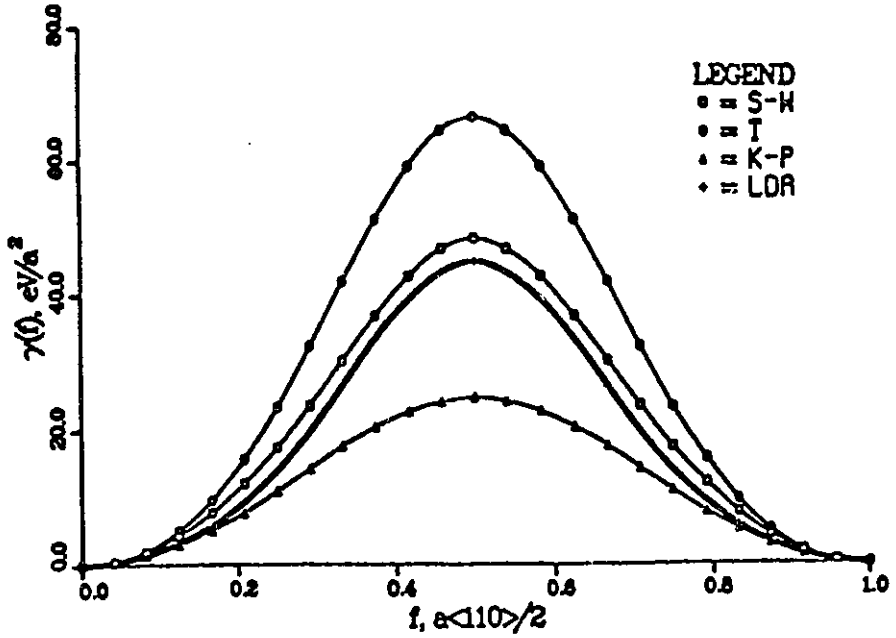

(a)

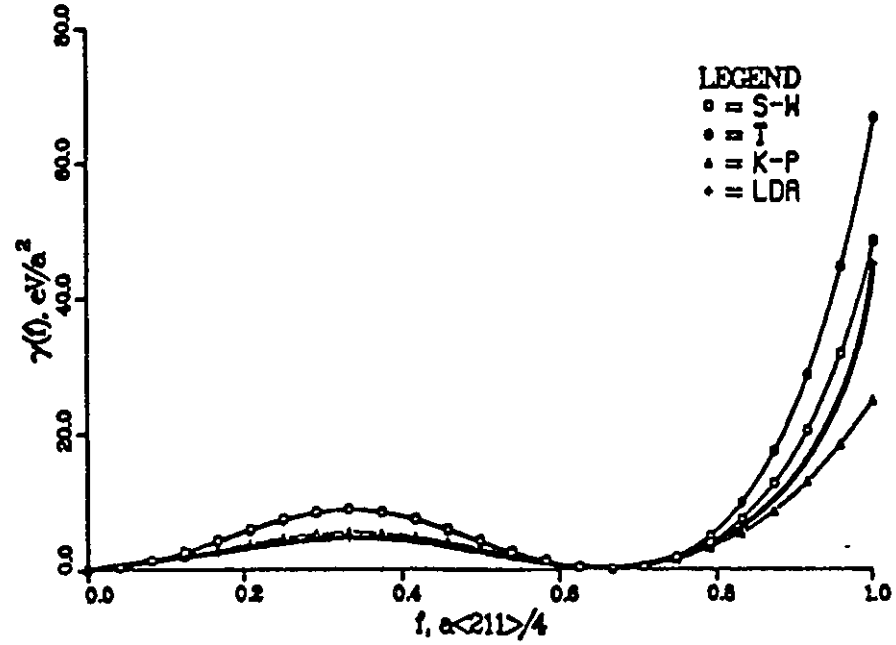

(b)

Fig. 36 Cross-sections of the GSF energy surface in the glide plane with Stillinger-Weber potential (S-W), Tersoff potential (T), local density approximation (LDA) and Kaxiras-Pandey potential (K-P) for (a) <110> and (b) <211> directions (no atomic relaxation perpendicular to the glide plane). a is the lattice constant of Si.

where ϵ is chosen to give f_2 depth -1, and σ is chosen to make $f_2(2^{1/6})$ vanish.

$$\begin{aligned} \varepsilon &= 50\,kcal/mol = 3.4723\times10^{-13}\ erg/at.pair \\ \sigma &= 2.0951\text{Å} \end{aligned} \qquad \ldots(5.3)$$

f_2 is a function only of scalar distance, and f_3 possesses translational and rotational terms. In simulations, ϵ and σ are used as energy and length unit. The reduced pair potential can then be written as

$$f_2(r) = \begin{cases} A(Br^{-p}-r^{-q})\exp[(r-b)^{-1}], & r<b \\ 0, & r\geq b \end{cases} \qquad \ldots(5.4)$$

where A,B,p,q and b are positive parameters. The cutoff distance is at b.

$$\begin{aligned} &A = 7.049556277,\ B = 0.6022245584, \\ &p = 4,\ q = 0,\ b = 1.80 \end{aligned} \qquad \ldots(5.5)$$

The same cutoff distance is extended to the three-body interactions

$$f_3(\boldsymbol{r}_i,\boldsymbol{r}_j,\boldsymbol{r}_k) = \begin{cases} h(r_{ij},r_{ik},\theta_{jik})+h(r_{ji},r_{jk},\theta_{ijk})+h(r_{ki},r_{kj},\theta_{ikj}), & r<b \\ 0, & r\geq b \end{cases} \qquad \ldots(5.6)$$

where θ_{jik} is the angle between $\mathbf{r}_j$ and $\mathbf{r}_k$ subtended at vertex i, etc. The function h belongs to a two-parameter family. Provided that both r_{ij} and r_{ik} are less than previously introduced cutoff b, it has the following form:

$$h(r_{ij},r_{ik},\theta_{jik}) = \lambda\exp[\gamma(r_{ij}-b)^{-1}+\gamma(r_{ik}-b)^{-1}]\times(\cos\theta_{jik}+\frac{1}{3})^2 \qquad \ldots(5.7)$$

with

$$\lambda = 21.0, \quad \gamma = 1.20 \qquad \ldots(5.8)$$

otherwise h vanishes identically. The "ideal" tetrahedral angle θ_t is such that

$$\cos\theta_t = -\frac{1}{3} \qquad \ldots(5.9)$$

so that the trigonometric part of expression (5.7) clearly discriminates in favour of pairs of bonds emanating from vertex i with the desired geometry.

5.2.2 Three-body Forces

The pair interactions for the SW potential can be calculated by using the derivative of expression (5.4) with respect to r. However evaluation of three-body forces are much more complicated. Let us define F3[i] as the three-body force acting on atom i due to the contributions of j, k atoms. These contributions are evaluated by simple differentiations of three h functions (5.7) of equation (5.6):

$$\nabla_{r_i} h(r_{ij}, r_{ik}, \theta_{jik}) = -\lambda \exp(ijk) \left[\frac{\gamma \nabla_{r_i} r_{ij}}{(r_{ij}-b)^2} + \frac{\gamma \nabla_{r_i} r_{ik}}{(r_{ik}-b)^2}\right] (\cos\theta_{jik} + \frac{1}{3})^2$$
$$+2\lambda \exp(ijk) (\cos\theta_{jik} + \frac{1}{3}) \nabla_{r_i} \cos\theta_{jik} \qquad \ldots(5.10)$$

$$\nabla_{r_i} h(r_{ji}, r_{jk}, \theta_{ijk}) = -\lambda \exp(jik) \left[\frac{\gamma \nabla_{r_i} r_{ji}}{(r_{ji}-b)^2} + \frac{\gamma \nabla_{r_i} r_{jk}}{(r_{jk}-b)^2}\right] (\cos\theta_{ijk} + \frac{1}{3})^2$$
$$+2\lambda \exp(jik) (\cos\theta_{ijk} + \frac{1}{3}) \nabla_{r_i} \cos\theta_{ijk} \qquad \ldots(5.11)$$

$$\nabla_{r_i} h(r_{ki}, r_{kj}, \theta_{ikj}) = -\lambda \exp(kij) \left[\frac{\gamma \nabla_{r_i} r_{ki}}{(r_{ki}-b)^2} + \frac{\gamma \nabla_{r_i} r_{kj}}{(r_{kj}-b)^2}\right] (\cos\theta_{ikj} + \frac{1}{3})^2$$

$$+2\lambda \exp(kij) (\cos\theta_{ikj} + \frac{1}{3}) \nabla_{r_i} \cos\theta_{ikj} \qquad \ldots(5.12)$$

where exp(ijk) is the abbreviation of the following terms

$$\exp(ijk) = \exp[\gamma (r_{ij}-b)^{-1} + \gamma (r_{ik}-b)^{-1}]$$

The evaluation of the gradients of the cosine functions and the pair separations may be readily calculated with the help of the equation (3.13) and (3.15). Substituting these equations along with equation (5.10-12) into the left-hand side of the expression (5.6), we get the three-body force F3[i]

$$F3[i] = -\nabla_{r_i} f_3(\boldsymbol{r}_i, \boldsymbol{r}_j, \boldsymbol{r}_k) \qquad \ldots(5.13)$$

$$= \lambda \exp(ijk) \left[\frac{\gamma \boldsymbol{r}_{ij}}{r_{ij}(r_{ij}-b)^2} + \frac{\gamma \boldsymbol{r}_{ik}}{r_{ik}(r_{ik}-b)^2}\right] (\cos\theta_{jik} + \frac{1}{3})^2$$

$$-2\lambda \exp(ijk) (\cos\theta_{jik} + \frac{1}{3}) \left[\frac{\boldsymbol{r}_{ij}+\boldsymbol{r}_{ik}}{r_{ij}r_{ik}} + \cos\theta_{jik} \left(\frac{-\boldsymbol{r}_{ij}}{r_{ij}^2} + \frac{-\boldsymbol{r}_{ik}}{r_{ik}^2}\right)\right]$$

$$+\lambda \exp(jik) \left[\frac{-\gamma \boldsymbol{r}_{ji}}{r_{ji}(r_{ji}-b)^2}\right] (\cos\theta_{ijk} + \frac{1}{3})^2$$

$$-2\lambda \exp(jik) (\cos\theta_{ijk} + \frac{1}{3}) \left[\frac{-\boldsymbol{r}_{jk}}{r_{ji}r_{jk}} + \cos\theta_{ijk} \frac{\boldsymbol{r}_{ji}}{r_{ji}^2}\right]$$

$$+\lambda \exp(kij) \left[\frac{-\gamma \boldsymbol{r}_{ki}}{r_{ki}(r_{ki}-b)^2}\right] (\cos\theta_{ikj} + \frac{1}{3})^2$$

$$-2\lambda \exp(kij) (\cos\theta_{ikj} + \frac{1}{3}) \left[\frac{-\boldsymbol{r}_{kj}}{r_{ki}r_{kj}} + \cos\theta_{ikj} \frac{\boldsymbol{r}_{ki}}{r_{ki}^2}\right]$$

Note that ϵ and σ are units of energy and length respectively. And the gradient of pair separation r_{jk} or r_{kj} with respect to $\mathbf{r}_i$ vanishes here.

I calculated the F3[i] as follows. The j and k atoms are chosen from the neighbour list of atom i. The minimum image pair separations r_{ij}, r_{ik} and r_{jk} (see section 3.3 for detail) and cosine functions can be readily evaluated during a simulation. These results are substituted into equation (5.13) to get the three-body force F3[i]. Repeat above procedure for every atom i. A typical piece of C code is

```
For(i=0; i<total_atom_number; i++)
 {
  For(J=0; J< i_neighbour_list -1; J++)
   {
    For(K=J+1; K< i_neighbour_list; K++)
     {
          ......
                    sort the index of j and k atom;
                    calculate pair separations;
                    apply periodic condition;
                    minimum pair separations and cosine functions
                    F3[i] += left side of equation (5.13);
          ......
     }
   }
 }
```

As we can see from equation (5.13), since there are so many terms involved in F3[i], it is very easy to make a mistake and it is hard to debug later when coding the program. Another approach is taken due to the fact that the three h functions in equation (5.6) are symmetric with respect to i, j and k. Instead of evaluating the three-body interaction force F3[i] for only atom i inside the triple loops, three forces f3[i], f3[j], f3[k] are calculated for each atom i,j,k, but through gradients from *only one* h function with respect to $\mathbf{r}_i$, $\mathbf{r}_j$ and $\mathbf{r}_k$ respectively

$$f3[i] = -\nabla_{r_i} h(r_{ij}, r_{ik}, \theta_{jik})$$

$$= \lambda \exp(ijk) \left[\frac{\gamma r_{ij}}{r_{ij}(r_{ij}-b)^2} + \frac{\gamma r_{ik}}{r_{ik}(r_{ik}-b)^2}\right] (\cos\theta_{jik} + \frac{1}{3})^2 \qquad (5.14)$$

$$-2\lambda \exp(ijk) (\cos\theta_{jik} + \frac{1}{3}) \left[\frac{r_{ij}+r_{ik}}{r_{ij}r_{ik}} + \cos\theta_{jik} (\frac{-r_{ij}}{r_{ij}^2} + \frac{-r_{ik}}{r_{ik}^2})\right]$$

$$f3[j] = -\nabla_{r_j} h(r_{ij}, r_{ik}, \theta_{jik})$$

$$= \lambda \exp(ijk) \left[\frac{-\gamma r_{ij}}{r_{ij}(r_{ij}-b)^2}\right] (\cos\theta_{jik} + \frac{1}{3})^2 \qquad \ldots (5.15)$$

$$-2\lambda \exp(ijk) (\cos\theta_{jik} + \frac{1}{3}) \left[\frac{-r_{ik}}{r_{ij}r_{ik}} + \cos\theta_{jik} (\frac{r_{ij}}{r_{ij}^2})\right]$$

$$f3[k] = -\nabla_{r_k} h(r_{ij}, r_{ik}, \theta_{jik})$$

$$= \lambda \exp(ijk) \left[\frac{-\gamma r_{ik}}{r_{ij}(r_{ij}-b)^2}\right] (\cos\theta_{jik} + \frac{1}{3})^2 \qquad \ldots (5.16)$$

$$-2\lambda \exp(ijk) (\cos\theta_{jik} + \frac{1}{3}) \left[\frac{-r_{ij}}{r_{ij}r_{ik}} + \cos\theta_{jik} (\frac{r_{ik}}{r_{ik}^2})\right]$$

The C code for this algorithm is

```
For(i=0; i<total_atom_number; i++)
 {
  For(J=0; J< i_neighbour_list -1; J++)
   {
    For(K=J+1; K< i_neighbour_list; K++)
     {
          ......
                    sort the index of j and k atom;
                    calculate pair separations;
                    apply periodic condition;
                    minimum pair separations and cosine functions
                    f3[i] += left side of equation (5.14);
                    f3[j] += left side of equation (5.15);
                    f3[k] += left side of equation (5.16);
          ......
     }
   }
 }
```

After simulation, the second algorithm will give the same three-body forces f3[i] for each atom

i as that of the first algorithm F3[i]. In the second method, even though when i = i (first loop) f3[i] only counts the contribution of one h function from equation (5.6), the other two contributions of the remains of h functions will be added when i = j (when i and k are the neighbour atoms of atom j) and when i = k (when i, j are the neighbour of atom k). In this case, as long as the two algorithms produce the same results, I am quite confident that the code for the calculation the three-body forces is correct.

5.2.3 Static Relaxation

The relaxation technique used in the present calculations was the same as in chapter 3 (for details see Ref. [85]). The crystallites were rectangular parallepipeds with a certain number of repeat units surrounded by (-1 -1 2), (1 1 1) and (-1 1 0) planes (see Fig. 37(a)). The dislocation line was always aligned along the z [-1 1 0] axis with periodic boundary conditions along this axis so that effectively an infinite dislocation was studied. Atoms were displaced from their equilibrium (perfect lattice) positions as given by elasticity theory for the given Burgers vector (partial or perfect dislocations) and the position of the slip plane (for the glide plane see Fig. 37(b) and the shuffle plane see Fig. 37(c)). The boundaries of the x and y directions were fixed while the rest of the atoms were relaxed by minimizing the atomistic potential energy. By fixing the boundary along the x and y directions no major reconstruction, such as a Peierls type reconstruction, is allowed. Although reconstruction is known to occur in Si, imposing these conditions allows a more direct comparison with the results of the PN model.

Studies of the Peierls stresses for various dislocations were performed using a procedure outlined by Vitek etc. [86,87]. The stress was imposed by introducing a homogeneous shear

(a)

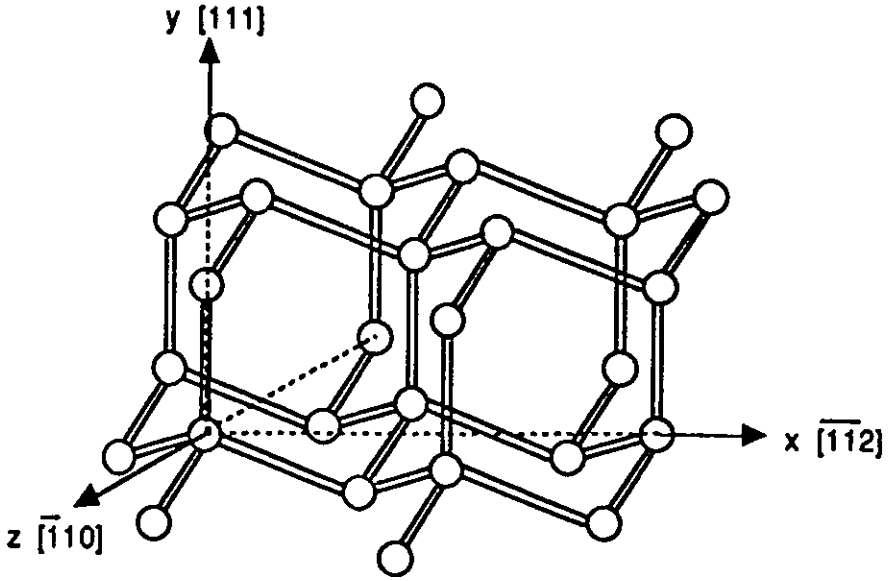

(b)

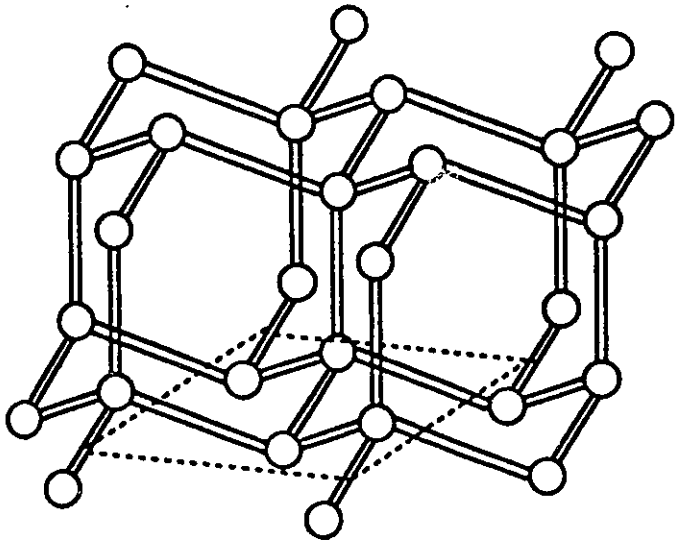

(c)

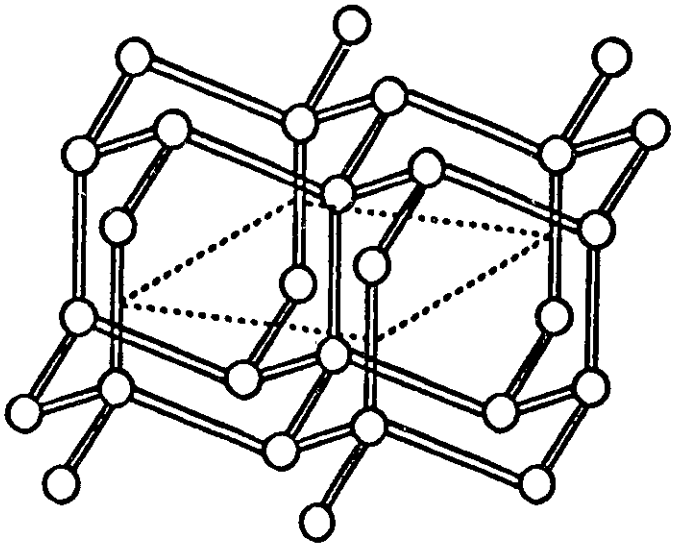

(d)

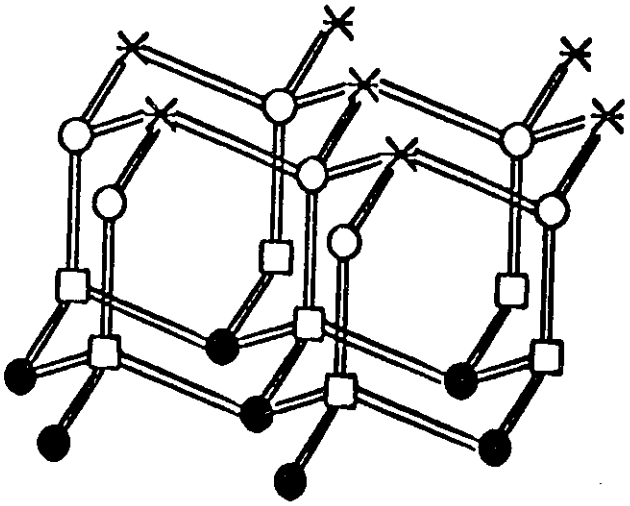

Fig. 37 (a) Four layers of the perfect silicon lattice with the x, y, z directions used in the simulations. (b) and (c) indicate the glide and shuffle plane (surrounded by the dashed line) respectively. (d) The same plot but with different symbols for each layers. Asterisks, open circles, squares and solid circles represent atoms of the top glide plane, the first shuffle plane, the second shuffle plane and the bottom glide plane respectively.

strain over the entire region containing the relaxed dislocation. Then again, keeping the atoms in the x and y boundaries regions fixed, the remaining atoms were relaxed. When fully relaxed, the resultant configuration was examined for any change in the location of the dislocation. Starting with the relaxed unstressed dislocation each time, the stress imposed was varied until the change in the location of the dislocation was one exact repeat lattice distance. The corresponding stress was taken as the minimum stress required to move the dislocation. The Peierls stress for that particular dislocation and orientation was deduced by projection onto the Burgers vector. Different sizes of models with atoms from 3000 to 15000 were tested in order to eliminate finite size effects.

5.3 Simulation Results

A view of the perfect silicon with four layers of atoms and the x, y and z directions used in the simulations is presented in Fig. 37(a). To make the plots easy to read, different symbols were used for each layer (Fig. 37(d)). Asterisks, open circles, squares and solid circles represent what I decided to call the top glide plane, the first shuffle plane, the second shuffle plane and the bottom glide plane respectively. The shuffle dislocations were introduced between the open circles and squares (see Fig. 37(c)) that is between the two shuffle planes, and the glide dislocations between the second shuffle and bottom glide plane (Fig. 37(b)), which is between the squares and the solid circles. The projections of those atoms along the y [111] direction is shown in Fig. 38. Fig. 38(a) shows the projection of two shuffle planes where the atoms of the first shuffle plane (open circles) and the second shuffle plane (squares) are on

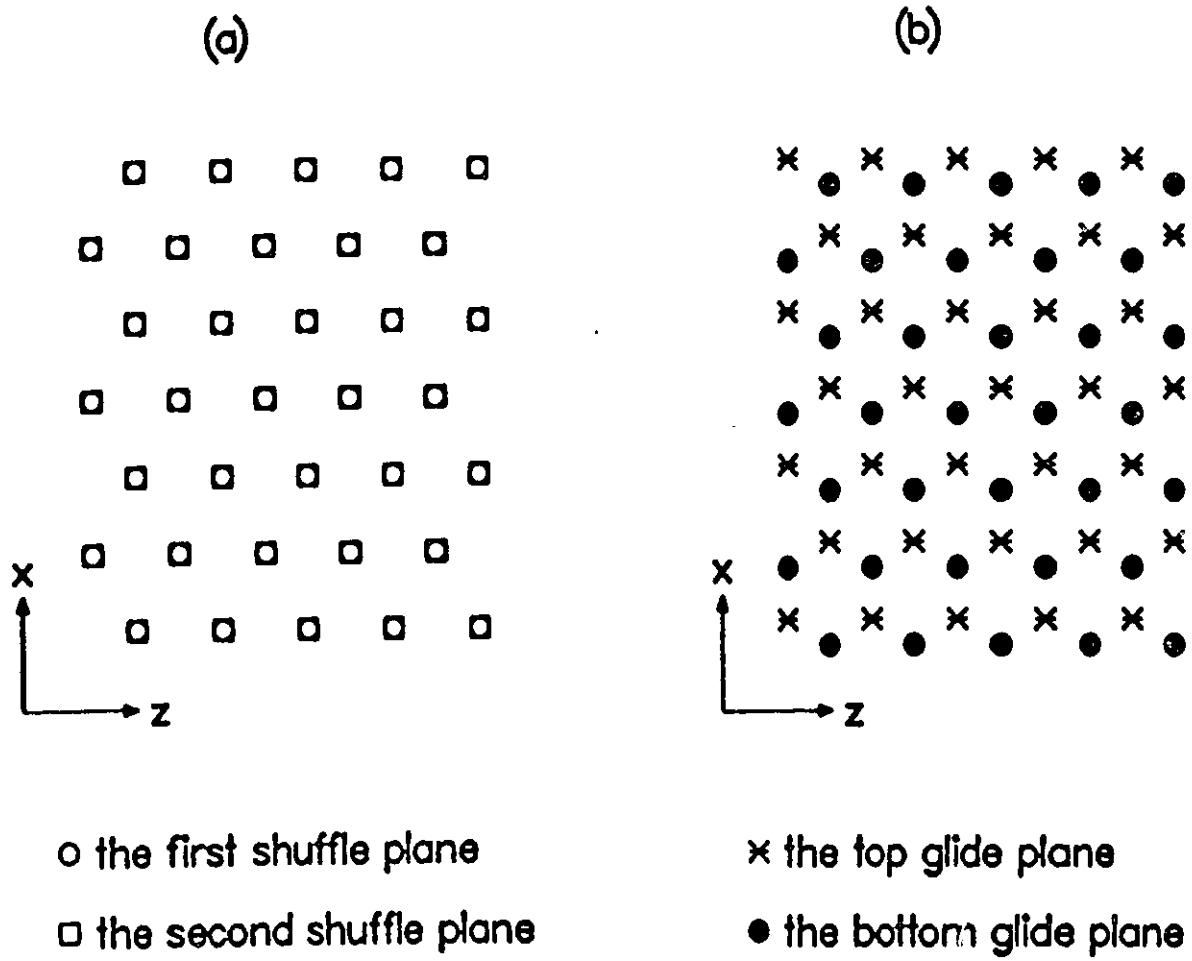

Fig. 38 The projections of Fig. 37(d) along the y or [111] direction. (a) shows the projections of the two shuffle planes. The open circles and squares represent atoms of the first and the second shuffle planes, respectively. Note that for the perfect lattice, atoms of those two shuffle planes are on top of each other along the y direction. (b) shows the projections of the two glide planes. The asterisks and solid circles represent atoms of the top and the bottom glide planes, respectively. In this case, atoms of those two glide planes are in the centres of each other along the y direction.

top of each other and Fig. 38(b) is the projection of two glide planes where the atoms from the different planes (asterisks and solid circles) are in the centres of each other. In the following part of this chapter, I will use these kinds of two dimensional [111] projections (**2dp**) to present the simulation results. For shuffle dislocations, only the first and second shuffle planes are used to display the configuration of atoms while for glide dislocations, the top and bottom glide planes are used.

Bearing in mind that, in 2dp, different symbols represent different planes and for the perfect lattice, atoms from two shuffle planes are on top of each other whereas the atoms from two glide planes are in the centres of one another. Let us look at an example of this kind of plotting but with one dislocation. Fig. 39 shows the 2dp of two *ideal* partial dislocations, 30° and 90° partial dislocations. In each graph, the dislocations are in the middle of the graphs with the dislocation lines along the z directions. Every arrow appearing in the plots is drawn from the atoms' original positions to their displaced positions on the bottom glide plane. Dislocations are created by moving half planes of atoms from the bottom glide plane a small distance with respect to the top glide plane. The arrows in this case are the displacement vectors which are also the Burgers vectors b_p of the partial dislocations. Note that the b_p ($= a/\sqrt{6}$) is shorter than the repeating distance of atoms from the same plane which is the Burgers vector b ($= a/\sqrt{2}$) of the perfect dislocations in silicon. That is why these dislocations are called partial dislocations. Here a (= 5.43 Å) is the lattice constant of silicon. The angles between arrows and the dislocation lines, which are the connecting lines of the ending points of arrows, will determine the characteristics of dislocations, 30° or 90°. The advantage of 2dp is that the position of the dislocation can be easily determined. As we can see from Fig. 39, the dislocation line is

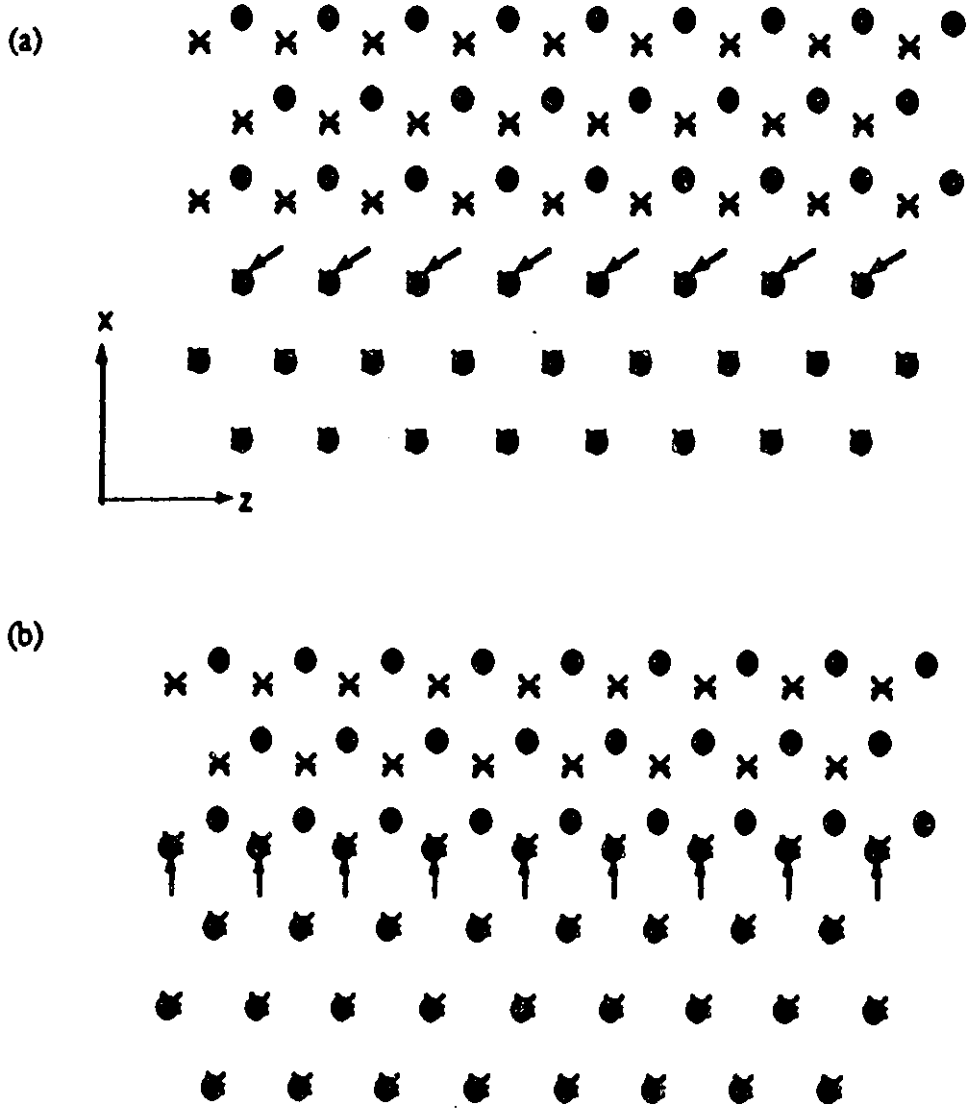

Fig. 39 (a) A silicon lattice with an ideal 30° partial dislocation on the glide plane projected normal to the (111) plane. Two layers of atoms are shown here the top glide plane (asterisks) and the bottom glide plane (solid circles). (b) The same lattice but with an ideal 90° partial dislocation. Every arrow appearing on the plots is drawn from the atoms' original positions to their displaced positions on the bottom glide plane.

factually the boundary between the perfect lattice, where atoms from two glide planes are in the centre of each other, and the displaced lattice, where the atoms are on top of each other. If the introduced dislocations are perfect ones, except for the region near the dislocation core, the configuration of atoms on two sides of dislocation line looks the same as that of the perfect lattice since the relative displacement of the top and bottom glide plane is one exact repeating distance of lattice. In this way, in 2dp, by examining the relative positions of atoms from two different planes, we can decide the characteristics of a dislocation, whether it is a partial, screw, or 60° one.

5.3.1 Dislocation Profile

One of the important assumptions of the Peierls-Nabarro model is that the dislocation distribution is planar [22]. Under this assumption, the dislocation only spreads along its Burgers vector direction. It is easy to verify this assumption by using lattice configurations calculated from simulations. I use the screw dislocations as examples. Fig. 40 shows the silicon lattices with the screw dislocations projected normal to (111) plane. Two layers of atoms in which the dislocation is introduced are shown for each plot. Fig. 40(a) shows a 2dp of a shuffle screw dislocation with atoms from the first shuffle plane (open circles) and the second shuffle plane (squares). Before introducing the dislocation, a series of atoms (squares) A,B,C,...,K on the solid line in the second shuffle plane were chosen along with their nearest neighbour atoms a,b,c,...,k on dashed line (open circles) in the first shuffle plane. The pair separations of Aa,Bb,Cc,..., Kk are zero for the perfect lattice. After introducing a screw shuffle dislocation between two planes, it is seen that these pair separations have been changed (Fig. 40(a)). For

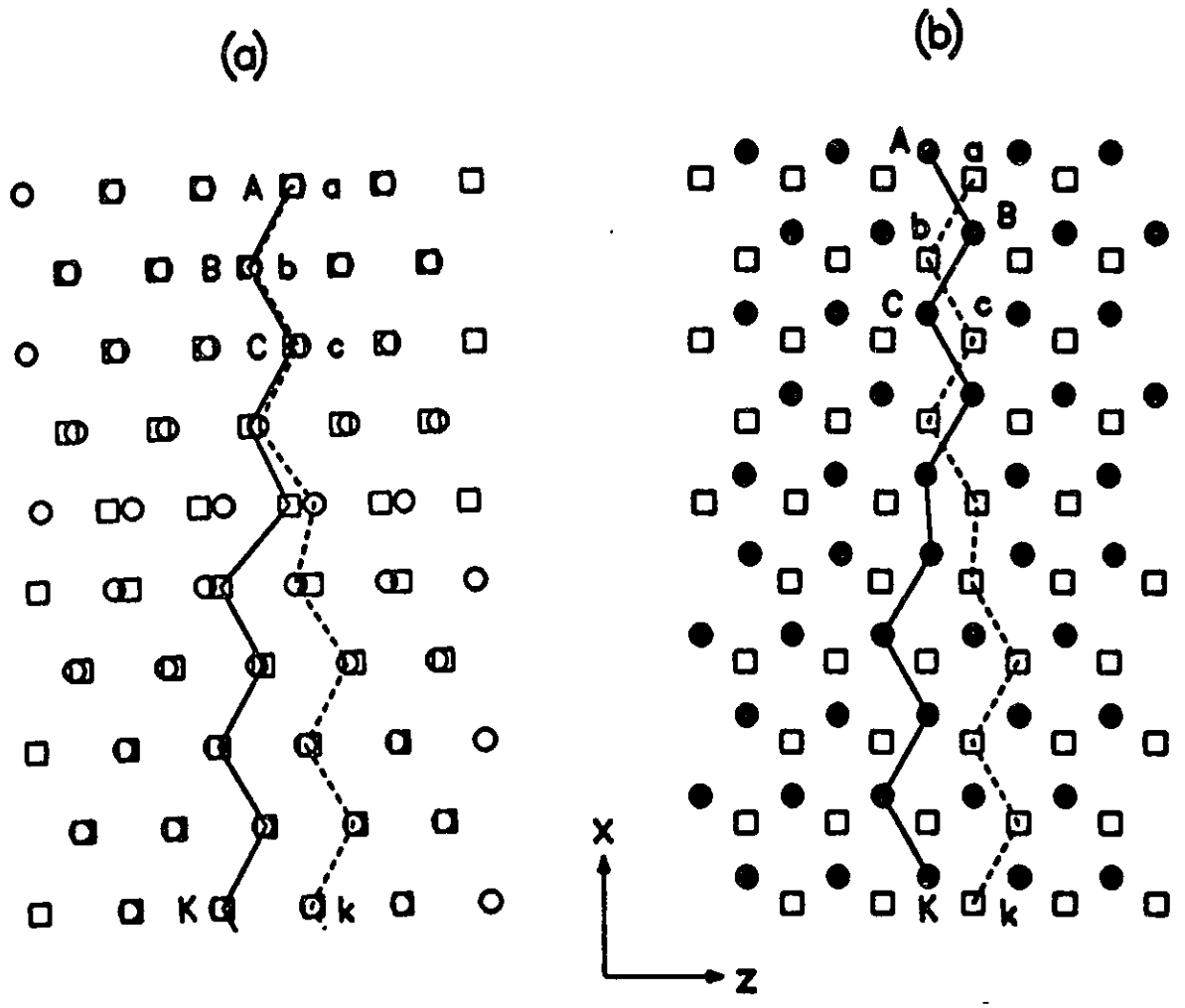

- the first shuffle plane
- the second shuffle plane

atoms on the first shuffle plane

atoms on the second shuffle plane

- the second shuffle plane
- the bottom glide plane

atoms on the second shuffle plane

atoms on the bottom glide plane

Fig. 40 The silicon lattices with the screw dislocations projected normal to the (111) plane. Two layers of atoms are shown for each plot. (a) A shuffle screw dislocation with the first shuffle plane (open circles) and the second shuffle plane (squares). The screw dislocation is introduced between those two planes shown right in the middle of the plot along the z direction. (b) A glide screw dislocation introduced between the second shuffle plane (squares) and the bottom glide plane (solid circles). Before introducing the dislocation, a series of atoms A,B,C,...on the solid line in the second shuffle plane for the shuffle dislocation , or the bottom glide plane for the glide dislocation were chosen along with their nearest neighbour atoms a,b,c,... on the dashed line in the first shuffle plane for the shuffle dislocation or the second shuffle plane for the glide dislocation. The changes of the relative pair separations such as Aa; Bb; Cc; ... are used to calculate the displacement profile of the screw dislocation shown in Fig. 40.

the configuration above the dislocation line, the positions of atoms such as A,B or C are just slightly displayed away from atom a,b or c. As soon as crossing the dislocation line, the atoms of the second shuffle plane move one repeating distance away from those on the first shuffle plane (-z direction). Take pair Kk for an example. Without any dislocation Kk is zero. Right now, K atom (square) is displayed -b away from k atom (open circle). Since the displacement is parallel to the dislocation line (z direction), this is a screw dislocation. The variation of pair separations is used to calculate the displacement field of the shuffle screw dislocation. A similar graph of a glide screw dislocation is shown in Fig. 40(b). This projection is not exactly the 2dp discussed earlier. Instead of using projections of the two glide planes, I used the projection of the second shuffle plane (square) and the bottom glide plane since the glide dislocation is introduced between these two planes. As we can see from Fig. 40(b), it is a little bit harder to study the changes of pair separations such as Aa, Bb,..., Kk. Even for the perfect lattice they are not equal to zero. However, we still can find that for pair Kk, K atom (solid circle) moves from the right side of k (square) to its left. Again displacement is along the -z direction. To understand this result, we should remember that, without the dislocation, the configuration of pair Kk would be the same as that of Bb. Since Bb is the periodic counterpart of Kk as we follow the zig-zag solid-dashed lines along the x direction.

From the above projection graphs, I can only indirectly show the displacement components along the x and z directions. However, the displacement vector has three components. Displacements along the x, y, and z directions plotted as functions of the x positions of the atoms are shown in Fig. 41. The solid lines represent the results of the glide screw dislocation while the dashed lines for the shuffle screw dislocation. As we expect, for the

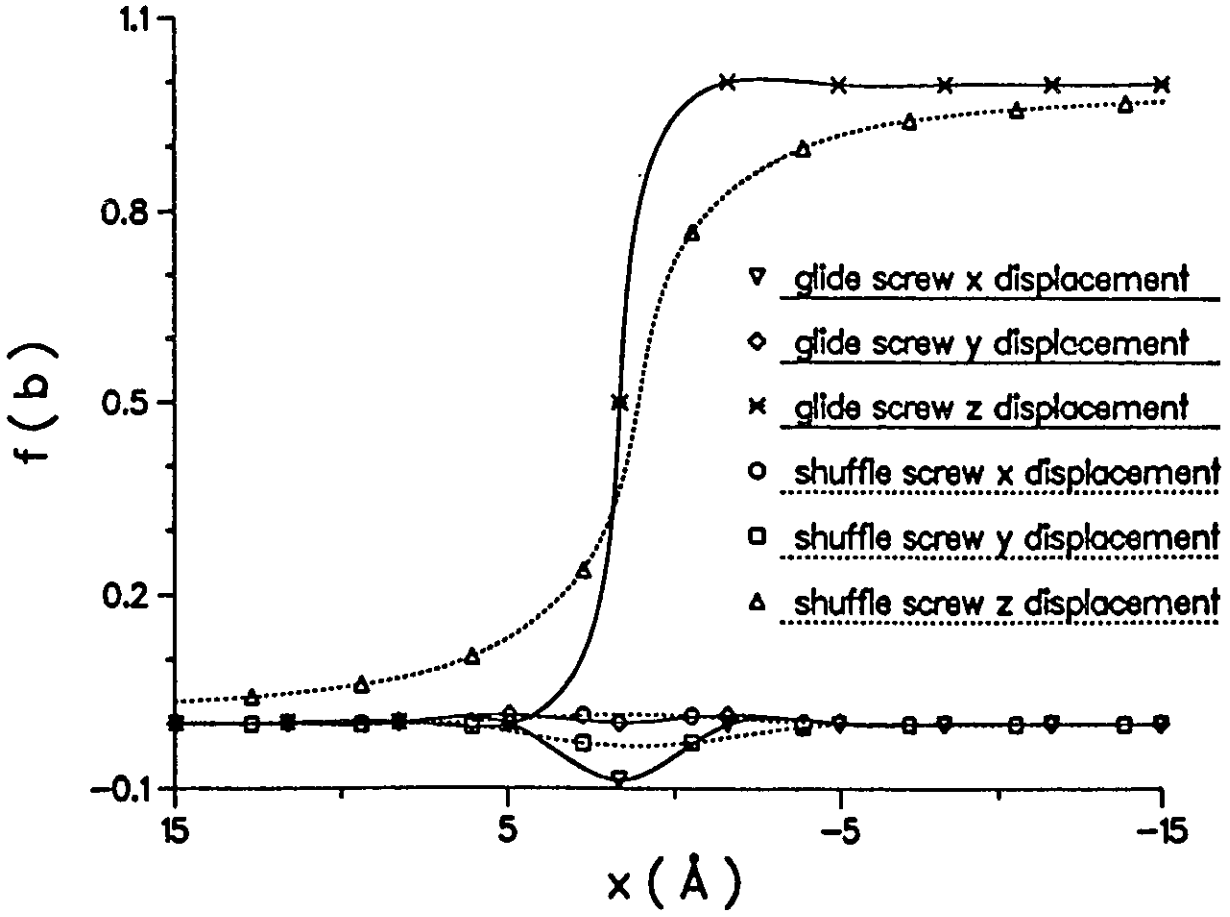

Fig. 41 Dislocation profiles of the screw dislocations. The x,y z components of displacement plotted as functions of the x positions of the atoms. The solid lines represent the results of the glide screw dislocation and the dashed lines for the shuffle screw dislocation.

screw dislocations, the dislocation displacements are seen to be mainly constrained along the Burgers vectors, which is the z direction, for both glide and shuffle dislocations. Above the dislocation line, (+x direction), such as pair Aa,Bb, the z component is very small, and below the dislocation line (-x direction), such as pair Kk the z component gradually becomes the Burgers vector b. The shapes of the dislocation profiles also give a measure of the extent of the core region that can not be described by linear elasticity. The width of the screw dislocation can be approximately determined by the region where the z component is greater than half of Burgers vector [22]. The width of screw shuffle dislocation is found to be 3Å. The corresponding width of screw glide dislocations is quite narrow, only about 0.3Å. Theose results are in good agreement with our Peierls-Nabarro model calculations. In addition to the z direction, the displacements also spread along the x (glide screw) or y (shuffle screw) direction. But those symmetric distributions are quite small compared with those of the z direction which is the Burgers vector direction.

5.3.2 Peierls Stress

To maintain periodic boundary conditions along the z-axis the shear stress was applied within the (111) plane. It was found that the Peierls stress (**PS**) is isotropic within that plane. In other words the minimum stress required to move the dislocation in any direction within that plane has the same projection unto the Burgers vector, the PS of the dislocation.

The possible effect of the finite size of the block upon the calculated PS has been tested by carrying out some calculations for different block sizes, but the differences were found to be negligible.

5.3.3 Shuffle Dislocations

The 2dp of a relaxed core configuration of a 60° shuffle dislocation is shown in Fig. 42(a). It is seen that the dislocation has a core region with atoms (open circles) on a,c dashed lines in the first shuffle plane and atoms (squares) on A,B,C solid lines in the second shuffle plane. Line B (solid squares) on the second shuffle plane is an extra line of atoms since it doesn't have the corresponding neighbour atoms on the first shuffle plane. The Burgers vector is at 60° with line B. The dislocation has been created by cutting between two shuffle planes, and moving half of the second shuffle plane by one Burgers vector and rejoining the atoms on either side of the cut. The line B is the dislocation line. In the silicon lattice, the line B is actually an extra half plane. When stress reaches the PS value, the following transformation occurs. First, atoms of line A move toward those of line a. Then atoms on line B glide along the Burgers vector direction toward those on line c, thus pushing the atoms on C away to form a new extra line of atoms shown in solid squares (see Fig. 42(b)). Eventually the dislocation moves down one repeating lattice distance. The Peierls stress was found to be 0.075μ, where μ is the shear modulus for Si (μ = 0.426 eV/Å^3 [22]). For the case of the screw shuffle dislocation, the relaxed core is shown in Fig. 43(a). Seven lines of atoms are shown in this graph. Since there is a shuffle screw dislocation in the graph, starting from the first line, we can observe that the atoms on the second shuffle plane (squares) move away from those on the first shuffle plane (open circles). The direction of displacement is along the -z direction. The dislocation line is right between the third and fourth line. Note the changes in positions of the atoms (squares), from the left side of open circles (atoms in the first shuffle plane), to the right.

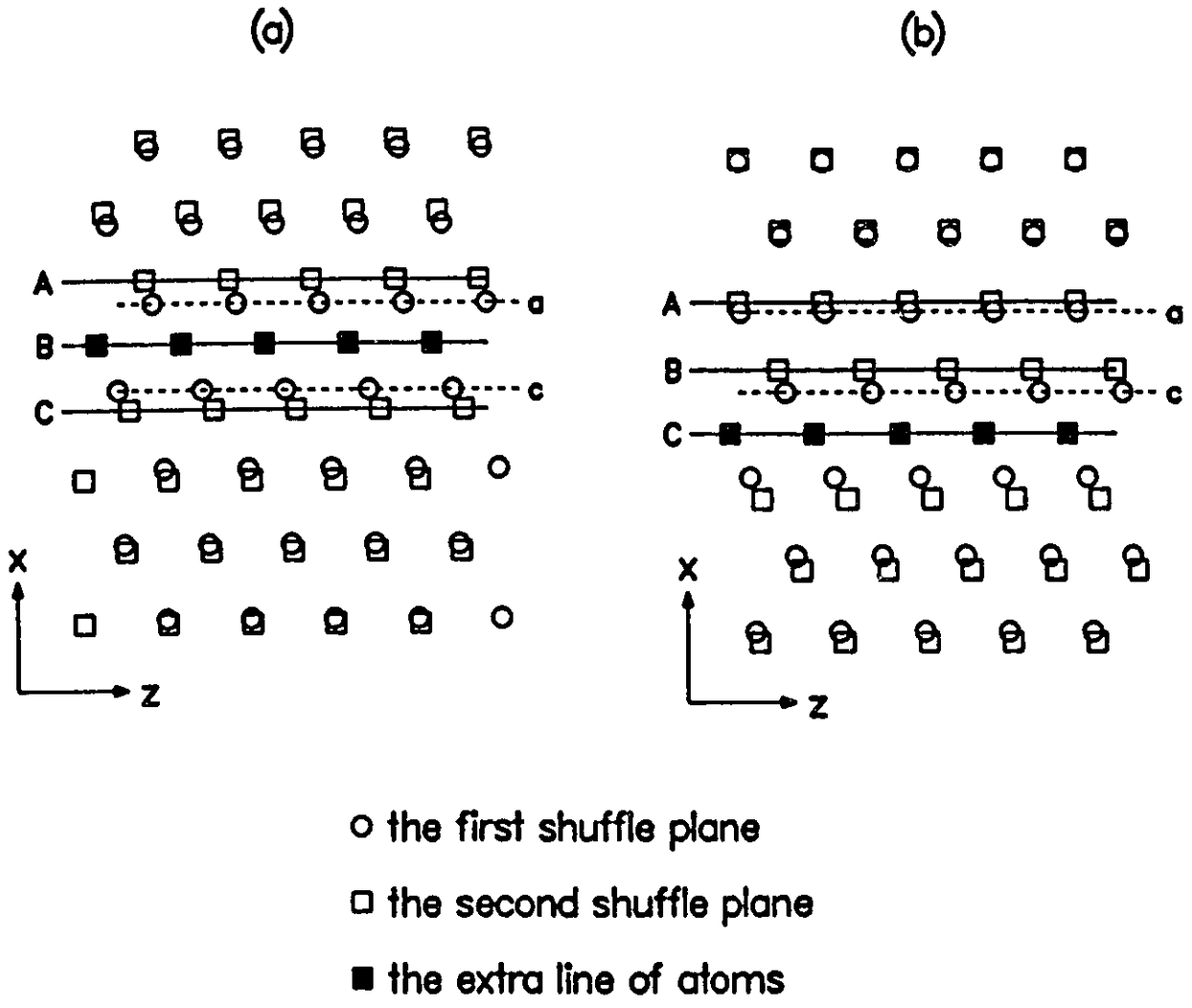

Fig. 42 Gliding of a 60° shuffle dislocation. (a) The (111) projection of a relaxed dislocation with the core region consisted of atoms on dashed lines a and b in the first shuffle plane and atoms on solid lines A,B and C in the second shuffle plane. Line B is a line of extra atoms represented by solid squares. (b) The same dislocation under an applied shear stress of 0.075μ on (111) plane. Note that dislocation moves one repeat lattice down and line C on the second shuffle plane becomes the new extra line of atoms.

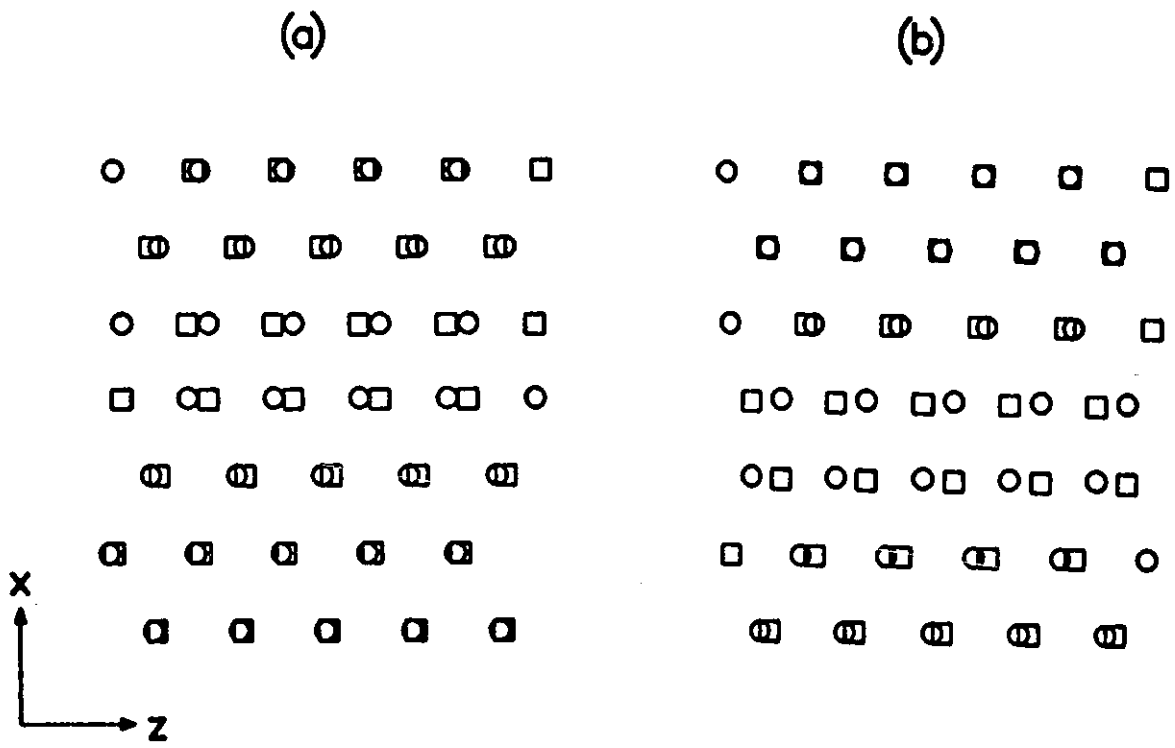

○ the first shuffle plane

□ the second shuffle plane

Fig. 43 Gliding of a screw shuffle dislocation. (a) The (111) projection of a relaxed dislocation and (b) the same dislocation under an applied shear stress of 0.086μ on (111) plane.

Fig. 43(b) shows the configuration ot the lattice under the Peierls stress. The dislocation line here is between the fourth and fifth line. The dislocation moves down one repeating distance. The stress was found to be 0.086μ which is higher than one for the 60° shuffle dislocation.

During the relaxation procedure, shuffle dislocations were introduced at different positions in the block and various shear stresses were applied. However, both shuffle dislocations started to move if the stress were greater than the Peierls stress. No dissociation was found. Fig. 44 is the 2dp configuration of a dissociated 60° shuffle dislocation with a 90° and 30° partials calculated by elasticity theory. The dashed lines and arrows represent the positions and Burgers vectors of the two partials respectively. We used this configuration as our starting point, after the relaxation was completed, the dislocation collapsed into a single 60° shuffle dislocation as shown in Fig. 42(a). The same situation happened to the screw shuffle dislocation as well.

5.3.4 Partial Dislocations

To obtain the Peierls stresses of the partial dislocations, the simulation was carried out on either one of the two sets of partials--30° & 30°partial (dissociated screw dislocation), or 30° & 90° partial (dissociated 60° dislocation), which are separated by a stacking fault on the [111] plane. Since a single partial dislocation is not observed in experiments. A relaxed 90° partial dislocation obtained from 2dp configuration is shown in Fig. 45(a). The dislocation line ξ is the boundary between a layer of stacking fault above, where the atoms on the top glide are on top of atoms on the bottom glide plane, and the perfect lattice at the lower part. The Burgers vector is perpendicular to the line ξ. Under a proper stress, the relative distances of atoms on line A

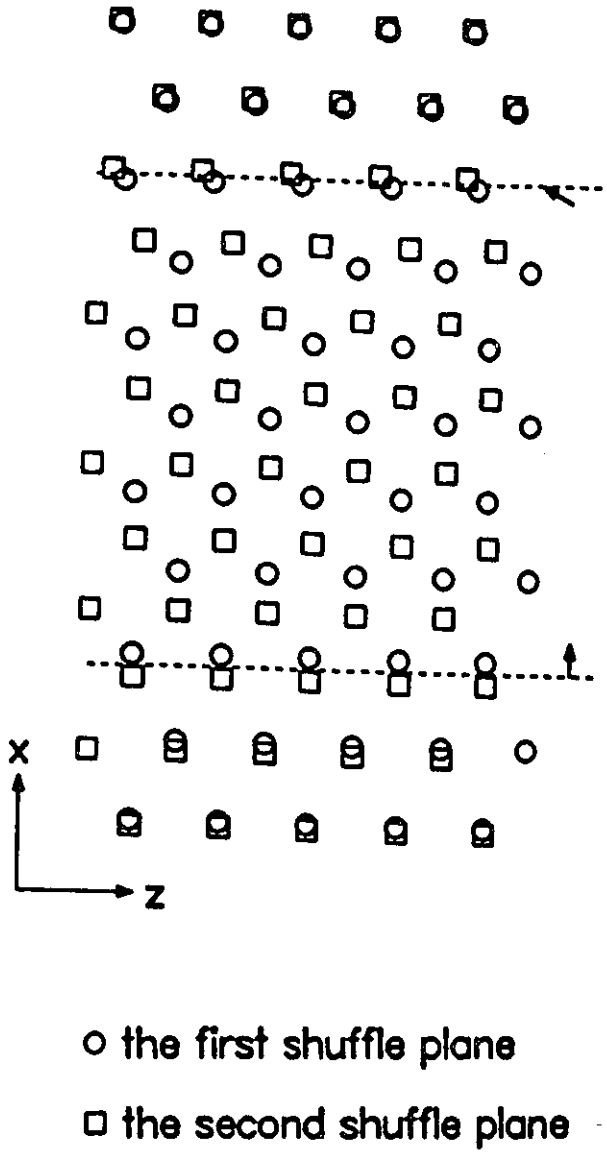

Fig. 44 The (111) projection of the configuration of a dissociated 60° shuffle dislocation calculated by elasticity theory. Between two dashed lines is a layer of stacking fault with a 90° partial at lower part and a 30° partial at upper part. The arrows represent the Burgers vectors of two partials.

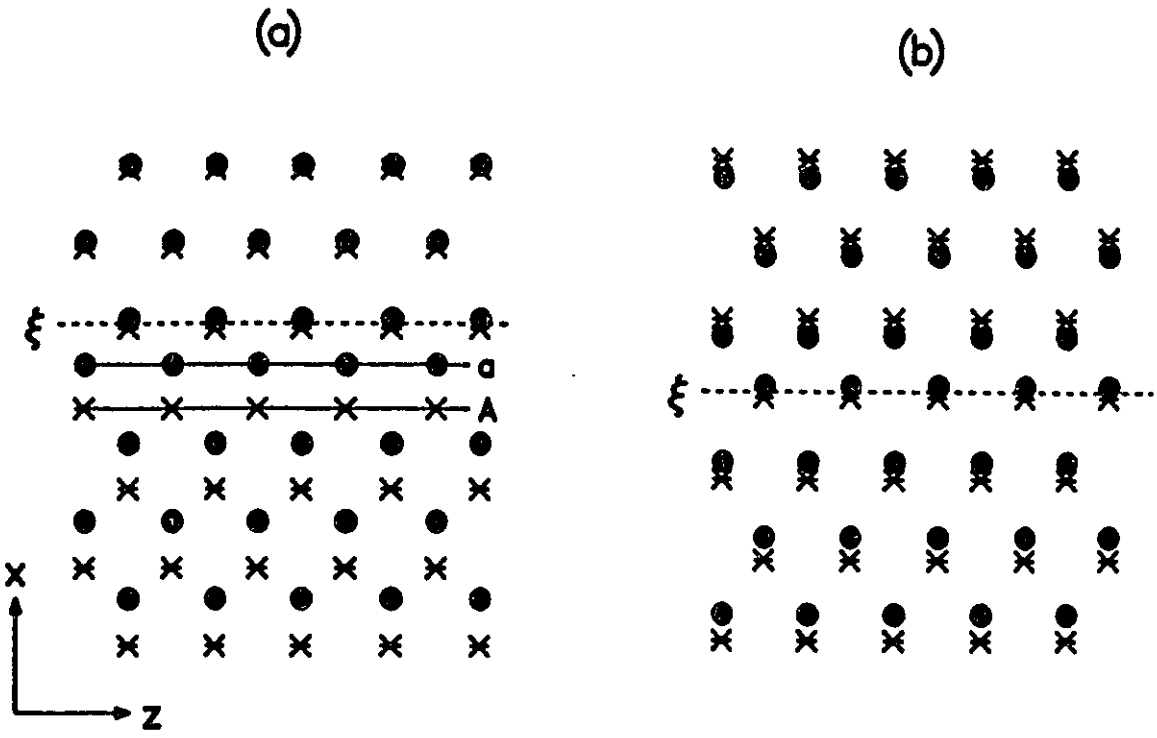

Fig. 45 Gliding of a 90° partial dislocation. The dashed line ξ represents the dislocation line and the Burgers vector is perpendicular to ξ. (a) The projection of a relaxed dislocation along the [111] direction. Two solid lines A and a are on the bottom and top glide plane respectively. (b) shows the result of (a) under an applied shear stress of 0.25μ. Note that line A and line a form the new dislocation line ξ due to the changes of their relative positions under the stress.

in the bottom glide plane and those on line a in the top glide plane decrease until they reach the same configuration of atoms on line ξ . This new line (dashed) becomes the boundary between the stacking fault and perfect lattice shown in Fig. 45(b). The Peierls stress to initiate this kind of motion was found to be 0.25μ. At a stress level of 0.31μ, a relaxed 30° partial dislocation of Fig. 46(a) moves one repeating lattice down (note the dislocation line ξ) into Fig. 46(b). The changes of the relative positions of atoms on the two glide planes are the same as for the 90° partial.

5.3.5 Glide Dislocations

Fig. 47(a) shows a 2dp of a core of glide screw dislocation. Dashed line ξ is the dislocation line. Open circles near the dislocation line were the original positions of atoms on the bottom glide plane without any dislocation. Arrows on the plot indicate the displacements of the atoms (solid circles) after introdution of a screw dislocation. When a shear stress is applied to Fig. 47(a), the core of dislocation starts to dissociate into two 30° partials (Fig. 47(b)). The area between the two dashed lines is a layer of stacking fault whose width is only one repeating lattice distance. Arrows indicate the directions of the two Burgers vectors. As the stress increases, no dislocation movement is found until the stress is greater than the Peierls stress of one of the partials such as the lower one for our case. This partial starts to glide one repeating lattice down and expand the area of the stacking fault between two partials, which is the area between the two dashed lines in Fig. 47(c). When the stress building on the trailing partial also reaches its Peierls stress level, the trailing partial begins to move as well. The analogous behaviour was found in the 60° glide dislocation as well. The only difference is that

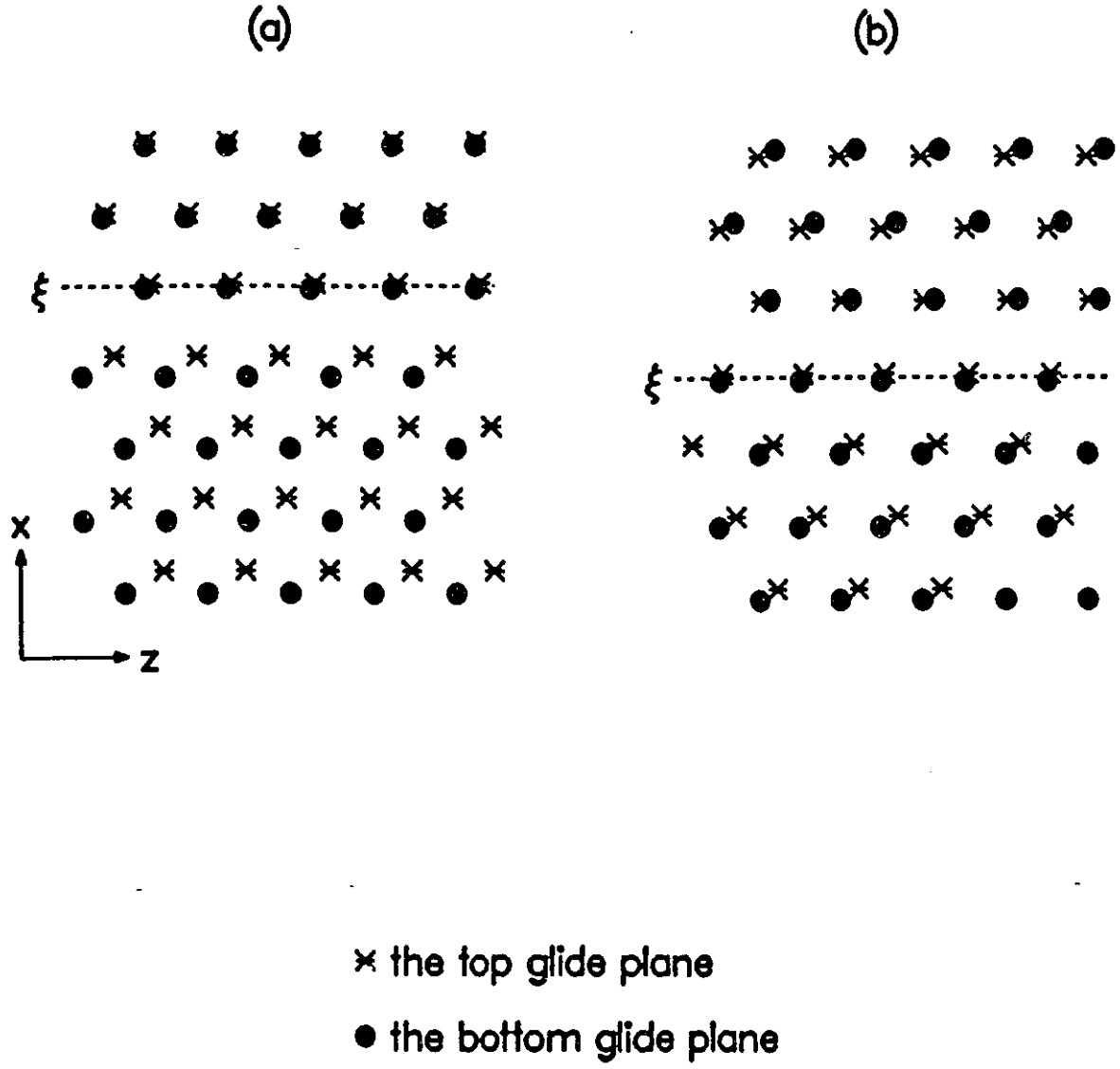

Fig. 46 Gliding of a 30° partial dislocation. Notations are the same as Fig. 45 except that the Burgers vector is at 30° with the dislocation line ξ and the shear stress for (b) is 0.31μ.

(a)

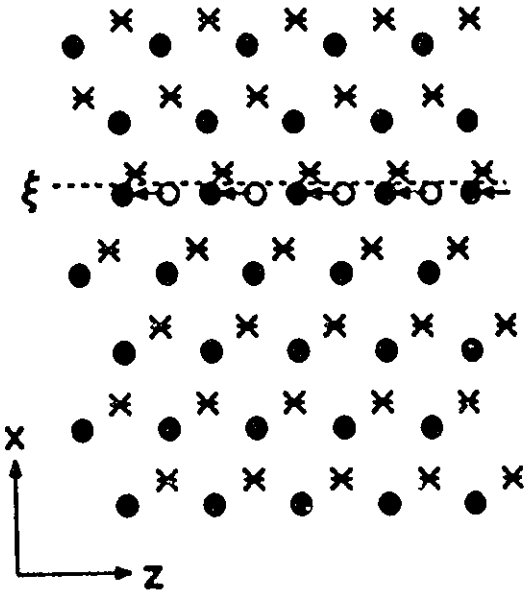

(b)

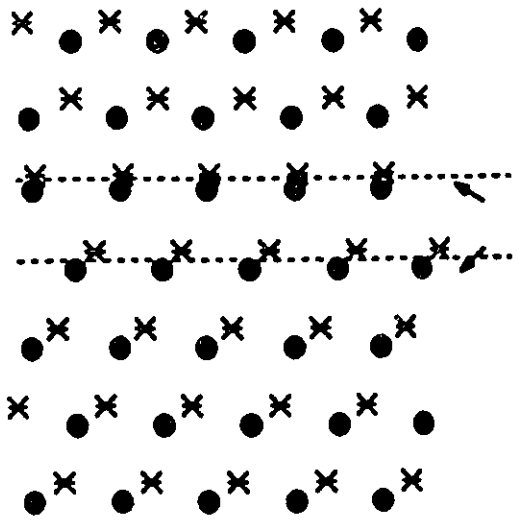

× the top glide plane

● the bottom glide plane

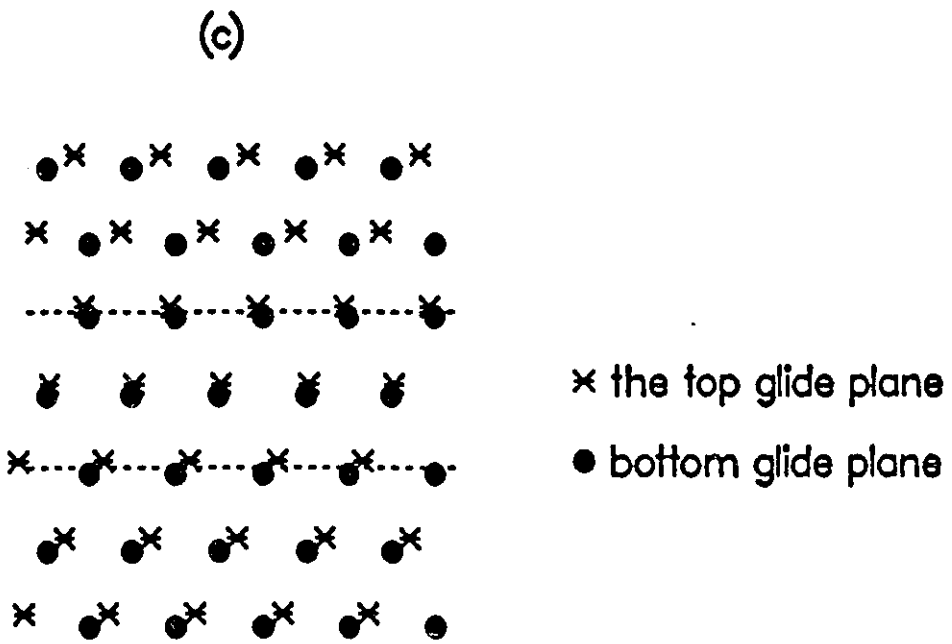

Fig. 47 Dissociation and motion of the glide screw dislocation. (a) The (111) projection of a relaxed core configuration of a glide screw dislocation. Dashed line ξ is the dislocation line. Every arrow on the plot shows the displacement of the atoms from their original positions (open circles) to their final displaced positions (solid circles) on the bottom glide plane. (b) Applied shear stress of 0.16ξ to (a). Note that dislocation starts to dissociate into two 30° partials which are represented by two dashed lines with their Burgers vectors indicating by the arrows. (c) When the shear stress reaches the Peierls stress level of the lower partial, this partial starts to move down and the stacking fault area (between two dashed lines) is expanded.

the dislocation dissociates into a 30° and a 90° partial.

In summary, the slipping of the glide dislocation is accomplished by dissociation into partials and the movement of partials. In other words, the glide dislocation can only glide in **dissociated** form.

5.4 Discussion and Conclusion

The first conclusion is that dislocations in Si are quite planar. In the core region, the displacements away from the Burgers vector direction are very small.

We also found that, if no reconstruction is allowed, the motion of the shuffle set dislocations in Si at 0K is easier than one would have expected. Actually, they are very stable against any dissociation. On the other hand, the glide set dislocations can *only* move in dissociated forms. In other words that the motion of a glide dislocation is accomplished by, first, dissociation into partials on the glide plane, and then gliding of the partials.

The results of obtained Peierls stresses for all the dislocation are shown in TABLE 5.1 along with those calculated by Peierls-Nabarro model [79]. Despite of the limitation of the PN model, which treats the dislocation as planar and our SW potential which is not the potential constructed by the first principle density calculation, the agreement between these two methods is very good. These agreements indicate that the PN model can give the correct relationship between generalized stacking fault energy surface characteristics and the properties of dislocations at low temperatures.

TABLE 5.1. Comparison of Peierls stresses in Si obtained from Peierls-Nabarro model σ_p and with those from relaxation on the SW potential model σ_{sw}. (μ = 0.426 eV/Å^3)

dislocation	σ_{sw} (μ)	σ_p (μ)
glide 60°	dissociated	16.92
glide screw	dissociated	21.29
shuffle 60°	0.075	0.083
shuffle screw	0.086	0.112
glide partial 90°	0.25	0.282
glide partial 30°	0.31	0.351

Both our PN and SW potential model calculations suggest that, in Si at 0K, shuffle-set dislocations should be easier to form and move than those belonging to the glide set. However, experimental observations show that total dislocations in Si are dissociated into partial dislocations separated by an intrinsic stacking fault. Since this fault can only exist on the glide planes, the general wisdom is that mobile dislocations belong to the glide set (although it has been argued that this inference is not without question [51]). It is possible that finite temperature effects may alter the conclusions of the calculations. Kaxiras and Duesbery [54] have shown that if entropy is taken account, then above a critical temperature and in the presence of a tensile stress, the free energy of the unstable stacking fault γ_{us} can become lower on the glide planes than on the shuffle set. It is also possible that complex reconstruction of the dislocation core,

which lies beyond the PN model and is excluded from the SW potential model, is responsible for this difference. But both our two models do show that 90° partials have lower Peierls stresses than those of 30° partials.

The calculated Peierls stresses and their isotropy in the glide plane can be used to explained the available experimental data on the mobility of partial dislocation in silicon [49,63,64]. It is known that, under the applied stress, the response of dissociation width of 30° & 90° partial with 90° leading, 30° & 90° partial with 30° leading and 30° & 30° partial are quite different. For the 90° leading case, the dissociation width is widened, while for the 90° trailing, the width is narrowed. and for 30° & 30° partials, the dissociation width would most likely be the same. The reasons behind these differences are illustrated in Fig. 48. The Fig. 48(a) and (b) are the dissociated 60° dislocation with the 90° partial trailing and the 90° partial leading, respectively and Fig. 48(c) is the dissociated screw dislocation. According to our calculation, the most efficient way to move a dislocation is to apply the stress along the Burgers vector direction b. For Fig. 48(a) and (b), if we apply the external stress along b, even though 30° & 90° partial get the same resolved shear stress along their Burgers vector directions, the 90° partial will start to move first no matter whether it is trailing or leading partial because it has lower Peierls stress than the 30° partial. If it is a leading partial the width of the stacking fault will be wider, and if it is trailing, the width will be narrower. These different mobilities of the two partials will become more significant if the external shear stress is applied perpendicular to the stacking fault, which is often the case in experiments. In this situation, all of the external stress is used to move the 90° partial while only part of it is used to move the 30° partial which already has a higher Peierls stress. These factors will make the 30° partial even harder to move.

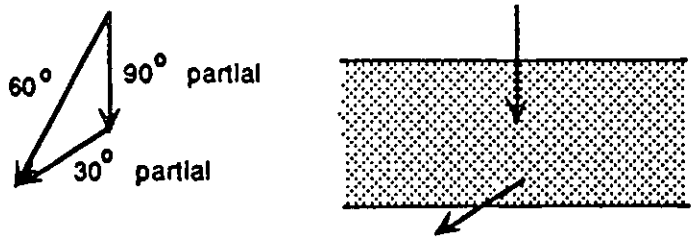

(a)

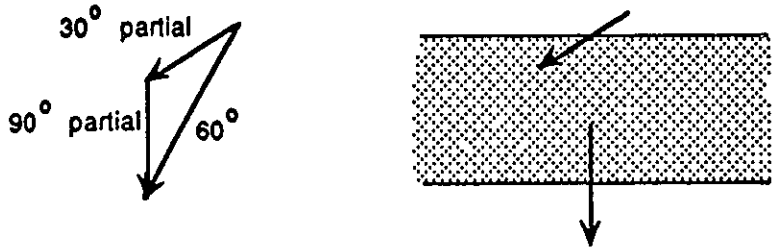

(b)

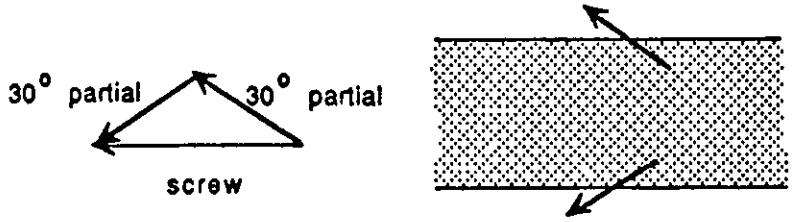

(c)

Fig. 48 (a) A dissociated 60° dislocation with a 90° partial leading. (b) A dissociated 60° dislocation with a 30° partial leading. (c) A dissociated screw dislocation with two 30° partials. The shadow areas are the stacking fault layers.

For the two 30° partials of the screw dislocation, they get the same amount of shear stress component if the external stress is along the Burgers vector of a screw, they are more likely to move at the same time and keep the width between them unchanged.

Mainly what this study has shown is that the PN model can give quantitative estimates of dislocation properties. What needs to be seen now is the effect of the reconstruction. Will it explain the glide-shuffle controversy? And what effect will reconstruction have on the PS of the dislocations in particular the shuffle set?

Chapter 6. Misfit Dislocations in Epitaxial Strained Layers (ESL)

6.1 Introduction

Structures of epitaxial strained layers (ESL) represent a major extension of the class of semiconductor materials. These structures form the basis for a new field of semiconductor research, which offers the prospect of novel solid-state devices with new or improved characteristics. ESL are grown as layers of semiconductor materials with lattice mismatches of as much as several percent. If the ESL are sufficiently thin the lattice mismatch is accommodated within the layers by uniform biaxial strain. The result is a high quality structure with coherent interfaces in which the structural modulation creates a new electronic band structure. ESL structures allow previously unknown freedom in the combination of lattice mismatched materials that, when combined with the effects of strain on the band structure, provide an unprecedented ability to tailor optical and electronic properties [88].

As is often the case in nature, however, the same feature of ESL that provides new possibilities, the mismatch strain, also presents limits to realization of this potential. In this case, the limit is associated with the structural stability of ESL. Briefly the critical thickness h_c that separates a regime of stable ESL structures from those in which the ESL structure is thermodynamically unstable is a function of the lattice mismatch and the details of the overall structure [89]. ESL thinner than the critical thickness are stable when strained into interfacial

coherence, whereas thicker layers possess enough strain energy to force the interfaces to become incoherent (shown in Fig. 49). This occurs by formation of misfit dislocations that interact strongly with the electronic carriers and may render the resulting structure unsuitable for device applications.

The magnitude of this critical thickness has been calculated using equilibrium theory by a large number of authors [89-92]. However, recently there has been a growing recognition that in practice, strain relaxation is kinetically limited. Finite misfit dislocation nucleation and propagation rates ensure that when the critical thickness is exceeded, the structure does not instantaneously achieve its equilibrium strain state at finite temperature [93]. Rather, the structure may be grown to substantially greater thickness than equilibrium critical thickness predictions, before detectable densities of misfit dislocations are observed [93,94]. This "metastable" growth regime is encouraged by lower growth temperature, higher Peierls stresses to dislocation motion, and higher energy barriers for dislocation nucleation. A classic example of this metastable growth regime is in the Ge_xSi_{1-x}/Si(100) system at a growth temperature of 550°C [95], where for relatively dilute Ge concentrations, ESL thickness may be grown to an order of magnitude greater than equilibrium predictions of h_c before misfit dislocations are present in substantial densities. Increasing the growth temperature (e.g. to 750°C in Ge_xSi_{1-x}/Si system [96],), decreasing the Peierls stress (e.g. by comparison to another system such as In_xGa_{1-x}/GaAs [97]), increasing the available dislocation source density [98] or increasing the experimental sensitivity to dislocations [99], all compress the apparent metastable regime.

Much theoretical and experimental progress in modelling and understanding the kinetic of strain relief has been made in the last few years, particular in Ge_xSi_{1-x}/Si(100) system [93,

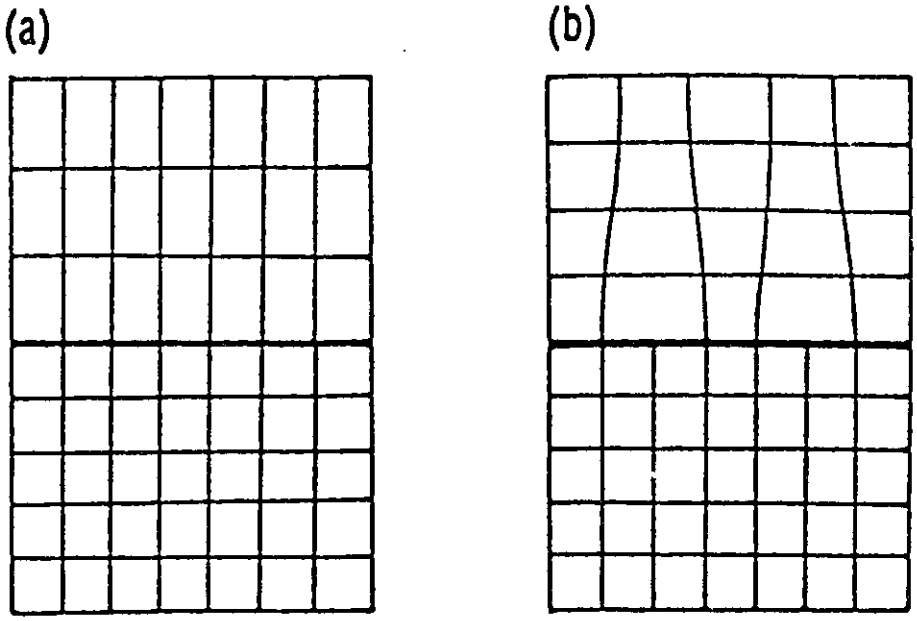

Fig. 49 Schematic illustration of (a) a epitaxial strained layer with $h < h_c$ and (b) with $h > h_c$. Note that two misfit dislocations are formed in the interface.

100-104] and to a lesser extent in the In_xGa_{1-x}/GaAs(100) system [105-107]. But the precise mechanisms of nucleation of misfit dislocations still remain elusive and controversial. The generic candidates for misfit dislocations are

1. Multiplication mechanisms arising from dislocation pinning and/or interaction processes [108-113].
2. Heterogeneous nucleation at specific local stress concentrations due, for example, to growth artifacts or preexisting substrate defects [114-118].
3. Homogeneous or spontaneous nucleation of dislocation loops or half-loops [22, 115, 117, 119-122].

The idea of a regenerative dislocation source goes as far back as the Frank-Read source [108]. Probably the first application of this concept to ESL was reported by Hagen and Strunk [109]. They proposed a mechanism for which intersections of particular dislocations act as sources of dislocation multiplication. The experimental evidence for this mechanism 1 was quite compelling (for a review see ref. [123]). Mechanism 3 cannot occur on laboratory time scales for strains of practical interest [115,121,124]. The remaining major source of misfit dislocations is mechanism 2. However, growth artifacts and substrate defects can be reduced to very low concentrations.

Another possibility is that uniform strained layers are unstable against modulation of the surface profile [125-130]. The driving force for the surface instabilities is that, although it increases the surface area, it also allows a partial relaxation of the strain by purely elastic deformation of the film and substrate. These provide points of large stress where the barrier to nucleation of dislocations is extremely small [131-133].

In this part of the thesis, I study the conditions for two competing relaxation mechanisms of ESL. One is the surface roughening which allows easy nucleation of dislocations. Another is nucleation of misfit dislocations at specific stress concentrations such as the edges of the ESL. The roles of various lattice mismatch and layer thickness on misfit dislocation nucleation and propagation have been investigated. Calculations also extended to the detail strain relaxation process for a certain ESL at various lattice mismatches.

6.2 Existing Models of ESL

In this section I review existing understanding of misfit dislocation microstructure, energetics and kinetics for ESL.

6.2.1 Equilibrium Critical Thickness

The concept of a critical thickness for the lattice mismatched ESL, above which mismatch stress is partially relieved by misfit dislocations and below which the structure is stable against misfit-relieving dislocations is several decades old [89]. The simplest conceptual illustration and calculation of this critical thickness, and the one most commonly applied to ESL, is the Matthews-Blakeslee (**MB**) " Mechanical Equilibrium" model [91]. This model balances an applied stress σ_a, acting on a threading dislocation traversing the ESL with the stress due to the "line tension", σ_T of created interfacial misfit dislocations (see Fig. 50).

The lattice mismatch stress experienced by the dislocation threading arm is given by:

$$\sigma_a = 2\mu\varepsilon_o \frac{(1+\nu)}{(1-\nu)} \cos\lambda\cos\phi \qquad \ldots(6.1)$$

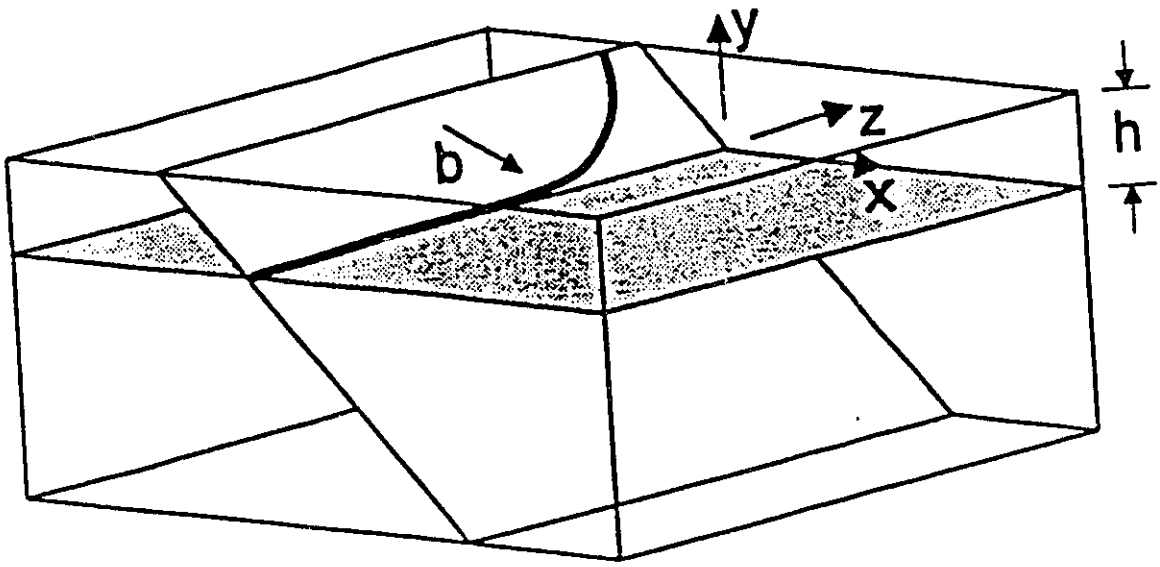

Fig. 50 Schematic diagram of a dislocation in a epitaxial strained layer with a glissile threading segment and its trailing interface misfit segment.

In equation (6.1), μ is the ESL shear modulus, ε_o is the lattice mismatch strain between ESL and substrate $\varepsilon_o = (a_e - a_s)/a_e$, where a_s and a_e are the lattice parameters of the substrate and ESL, and ν is the Poisson ratio of the ESL. The angular factor in equation (6.1), $\cos\lambda\cos\phi$, is often referred to as the Schmid factor. Here λ is the angle between the dislocation Burgers vector and the line in the interface which is normal to the misfit dislocation line direction, and ϕ is the angle between the glide plane and the interfacial normal.

The restoring stress due to the dislocation "line tension" is given from standard expressions for the self energy of a straight dislocation in equation (2.8):

$$\sigma_T = \frac{\mu b \cos\phi (1-\nu\cos^2\theta)}{4\pi h(1-\nu)} \ln\left(\frac{h}{r_o}\right) \qquad \ldots(6.2)$$

The parameters are the same as defined in equation (2.8).

Equating equations (6.1) and (6.2) and solving for $h = h_c$ then yields the critical thickness:

$$h_c = \frac{b(1-\nu\cos^2\theta)}{8\pi(1+\nu)\varepsilon\cos\lambda} \ln\left(\frac{h_c}{r_o}\right) \qquad \ldots(6.3)$$

Because of the core radius r_o, we can not apply equation (6.3) to the ultra thin ESL.

6.2.2 Kinetic Strain Relaxation

The MB model is generally accepted as being formally correct for predicting that the ESL thickness at which creation of interfacial misfit dislocations is first energetically favoured. It says nothing, however, about strain relaxation rates at finite temperatures. When the critical thickness is exceeded during ESL growth, strain relaxation rates will depend upon the dislocation

nucleation rate, the dislocation propagation velocity and the dislocation interactions.

Dodson and Tsao (DT) [93] created a theoretical framework to describe finite strain relaxation rates based upon the concept of "excess stress", $\sigma_{ex} = \sigma_a - \sigma_T$, see equation (6.1) and (6.2). By analogy to measured dislocation velocities during deformation of bulk semiconductors [134,135], they assumed that dislocations propagate with a velocity, v, approximately proportional to the excess stress, and controlled by thermal activation over the inter-atomic Peierls stress, such that:

$$v = v_o \sigma_{ex} e^{-\frac{E(\sigma)_v}{kT}} \qquad \ldots(6.4)$$

The activation energy, E_v, for 60° a/2<110> dislocations is measured in bulk semiconductors to be of the order 2.2 eV in Si [134,135], 1.6 eV in Ge [136] and 1.0 eV in InAs and GaAs [50].

6.3 Simulation Models

The model system used in the present study is a two-dimensional triangular lattice with interactions defined by the Lennard-Jones potential (LJP) as defined in equation (3.18). The interactions between the various atoms are modeled using one of three potentials: V_s, V_e, V_{se}, all of which are LJP with three parameters ϵ (ϵ_s, ϵ_e, and ϵ_{se}) and three parameters σ (σ_s, σ_e, and σ_{se}). Potential V_s and V_e model the interactions among ESL and substrate atom. V_{se} simulations

the interactions of atoms at interface. ϵ_s and σ_s are used as the units of energy and length. I chose the parameter $\epsilon_e = 0.9\ \epsilon_s$ for the ESL taking into considerations that silicon and germanium have different properties [137] and the fact that the most common structures for ESL are $Si_{1-x}Ge_x$. Since for LJP the equilibrium lattice constant is proportional to the parameter σ, I select the $\sigma_e = (1+x)\ \sigma_s$. By changing the input value of x, I can the vary the misfit $\epsilon_o = x/(1+x) \approx x$ of the system. The parameter ϵ_{se} and σ_{se} are given by the Lorentz-Berthelot rule [138] for the mixtures

$$\epsilon_{se} = \sqrt{\epsilon_s \epsilon_e}$$
$$\sigma_{se} = \frac{\sigma_s + \sigma_e}{2} \qquad \ldots (6.5)$$

The relaxation technique used in this part of the calculations is the same as discussed in chapter 3. The simulation cell is a parallelogram composed of two parts. The bottom part is the substrate with equilibrium lattice. It consists of 50 rows time 95 columns of atoms. The top part is the ESL with the lattice constant x% larger than that in the substrate. The bottom two rows of the substrate are held fixed while free boundary conditions are imposed on the other three sides. These conditions effectively model the ESL on a large substrate, in order to investigate the effects of the lattice mismatch and layer thickness of ESL on its relaxation mechanism. A representative structure of the 5 ESL on the substrate is shown in Fig. 51. Only half of the substrate atoms are displayed in the graph.

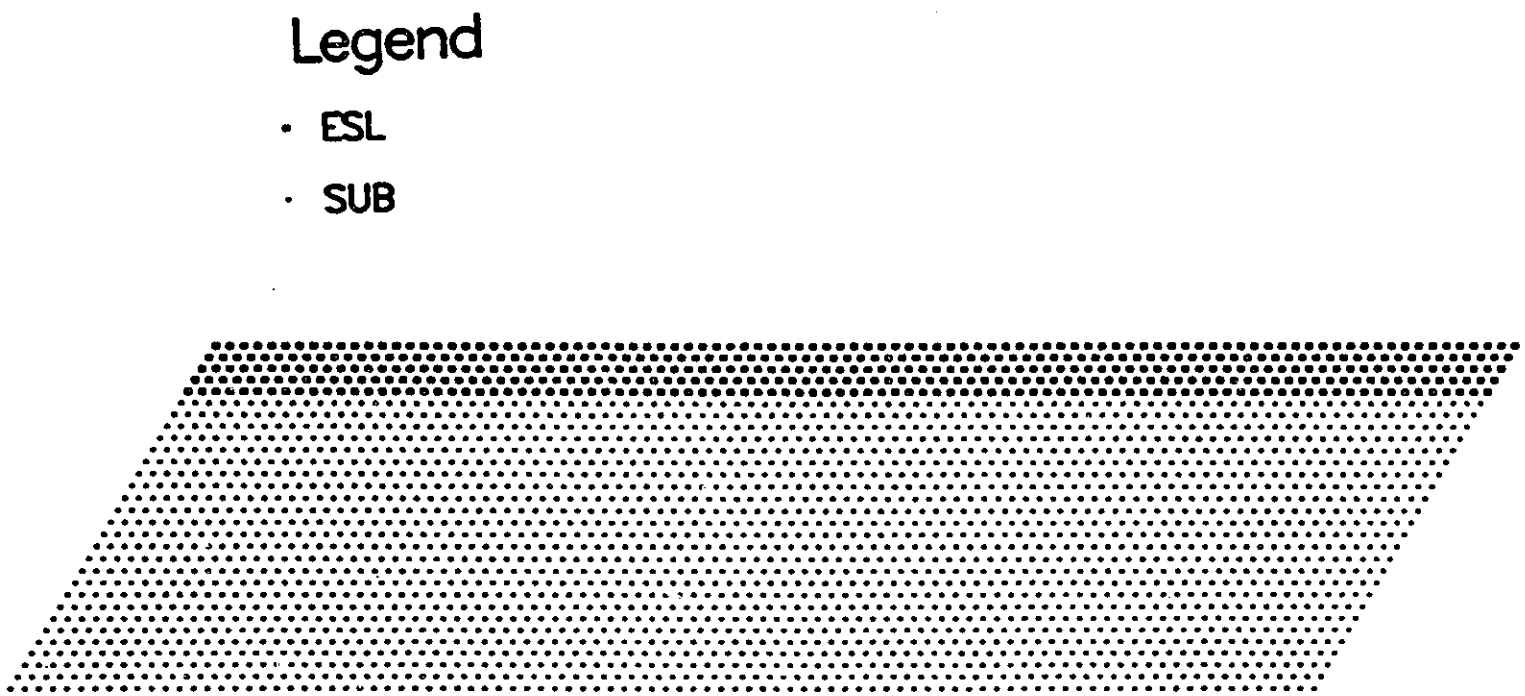

Fig. 51 The typical initial configuration of the simulation cell with 5 layers of ESL and 50 layers of substrate (SUB). Only half thickness of the SUB atoms are shown here. SUB atoms are represented by • and ESL atoms by * .

6.4 Simulation Results

I only focus on the ultrathin ESL whose layer thickness is smaller than 10 layers owing to the limitations of the computer relaxation time. We also know from the discussion in section 6.2.1 that this is the range for which the well accepted MB model fails because of the core of the dislocation. And the ultrathin ESL is the initial stage of the epitaxial growth. To fully understand the mechanism of strain relief in this stage will help to control the growth process to get the defect-free ESL.

6.4.1 Strain relaxation process

We first look at the dependence on the misfit of the ESL. The starting configuration was the 5 layer ESL with various misfits. The ESL in this case is compressed. In the process of relaxation the internal stress of the ESL will push the atoms to the side of the layers. I plotted on Fig. 52 the average energy per atom, the main part being the strain energy, as a function of misfit. The misfits I considered were from 1% to 12%. As we can see from Fig. 52, for the small misfit such as 3% to point a, the ESL is stable. The strain energy increases linearly with respect to the misfit, which is predicted by elasticity theory [22]. As soon as the misfit reaches point a, the coherent ESL becomes incoherent with one misfit dislocation appearing at the right side of the system. This dislocation is nucleated by pushing one line of ESL atoms out of the substrate (see the right side of Fig. 53). As the misfit increases to point b, another misfit dislocation appears at the left side of system (see the left side of Fig. 53). These two misfit dislocations start to move towards the centre part of the ESL as the misfit passes b. This kind of dislocation movement becomes energetically favourable. It brings the strain energy down. The arrows in Fig. 53 indicate the new positions of the misfit dislocations. Later, the gliding of these

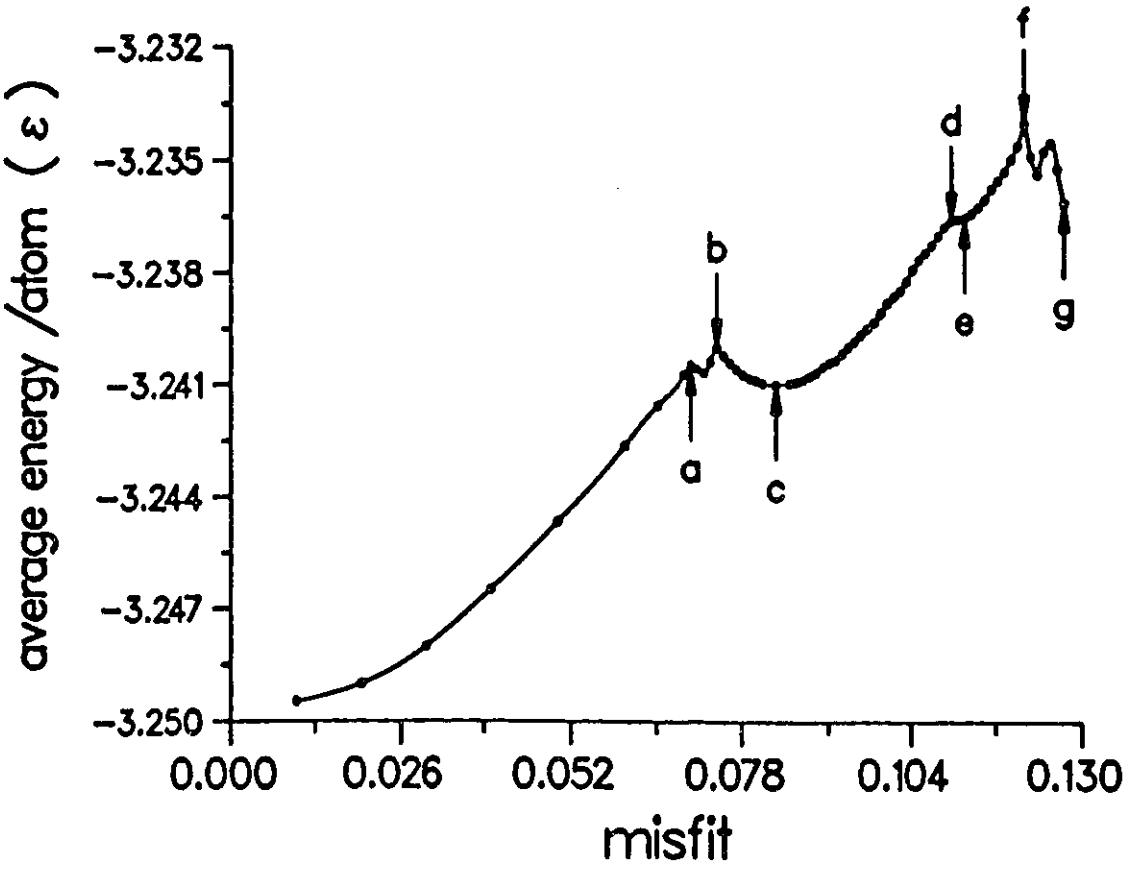

Fig. 52 The strain energy change as a function of misfit. Points a & b are the misfits for which the first pair of dislocations nucleated from the edges. At point c, the first pair of dislocation stops to move toward the centre. Points d & e are the misfits for generating the second pair of dislocations. At point f, the surface becomes unstable and at point g the dislocation starts to nucleate from the rough surface.

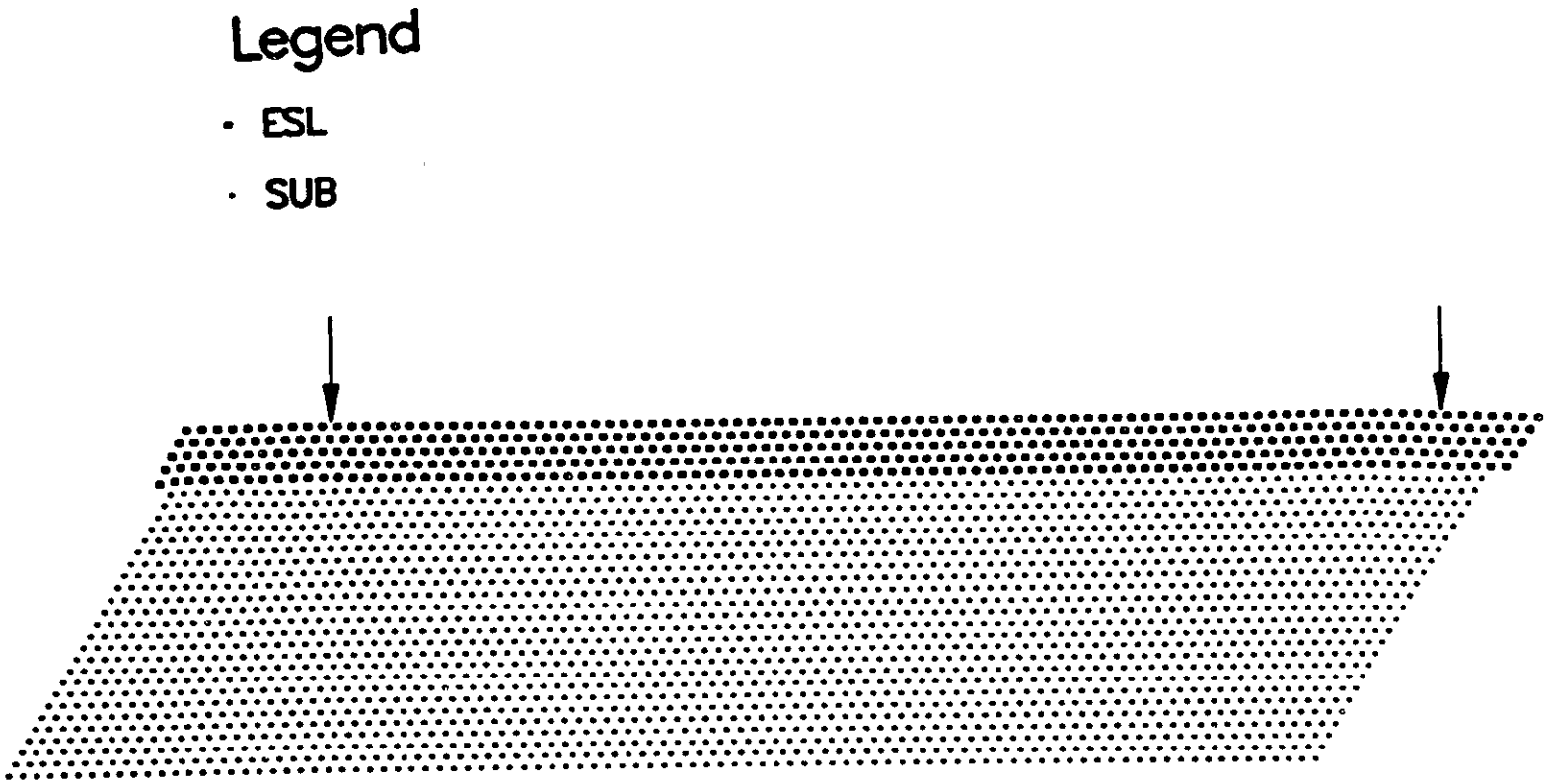

Fig. 53 The representative configuration with two misfit dislocations nucleated from the edges of the ESL. The final positions of misfit dislocations are indicated by arrows.

two misfit dislocations becomes sluggish and stops completely when the misfit equals c, where the right misfit dislocation is only about 22a from the edge and the left one is about 18a from the left edge and leaves the large part of centre unrelaxed. Here a is the lattice repeating distance at the interface. From the c to d, the strain energy increases linearly with respect to misfit again. We can further verify that during this period the two misfit dislocations actually do not move at all. Note that the slope of cd is almost the same as the initial 3% to a. This indicates that from c to d, the gain of the atom energy is all from the strain energy. At point d, another misfit dislocation is formed at the right side of the ESL and at point c, the fourth misfit dislocation is formed from the left. Since the strain at two sides of system has been partly relieved by the first pair of misfit dislocation, there is not enough room for the second pair of dislocations to advance toward the centre. The second pair of dislocations stops at only 5 ~ 6a from the edge. The corresponding energy is not reduced as much as the first two misfit dislocations. It can only hold the rising energy curve at a small plateau (de in the graph). As the misfit continues to increase after point e, the stress in the centre part of the ESL becomes much higher than those at the two sides which are alleviated by nucleating two pairs of misfit dislocations. It is not surprising that the surface of ESL becomes unstable in the centre when the misfit is at point f. Fig. 54(a) is the relaxed configuration of the system at point f. Only the centre part of the system is displayed. One atom has been squeezed out of the surface to ease the large compressed stress at the ESL. As the misfit becomes even higher (at point g), the surface becomes very rough, allowing easy nucleation of dislocations (see Fig. 54(b)). The roughening process is energetically favourable which reduces the strain energy dramatically (see f to g in Fig. 52). And the substrate also becomes rough at the interface.

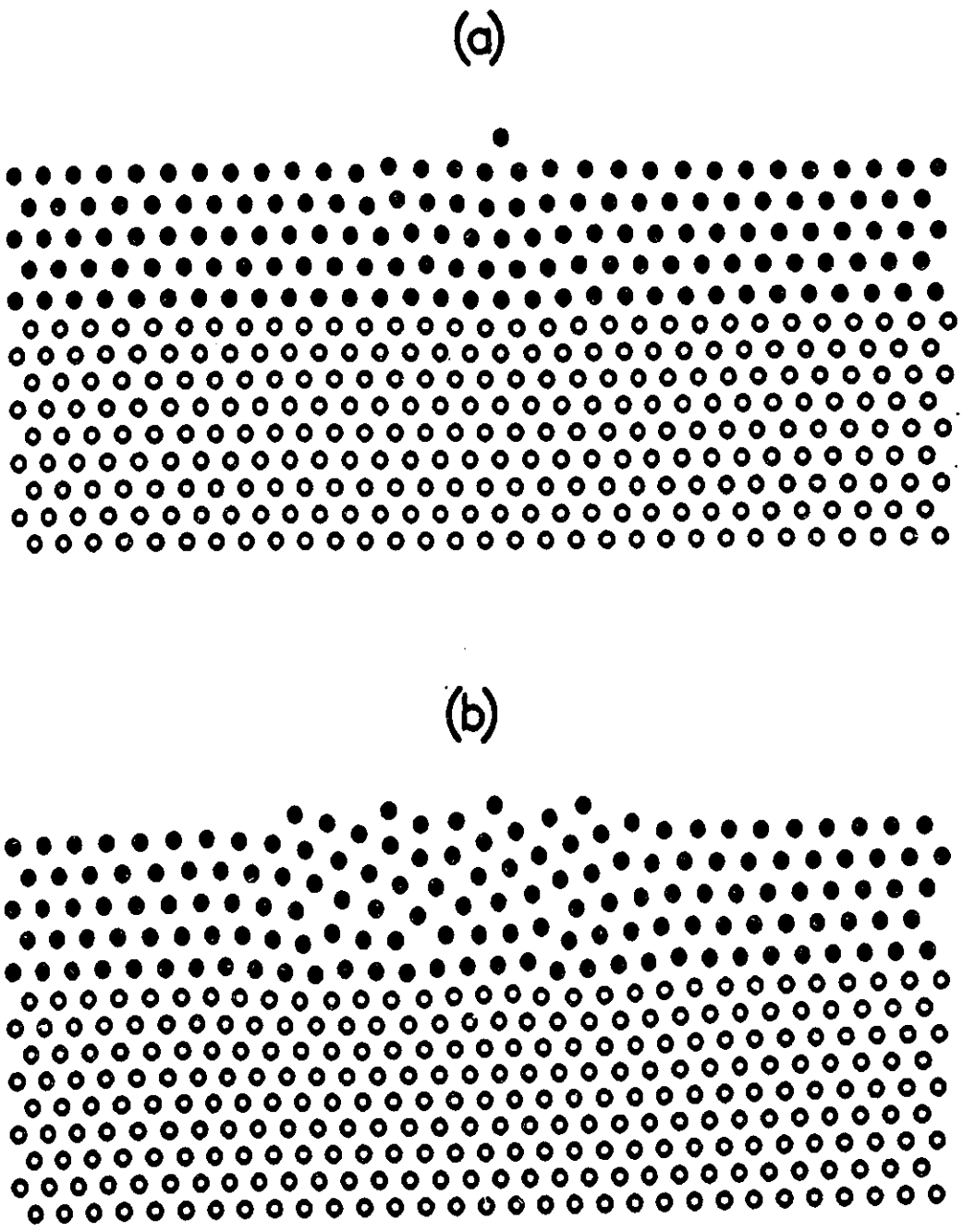

Fig. 54 The configurations of surface roughness with (a) misfit at point f and (b) at point g in Fig. 52. ● and ○ represent the atoms of ESL and substate respectivley.

6.4.2 Misfit Dislocation

As I discussed above, at small misfit, the strain ESL will relax by nucleation of misfit dislocations at existing sources such as the edges of the system where the stress is concentrated. It is interesting to study in detail the nucleation conditions of this kind of dislocation.

In addition to the misfit of the layers, this nucleation mechanism also depends on the thickness of the ESL. The critical misfit for nucleating a dislocation from the edges as a function of thickness of the ESL is shown in Fig. 55. Fig. 55 indicates that the critical misfit decreases linearly as the thickness increases. This suggests that this relaxation process may be more likely to operate in ESL with ten or more layers since the bigger the layer thickness the larger the strain in the ESL. And the higher stress concentration at the edges will make it easy to overcome the energy barrier to nucleate the dislocations.

6.5 Discussion and Conclusion

Here comes the conclusion of this chapter. We find two competing mechanisms of relaxation for the ESL. At small misfit, the strain relaxes by nucleation of misfit dislocation at the existing points of stress concentration. In our case, these are the edges of the system. And this relaxation mechanism is favourable for the thick ESL layers. However misfit dislocations generated by this mechanism can not glide to its *ideal* position in the ESL due to the kinetic barrier. This is quite undesirable for the relaxation of the strain. On one hand, it leaves a large part of layer, which is far from the defects, unrelaxed. And on the other hand, it reduces the

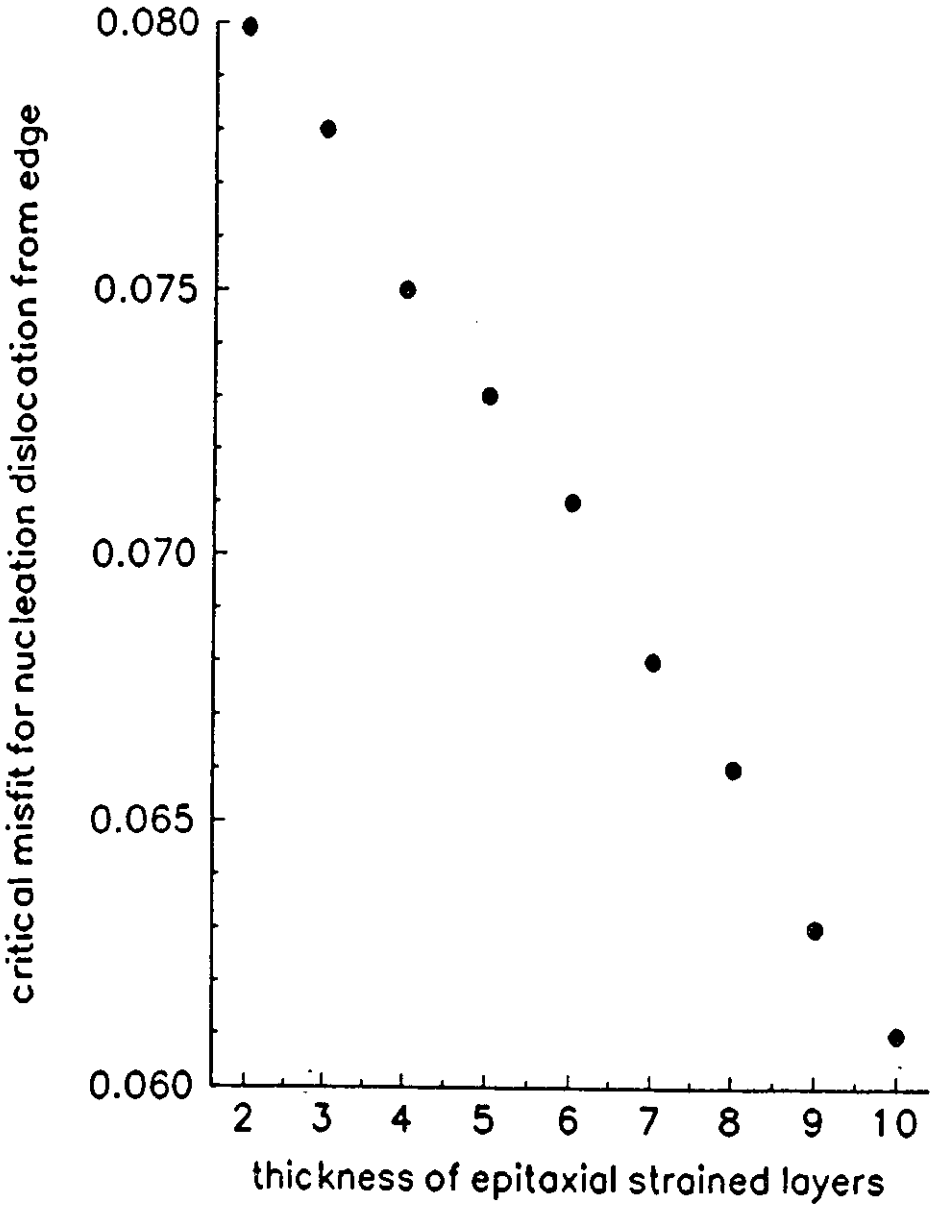

Fig. 55 The critical misfit at which the dislocation nucleates from the edge of the system as a function of the layer thickness.

driving force to nucleate more misfit dislocations from those defects since misfit dislocations are just piled up around them. At large misfit, the surface becomes unstable which provides a low-barrier path for formation of dislocations to relax the strain.

LeGoues and co-workers [102,132] found that the growth of Ge islands on the Si(001) is associated with dislocation nucleation at the edges of the island following sudden enlargement of the size of the island. They also found the two similar competing mechanisms for the ESL. Since the LJP is a weak potential including only two-body interactions, the misfit values we used are relatively high compared with theirs. However, our results seems to be in qualitatively agreement with their experimental ones.

Chapter 7. Conclusion

Dislocations have been studied in two types of systems, monolayers and bulk Si. In monolayers the emphasis was on departure from elastic behaviour. Two interparticle potentials were considered, the Lennard-Jones potential (LJP) and the piecewise linear force potential (PLF). Elasticity theory predicts a logarithmic dependence of the interaction energy on the distance between 2 dislocations, a minimum in dipole interaction for a 45° angle and no Peierls stress. However for the two potentials considered departures from elastic behaviour are more significant than one would have expected. Even in a system such as the PLF system where the forces are all harmonic, the region where the dipoles behave nonelastically is fairly extended and the asymmetry between interstitial and vacancy dipoles is significant. Comparison between the properties of the dislocations in LJP and PLF monolayers shows that the key parameters are the energies of the vacancy and interstitials defects. When the vacancy energy is lower than the elastically predicted core energy value, the lowest energy configuration for a vacancy dipole is a five-fold coordinate vacancy (FCV) configuration. In the LJP system vacancy dipoles are lower in energy because the LJP system is softer under expansion than compression whereas interstitial dipoles tend to be lower in energy in the PLF system because of its soft core. The non-elastic behaviour is larger in both range and magnitude in the LJP system but it is not negligible in the PLF system. In the longer range LJP system the dislocations are harder to form than in the PLF system but easier to move. In the short range PLF system they are easy to form in particular in the compressed systems but hard to move. Except for the anomalous configurations involving a FCV the angular dependence of the dipole energies in the PLF is what is predicted by

elasticity theory with a minimum at 45°. However the angular dependence in the LJP system is significantly smaller than the prediction of elasticity theory. There is still a broad maximum centred around 90° but the energy rise is only about one third of that predicted by elasticity theory, and minimum is closer to 60° than 45°. These studies therefore reveal that in two dimensions dislocation properties depend sensitively on the nature of the interparticle interactions.

For bulk Si, we first constructed a zero-temperature model for dislocations within the framework of a Peierls-Nabarro (PN) model using generalized stacking-fault (GSF) energies obtained from first-principles density-functional calculations. Core width (2ξ), core energies (W(a'/2)), PN pinning energies (W_p) and stresses (σ_p) are calculated for various possible perfect and imperfect dislocations. Those results are listed in TABLE 7.1.

The Stillinger-Weber potential (SW) model simulations are also performed for various dislocations in silicon. We find no evidence of dissociation in the shuffle dislocations. Within this model shuffle dislocations glide along their slipping planes. On the other hand, glide sets are shown to glide *only* in dissociated form. The dislocation displacement fields are shown to be mainly constrained along the Burgers vector. The Peierls stress (PS) is found to be isotropic within the (111) glide plane. In other words, at 0K, the minimum stress required to move the dislocation in any direction within that plane has the same projection unto the Burgers vector, the PS of the dislocation. Our PS are in agreement with those obtained from PN model listed in TABLE 7.1. These agreements indicate that our PN model can give the correct relationship

TABLE 7.1 Properties of dislocations in Si obtained from our PN model (μ = 0.426 eV / Å^3)

Dislocations	2ξ (Å)	W(a'/2) (eV/Å)	W_p (eV/Å)	σ_p (μ)
Glide 60°	0.37	0.169	3.77	16.92
Glide screw	0.30	0.110	3.74	21.29
Shuffle 60°	3.95	0.538	0.116	0.083
Shuffle screw	3.14	0.408	0.148	0.112
Glide 30°	0.92	0.062	0.343	0.351
Glide 90°	1.16	0.093	0.323	0.282

between GSF energy surface characteristics and the properties of dislocations at low temperature in the absence of reconstruction[1] .

Both the PN model and SW simulations show that in Si, at 0K, shuffle set dislocations should be easier to form and move than those belonging to the glide set but experiments do not show that. Temperature may explain the difference through entropy effects [54] or maybe some complex reconstruction is responsible. Our models do show that 90° partials have lower Peierls stresses than those of the 30° partials in accord with experiments.

---

[1]. The effects of reconstruction are not considered in the PN model because it assumes homogeneous displacements along the dislocation line.

Finally, using a simple two dimensional LJP system, we found two relaxation mechanisms in the epitaxial strained layers (ESL). At small misfit, strain is relaxed by nucleating the misfit dislocations from the points of stress concentration. This process is easier for thicker layers. Due to the kinetic barrier of the misfit dislocations, they can not evenly release the stress in the strained layers. At large misfit, the surface where the stress is relatively high becomes rough, and misfit dislocations are generated from the surface to relax the stress.

References

[1] V. Volterra, Ann. Sci. Ec. Norm. Sup., Paris **24**, 401 (1907).

[2] J.H. Michell, Proc. Lond. Math. Soc. **31**, 100 (1900).

[3] G. Weingarten, Atti Accad. naz. Lincei Rc. **10**, 57 (1901).

[4] A. Timpe, Z. math. Phys. **52**, 348 (1905).

[5] A.E.H. Love, *A Treaties on the Mathematical Theory of Elasticity*, 3rd edn (Cambridge: Cambridge University Press).

[6] C. Somigliana, Atti Accad. naz. Lincei Rc. **23**, 463 (1914).

[7] C. Somigliana, Atti Accad. naz. Lincei Rc. **24**, 655 (1915).

[8] C.G. Darwin, Phil. Mag. **27**, 675 (1914).

[9] C.G. Darwin, Phil. Mag. **43**, 800 (1922).

[10] O. Mügge, Neues Jahb. Min. 13 (1883).

[11] A. Ewingg and W. Rosenhain, Phil. Tans. Roy. Soc. A 193, 353 (1899).

[12] L. Prandtl, Z. angew. Math. Mech. **8**, 85 (1928).

[13] U. Dehlinger, Ann. Phys. Lpz. **2**, 749 (1929).

[14] G.I. Tayor, Proc. R. Soc. A **145**, 362 (1934).

[15] E. Orowan, Z. Phys. **89**, 634 (1934).

[16] M. Polanyi, Z. Phys. **89**, 660 (1934).

[17] J.M. Burgers, Proc. Koninkl. Ned. Acad. Wet. **42**, 293 (1939).

[18] R. Peierls, Proc. Phys. Soc. **52**, 34 (1940).

[19] F.R.N. Nabarro, Proc. Phys. Soc. **59**, 256 (1947).

[20] W.L. Bragg, Proc. Phys. Soc. **52**, 54 (1940).

[21] D.W. Pashley, Rep. Prog. Phys. **28**, 291 (1965).

[22] J.P. Hirth and J. Lothe, *Theory of Dislocations* , 2nd ed. (Wiley, New York 1982).

[23] F.R.N. Nabarro, Advan. Phys. **1**, 269 (1952).

[24] L. Lejček, Czech. J. Phys. B **22**, 802 (1970).

[25] J.M. Kosterlitz and D.J. Thouless, J. Phys. C **6**, 1181 (1973).

[26] D.R. Nelson and B.I. Halperin, Phys. Rev. B **19**, 2457 (1979).

[27] A.P. Young, Phys. Rev. B **19**, 1855 (1979).

[28] For an extensive review see K.J. Strandburg, Rev. Mod. Phys. **60**, 161 (1988).

[29] B. Joós and M.S. Duesbery, Phys. Rev. Lett. **55**, 1997 (1985).

[30] M.S. Duesbery and B. Joós, Philos. Mag. **54**, 145 (1986).

[31] B. Joós and M.S. Duesbery, Phys. Rev. B **33**, 8632 (1986).

[32] B. Grossmann, B. Joós and M.S. Duesbery, Phys. Rev. B **39**, 7917 (1989).

[33] W.G. Hoover, N.E. Hoover and W.C. Moss, J. Appl. Phys. **50**, 829 (1979).

[34] F.F. Abraham, Adv. Phys. **35**, 1 (1986).

[35] W.G. Hoover, W.T. Ashurst and R.J. Olness, J. Chem. Phys. **60**, 4043 (1974).

[36] W.G. Hoover, A.J.C. Ladd and N.E. Hoover, in: *Interatomic Potentials and Crystalline Defects*, Ed. J.K. Lee (Metallurgical Society, Warrendale, PA, 1981).

[37] A.J.C. Ladd and W.G. Hoover, J. Chem. Phys. **74**, 1337 (1981).

[38] A.J.C. Ladd and W.G. Hoover, Phys. Rev. B **26**, 5469 (1982).

[39] J.A. Combs, Phys. Rev. Lett. **61**, 714 (1988); Phys. Rev. B **38**, 6751 (1988).

[40] B. Joós and M.S. Duesbery, Phys. Rev. Lett. **70**, 2754 (1993).

[41] W.G. Hoover, A.J. de Groot and C.G. Hoover, Comp. Phys. **6**, 155 (1992).

[42] L. Verlet, Phys. Rev. **159**, 98 (1967).

[43] D.S. Fisher, B.I Halperin and R. Morf, Phys. Rev. B **20**, 4692 (1979).

[44] S.T. Chui, Phys. Rev. Lett. **48**, 993 (1982); Phys. Rev. B **28**, 178 (1983).

[45] Y. Saito, Phys. Rev. B **26**, 6239 (1982).

[46] D.C. Houghton, J.P. Noël, N.L. Rowell and D.D. Perovic, in *Muticomponent and Multilayered Thin Films for Advanced Microtechnologies: Techniques, Fundamentals, and Devices*, Vol. **234** of NATO Advanced Study Institute, Series E: Applied Science, edited by O. Auliello and J. Engemann (Kluwer, Dordrecht, 1993), p.401.

[47] H. Alexander, in *Solid State Physics* , edited by F. Seitz, D. Turnbull and H. Ehrenreich (Academic, New York, 1968), Vol. **22**, p.27.

[48] S. Amelinckx, in *Dislocations in Solids* , edited by F.R.N. Nabarro (North-Holland, Amsterdam, 1979), Vol. **2**, p. 294.

[49] H. ALexander, in *Dislocations in Solids* , edited by F.R.N. Nabarro (North-Holland, Amsterdam, 1986), Vol. **7**, p. 114.

[50] A. George and J. Rabier, Rev. Phys. Appl. **22**, 941 (1987).

[51] F. Louchet and J. Thibault-Desseaux, Rev. Phys. Appl. **22**, 207 (1987).

[52] M.S. Duesbery and G.Y. Richardson, CRC Crit. Rev. Solid State Mater. Sci. **17**, 1 (1991).

[53] M.S. Duesbery, D.J. Michel, E. Kaxiras and B. Joós, Mater. Res. Soc. Symp. Proc. **209**, 125 (1991).

[54] E. Kaxiras and M.S. Duesbery, Phys. Rev. Lett. **70**, 3752 (1993).

[55] V. Vitek, L. Lejček and D.K. Bowen, in *Proceedings of the Batelle Colloquium on*

Interatomic Potentials and Simulation of Lattice Defects, Seattle, 1971, edited by P.C. Gehlen, J.R. Beeler Jr. and R.I. Jaffee (Plenum, New York, 1972), p. 493.

[56] V. Vitek and M. Yamaguchi, J. Phys. F **3**, 537 (1973).

[57] M. Yamaguchi and V. Vitek, J. Phys. F **5**, 11 (1975).

[58] F.H. Stillinger and T.A. Weber, Phys. Rev. B **31**, 5262 (1985).

J. Tersoff, Phys. Rev. B **39**, 5566 (1989).

E. Kaxiras and K.C. Pandey, Phys. Rev. B **38**, 12736 (1988).

[59] I.L.F. Ray and D.J.H. Cockayne, Proc. R. Soc. London, Ser. A **325**, 543 (1971).

[60] A.M. Gòmez and P.B. Hirsh, Phil. Mag. **36**, 169 (1977).[63] J. Frenkel and T

[61] K. Wessel and H. Alexander, Philos. Mag. **35**, 1523 (1977).

[62] H. Alexander, H. Gottschalk and C. Kisielowski-Kemmerich, in *Dislocations in Solids*, edited by H. Suzuki, T. Ninomoya, K. Sumino and S. Takeuchi (University of Tokyo Press, Tokyo, 1985), p. 337.

[63] P. Grosbras, J.L. Dement, H. Garem and J.C. Desoyer, Phys. Status solidi A **84**, 481 (1984).

[64] J.L. Demenet, P. Grosbras, H. Garem and J.C. Desoyer, Philos. Mag. A **59**, 501 (1989).

[65] A. Olsen and J.C.H. Spence, Phil. Mag. A **43**, 945 (1981).

[66] P.B. Hirsh, J. Mirco. **118**, 3 (1980).

[67] G.R. Anstis, P.B. Hirsh, P.B. Humphreys, C.J. Hutchison and J.L. Ourmazed, *Microscopy of Semiconductor Materials Conference*, Oxford, 6-10 April 1981, Institute of Physics Conference Series No. 60, P. 1.

[68] A.Bourret, J. Desseaux and A. D'anterroches, *Microscopy of Semiconductor Materials*

Conference, Oxford, 6-10 April 1981, Institute of Physics Conference Series No. 60, P. 15.

[69] J. Castaing, P. Veyessière, L.P. Kubin and J. Rabier, Phil. Mag. A **44**, 1407 (1981).

[70] T. Suzuki and S. Takeuchi, Revue Phys. Appl. **23**, 685 (1988).

[71] T. Suzuki and S. Takeuchi, JJAP Series 2, *Lattice Defects in Ceramics* (1989).

[72] J. Frenkel and T. Kontorowa, Phys. Z. Sowjetunion **13**, 1 (1938).

[73] F.C. Frank and J.H. van der Merwe, Proc. R. Soc. London, Ser. A **198**, 205 (1949).

[74] R. Hobart, J. Appl. Phys. **36**, 1944 (1965); B. Joós, Solid State Commun. **42**, 709 (1982).

[75] A. Foreman, M.A. Jaswon and J.K. Wood, Proc. Phys. Soc. A **64**, 156 (1951).

[76] J.W. Christian and V. Vitek, Rep. Prog. Phys. **33**, 307 (1970).

[77] L. Lejček, Czech, J. Phys. B **22**, 802 (1972).

[78] F. Kroupa and L. Lejček, Czech. J. Phys. B **22**, 813 (1972).

[79] B. Joós, Q. Ren and M. Duesbery, Phys. Rev. B **50**, 5890 (1994).

[80] J.Q. Broughton and X.P. Li, Phys. Rev. B **35**, 9120 (1987).

[81] B.W. Dodson and P.A. Taylor, Appl. Phys. Lett. **49**,642 (1986).

[82] S. Ihara, S.L. Ho, T. Uda and M. Hirao, Phys. Rev. Lett. **65**, 1909 (1990).

[83] J.S. Kallman, W.G. Hoover, A.J. De Groot, S.M. Lee and F. Wooten, Phys. Rev. B **47**, 7705 (1993).

[84] M.S. Duesbery, B. Joós and D.J. Michel, Phys. Rev. B **43**, 5143 (1991).

[85] B. Joós, Q. Ren and M. Duesbery, Surf. Sci. **302**, 385 (1994).

[86] M. Yamaguichi, V. Paidar, D.P. Pope and V. Vitek, Phil. Mag. A **45**, 867 (1982).

[87] V. Paidar, M. Yamaguchi, D.P. Pope and V. Viteck, Phil. Mag. A **45**, 883 (1982).

[88] P.S. Piercy and G.C. Osbourn, J. Metals **39**, 14 (1987); *Strained Layer Superlattices* , ed. T.P. Pearsall, Semiconductor and Semimetals Series Vols. 32 and 33 (Academic Press, Boston, 1990).

[89] F.C. Frank and J.H. van der Merwe, Proc. Roy. Soc. A **198**, 205 (1949); A **198**, 216 (1949); A **200**, 125 (1949).

[90] J.H. van der Merwe and C.A.B. Ball, in *Epitaxial Growth* , Part b, edited by J.W. Matthews (Academic, New York), pp. 493-528.

[91] J.W. Matthews and A.E. Blakeslee, J. Cryst. Growth **27**, 118 (1974); **32**, 265 (1974).

[92] J.W. Matthews, J. Vac. Sci. Technol. **12**, 126 (1975).

[93] B.W. Dodson and J.Y. Tsao, Appl. Phys. Lett. **51**, 1325 (1987).

[94] I.J. Fritz, Appl. Phys. Lett. **51**, 1080 (1987).

[95] J.C. Bean, L.C. Feldman, A.T. Fiory, S. Nakahara and I.K. Robinson, J. Vac. Sci. Technol. A **2**, 436 (1984).

[96] E. Kasper, H.J. Herzog and H. Kibbel, Appl. Phys. **8**, 199 (1975).

[97] I.J. Fritz, S.T. Picreaux, L.R. Dawson, T.J. Drummond, W.D. Laidig and N.G. Anderson, Appl. Phys. Lett. **46**, 967 (1985).

[98] R. Hull, J.C. Bean, J.M. Bonar, G.S. Higashi, K.T. Short, H. Temkin and A.E. White, Appl. Phys. Lett. **56**, 2445 (1990).

[99] P.L. Gourley, I.J. Fritz and L.R. Dawson, Appl. Phys. Lett. **52**, 377 (1988).

[100] R. Hull, J.C. Bean, D.J. Werder and R.E. Leibenguth, Phys. Rev. B **40**, 1681 (1989).

R. Hull, J.C. Bean and C. Buescher, J. Appl. Phys. **66**, 5837 (1989).

R. Hull, J.C. Bean, D. Bahnck, L.J. Peticolas, K.T. Short and F.C. Unterwald, J. Appl.

Phys. **70**, 2052 (1991).

[101] P.M. Mooney, F.K. LeGoues, J. Tersoff and J.O. Chu, J. Appl. Phys. **75**, 8 (1994).

[102] F.K. LeGoues, P.M. Mooney and J. Tersoff, Phys. Rev. Lett. **71**, 396 (1993).

F.K. LeGoues, P.M. Mooney and J.O. Chu, Appl. Phys. Lett. **62**, 140 (1993).

F.K. LeGoues, M.C. Reuter, J. Tersoff, M. Hammer and R.M. Tromp, Phys. Rev. Lett. **73**, 300 (1994).

F.K. LeGoues, Phys. Rev. Lett. **72**, 876 (1994).

[103] D.C. Houghton, J. Appl. Phys. **70**, 2136 (1991).

[104] C.G. Tuppen and C.J. Gibbings, J. Appl. Phys. **68**, 1526 (1990).

[105] J.M. Bonar, R. Hull, R.J. Malik, R.W. Ryan and J.F. Walker, Proc. Mat. Res. Soc. **160**, 117 (1990).

[106] D.C. Paine, D.J. Howard, D. Luo, R.N. Sacks and T.C. Eschrich, Proc. Mat. Res. Soc. **160**, 123 (1990).

[107] R.H. Dixon and P.J. Goodhew, J. Appl. Phys. **68**, 3163 (1990).

[108] F.C. Frank and W.T. Read, in *Symposium on Plastic Deformation of Crystalline Solids*, Carnegie Institute of Technology, Pittsburgh, 1950,44.

[109] W. Hagen and H. Strunk, Appl. Phys. **17**, 85 (1978).

[110] F.K. LeGoues, B.S. Myerson and J.F. Morar, Phys. Rev. Lett. **66**, 2903 (1991);

F.K.LeGoues, B.S. Myerson, J.F. Morar and P.D. Kirchner, J. Appl. Phys. **71**, 4230 (1992).

[111] A. Lefebvre, C. Herbeaux, C. Boillet and J. Di Persio, Phil. Mag. Lett. **63**, 23 (1991).

[112] J. Washburn and E.P. Kvam, Appl. Phys. Lett. **57**, 1637 (1991).

[113] M.A. Capano, Phys. Rev. B 45, 11768 (1992).

[114] V. Higgs, P. Kightley, P.D. Augustus and P.J. Goodhew, Appl. Phys. Lett. **57**, 829 (1991).

[115] D.J. Eaglesham, E.P. Kvam, D.M. Maher, C.J. Humphreys and J.C. Bean, Phil. Mag. A **59**, 1059 (1989).

[116] M.D. DeCotesu, P.R. Wilshaw and R. Falster, Solid State Phen. **19-20**, 27 (1991).

[117] R. Hull and J.C. Bean, J. Vac. Sci. Tech. A **7**, 2580 (1989).

[118] D.D. Perovic and D.C. Houghton, in *Mechanisms of Heteroepitaxial Growth* , edited by M.F. Chisholm, B.J. Garrison, R. Hull and L.J. Schowalter, MRS Symposia Proceedings No. 263 (Materials Research Society, Pittsburgh, 1992).

[119] J.W. Matthews, A.E. Blakeslee and S. Mader, Thin Solid Films **33**, 253 (1976).

[120] E.A. Fitzgerald, G.P. Watson, R.E. Proano, D.G. Ast, P.D. Kirchner, G.D. Pettit and J.M. Woodall, J. Appl. Phys. **65**, 2688 (1989).

[121] S.V. Kamat and J.P. Hirth, J. Appl. Phys. **67**, 6844 (1990).

[122] S.A. Dregia and J.P. Hirth, J. Appl. Phys. **69**, 2169 (1991).

[123] R. Hull and J.C. Bean, Crit. Rev. Solid State Mat. Sci. **17**, 507 (1992).

[124] P.M.J. Maree, J. Appl. Phys. **62**, 4413 (1987).

[125] W.H. Yang and D.J. Srolovitz, Phys. Rev. Lett. **71**, 1593 (1993).

[126] D. Srolovitz, Acta Metall. **37**, 621 (1989); M.A. Grinfeld, Sov. Phys. Dokl. **31**, 831 (1986); R.J. Asaro and W.A. Tiler, Metall. Trans. **3**, 1789 (1972).

[127] B.G. Orr, D. Kessler and C.W. Snyder, Europhy. Lett. **19**, 33 (1992); C.W. Snyder, J.F. Mansfield and B.G. Orr, Phys. Rev. B **46**, 9551 (1992).

[128] B.J. Spencer, P.W. Voorhees and S.H. Davis, Phys. Rev. Lett. 67, 3696 (1991).

[129] A.J. Pidduck, D.J. Robbins, A.G. Cullis, W.Y. Leong and A.M. Pitt, Thin Solid Films **222**, 78 (1992).

[130] D. Vanderbilt and L.K. Wickham, in *Evolution of Thin-Film and Surface Microstructure*, edited by C.V. Thompson, J.Y. Tsao and D.J. Srolovitz, MRS Symposia Proceedings No. 202 (Materials Research Society, Pittsburgh, 1991). P. 555.

[131] D.E. Jesson, S.J. Pennycook, J.M. Baribeau and D.C. Houghton, Phys. Rev. Lett. 71, 1744 (1993); see also, e.g. *Cavities and Cracks in Creep and Fatigue* , edited by J. Gittus (Applied Science, London, 1981).

[132] J. Tersoff and F.K. LeGoues, Phys. Rev. Lett. **72**, 3570 (1994).

[133] J. Grilhé, Europhy. Lett. **23** (2), 141 (1993).

[134] H. Alexander and P. Haasen, in Solid State Physics, vol. **22** (1968).

[135] M. Imai and K. Sumino, Phil. Mag. A **47**, 599 (1983).

[136] J.R. Patel and A.R. Chaudhuri, Phys. Rev. **143**, 601 (1966).

[137] S.J. Cook and P. Clancy, Phys. Rev. B **47**, 7686 (1993).

[138] J.S. Rowlinson, *Liquids and Liquid Mixtures* (Butterworth, London, 1969).